N° d'ordre : 2012-60 ANNÉE 2012

THÈSE

présentée devant
L'ÉCOLE CENTRALE DE LYON

pour obtenir
le grade de DOCTEUR
SPÉCIALITÉ ACOUSTIQUE

par

Cyprien HENRY

Prediction of Broadband Shock-Associated Noise in Static and Flight Conditions

Soutenue le 13 décembre 2012 devant la Commission d'Examen

JURY

Examinateurs :	M.	Christophe BAILLY
	M.	Guillaume BODARD
	M.	Sébastien DECK
	M.	Daniel JUVÉ
	M.	Philippe LAFON (Rapporteur)
	M.	Philip MORRIS (Rapporteur)
	M.	Mauro PORTA

Laboratoire de Mécanique des Fluides et d'Acoustique, UMR CNRS 5509
École Centrale de Lyon

Remerciements

Cette thèse de doctorat a été réalisée en partenariat entre le Centrale Acoustique du LMFA et le département Acoustique de Snecma.

Je remercie tout d'abord Christophe Bailly, Professeur à l'Ecole Centrale de Lyon, pour avoir encadré ce travail. Je lui suis très reconnaissant pour le regard scientifique critique qu'il a porté sur mon travail et pour ses nombreux conseils. Je remercie également Benoît André, dont j'ai pu utiliser les mesures de bruit de choc afin de valider mes travaux. J'adresse également mes remerciements à Daniel Juvé, responsable du Centre Acoustique, pour avoir présidé mon jury de thèse. Je remercie plus largement tout le personnel du Centre Acoustique qui a pu m'aider pendant ces trois ans.

Je remercie Guillaume Bodard, Ingénieur à Snecma, pour avoir suivi avec beaucoup d'intérêt mes travaux. Il a su orienter mon travail et me faire profiter de son expérience d'ancien thésard. Je remercie également Norman Jodet, ancien stagiaire et maintenant Ingénieur à Snecma, que j'ai eu la chance d'encadrer pendant 6 mois. Son stage a permis d'enrichir ces travaux de recherche. Je remercie tout le personnel du département Acoustique dans lequel j'ai effectué cette thèse.

Je remercie Mauro Porta, Ingénieur chez Airbus, pour le regard d'avionneur qu'il a porté sur ces travaux.

Je remercie Philippe Lafon, Ingénieur chercheur à EDF et Philip Morris, Professeur à Penn State, pour avoir relu avec attention ce travail.

Je remercie enfin Sébastien Deck, Ingénieur chercheur à l'ONERA pour l'intérêt qu'il a porté à mon travail.

Contents

Nomenclature

c	Speed of sound
D	Nozzle exit diameter
f_p	Peak frequency of BBSAN
g_0	Green's function of the wave equation in a homogeneous medium at rest
g_L	Green's function of Lilley's equation
I_k	Turbulence intensity
$\mathrm{Im}(z)$	Imaginary part of complex number z
L_c	Potential core length
$\overline{L}_s$	Average shock-cell length
LEE	Linearized Euler Equations
M_d	Nozzle design Mach number
M_{ext}	Freestream Mach number
M_j	Isentropic jet Mach number
M	Local Mach number
NPR	Nozzle pressure ratio p_0/p_∞
p_{stat}	Static pressure
p_s	Shock pressure, $p - p_\infty$
p_∞	Ambient pressure
PSD	Power Spectrum Density
R_{pp}	Cross spectral density
$\mathrm{Re}(z)$	Real part of complex number z
SPL	Sound Pressure Level
St	Strouhal number
S_{pp}	Power spectral density of the acoustic perturbations
u_c	Convection velocity
v_i	Velocity component in the i-th direction
$\boldsymbol{x} = (x_i)_{i=1,2,3}$	Observer location
Greek letters	
$\boldsymbol{\eta} = (\xi, \gamma, \zeta)$	Vector joining two point sources
Φ	Inlet angle
γ	Specific heat ratio of air
ω	Angular frequency
π	Logarithm of the pressure $\frac{1}{\gamma}\ln(p_{\mathrm{stat}}/p_\infty)$
Π_n	n-th component of the vector Green's function
ρ	Air density
τ_s	Turbulence characteristic time scale

Subscripts

0	Stagnation variable
i	Variable number
∞	Undisturbed quantities

Superscripts

$'$	Acoustic perturbations
$*$	Complex conjugate

Introduction

General context

Nowadays, large commercial aircraft are commonly powered with dual-stream turbofans, such as those of the CFM-56 engine family manufactured by SNECMA and General Electric. During the design process of the engine, many requirements have to be met. Objectives are traditionally set on mass, thrust and specific fuel consumption. Though of minor importance in the past, acoustics is now driving the design process, as much as the aforementioned parameters. Indeed, aircraft manufacturers and airliners are now truly concerned about acoustic emissions, and have become more and more demanding on the noise levels for new engines. Stringent environmental norms are the main reason to this. A second reason is that passengers are looking for quieter aircraft cabins.

Noise reduction may be achieved by increasing the transmission loss through the fuselage sidewalls. This approach concerns cabin noise only, and usually leads to an increased aircraft weight. Another approach is to directly study noise sources, bearing in mind that the relative importance of a given source depends on the phase of flight. For instance, the fan source is known to be overwhelming during landing. Predominant sources during the cruise phase are also the subject of much interest. This is easily understood, because cruise is the longest phase of flight. A quieter cruise is beneficial to passengers and crew, and it is a strong asset over competitors.

Two primary sources have been identified in cruise conditions. Boundary layer noise is the first one: it is produced by the unsteady pressure field in the boundary layer developing on the fuselage. The second source is located inside the jet plumes issuing from the engine. It is directly related to the engine operating conditions.

Operating conditions of dual-stream engines

The main modules of a dual-stream engine are shown in Figure 1. Cold air from outside enters the engine through the rotor, and passes through a series of modules. The air flow is split up into two parallel streams: the primary stream flows through the combustion chamber (in red in the figure), while the secondary stream flows along the nacelle walls (in blue in the figure).

At the engine exit, the primary stream is hot and follows the plug slopes. It is surrounded by the cold secondary stream. The operating conditions of each stream may be defined using the Nozzle Pressure Ratio (NPR), that is the ratio between the total and ambient pressure. The typical evolution of the NPRs of the primary and secondary streams during a mission are shown in Figure 2. For both streams, the NPR increases during the climb phase: the atmospheric pressure decreases as the plane climbs, while

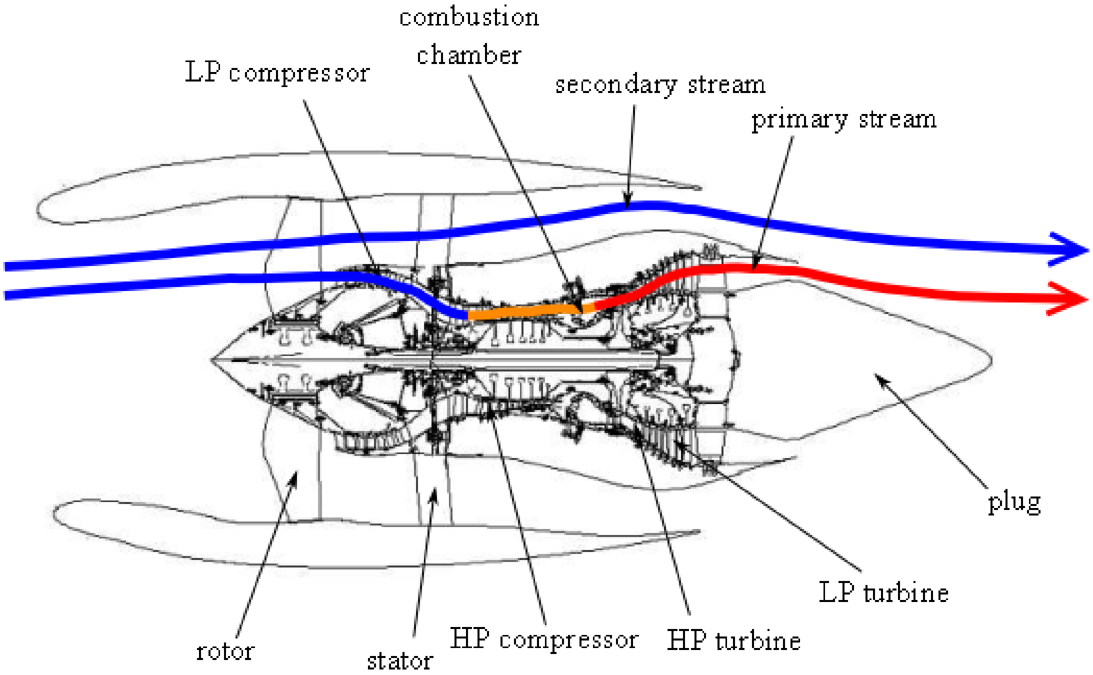

Figure 1: Main modules of a dual-stream civil engine. LP stands for Low Pressure, HP stand for High Pressure. Illustration by SNECMA.

the total pressure remains almost constant. Since the isentropic jet Mach number M_j is proportional to the NPR, the jet Mach numbers increase in the climb phase as well.

Broadband Shock-Associated Noise on civil engines

In cruise conditions, the respective NPRs of each jet are such that the primary stream is subsonic ($M_j < 1$), whereas the secondary stream is supersonic ($M_j > 1$) and imperfectly expanded: in the secondary stream, there is a series of shock-cells. This quasi-periodic structure is surrounded by two shear layers: the inner shear layer between the primary and secondary streams, and the outer shear layer between the secondary stream and the ambient medium. Turbulence is convected in those shear layers and interact with the shock-cells, producing the so-called Broadband Shock-Associated Noise (BBSAN).

BBSAN has been the subject of much interest recently, as shown by the Quiet Technology Demonstrator 2 (QTD2) program: Boeing, General Electric, Goodrich, Spirit and NASA conducted flight tests [16] to characterize BBSAN in flight, as well as to assess new noise reduction technologies such as chevrons.

Needless to say, SNECMA is also concerned by BBSAN and aims at better understanding and reduction of this phenomenon.

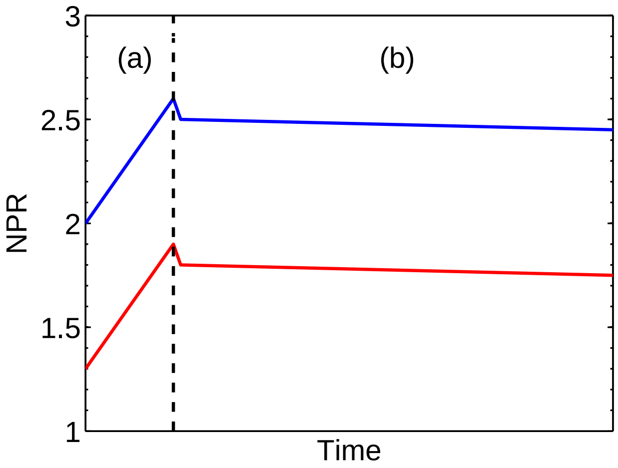

Figure 2: Evolution of the NPRs of the primary and secondary streams during a mission. (a): climb phase, (b): cruise phase. 🟥 primary stream, 🟦 secondary stream

Objectives of the research

This work aims at developing a statistical prediction method for BBSAN, following the work by Morris & Miller [56]. The approach is similar to studies performed for mixing noise models [13, 11, 55]. A methodology has been developed to compute the mean turbulent flow field using the Reynolds Averaged Navier-Stokes (RANS) equations. These equations are solved with elsA, a solver developed by ONERA. Most calculations have been performed on academic configurations. An extensive test campaign has been conducted on these configurations by André [3] at Ecole Centrale de Lyon (ECL), so that calculations have been thoroughly compared to measurements. Mainly, two operating conditions have been tested. The first one is a jet at $M_j = 1.15$, that is NPR=2.27. This condition is typical of a civil engine in cruise. The second operating condition is a jet at $M_j = 1.35$, or NPR $= 2.96$, which rather concerns military engines.

An acoustic model has been developed, starting from the work by Morris & Miller. It uses the RANS calculation as an input to compute Power Spectrum Densities (PSDs). The intermediate version of the model does not account for refraction effects: acoustic sources are propagated to the far-field using a free field Green's function. As will be seen, this gives good results on simple configurations.

The model has been extended to account for refraction effects. This is achieved by computing a Green's function tailored to the problem. A ray tracing method coupled to an adjoint approach has been used to evaluate the Green's function. The computation of the Green's function has been validated for simple cases. The Green's function calculation has been coupled to the acoustic model. PSDs including refraction effects on dual-sream jets are presented.

Organization of the report

In the first chapter, the main characteristics of supersonic shocked jets, from the aerodynamic and acoustic point of view are recalled. The state of the art for BBSAN prediction is presented and the influence of flight on shocked jets is described in the last section. The second chapter introduces the RANS equations along with the $k-\omega-\mathrm{SST}$ model. The finite volume method used to solve the RANS equations is also described. The BBSAN model is developed in the third chapter. The governing equations are derived. They are solved with the Green's functions technique, which is presented. The derivation of the PSD is detailed as well as the numerical implementation. Applications are shown in the fourth chapter. First, the aerodynamic preprocessing is presented, and applied to jets at $M_j = 1.15$ and $M_j = 1.35$. Extensive comparison with measurements are then shown. In the last section of the chapter, acoustic results are presented and compared to experiments.

The inclusion of refraction effects is considered in the fifth chapter. It is shown that the problem consists in the computation of scalar Green's function of Lilley's equation, and relating it to the vector Green's functions of the Linearized Euler Equations (LEE). A ray-tracing algorithm is used to compute the Green's functions: first, the Green's function of Lilley's equation is computed with ray-tracing, then it is used to compute the vector Green's functions of the LEE. These calculations are validated on simple test cases. The final formulation for the acoustic model, including refraction effects is finally derived and the numerical implementation is described.

The last chapter describes the application of the previous developments to jets in flight conditions. First, the aerodynamic results are compared to measurements. Then the full model is applied to these configurations.

Chapter 1

Aero-Acoustics of supersonic shocked jets

Since this work aims at the prediction of BBSAN, it seems natural to recall the physics of the phenomenon under consideration beforehand. The origin of BBSAN is better understood when the aerodynamics of shocked jets is known. This is the subject of the first part. In the second part, the characteristic acoustic spectrum of a supersonic shocked jet is presented, and the three contributing sources are described.

1.1 Aerodynamics of supersonic shocked jets

1.1.1 One-dimensional, isentropic flow of a perfect gas through nozzles

One-dimensional, isentropic flows are considered here. The *isentropic* term means that the flow is inviscid, and more generally that any diffusion effects are neglected.

Flow parameters

Some convenient flow parameters are now presented. Consider an arbitrary flow field, and a given fluid particle traveling at speed v. The static pressure and temperature are respectively given by p and T. The speed of sound c is given by,

$$c = \sqrt{\gamma r T} = \sqrt{\gamma \frac{p}{\rho}} \tag{1.1}$$

where r is the specific gas constant, γ is the heat capacity ratio and ρ is the density of air. For dry air at 20°C, $r = 287.04$ J.kg^{-1}.K^{-1} and $c = 343.21$ m/s. The local Mach number M is given by,

$$M = \frac{v}{c} \tag{1.2}$$

Now imagine that the fluid element is brought adiabatically to $M = 1$. The corresponding variables, obtained from this virtual transformation are written with an asterisk, namely c^*, T^*. Another virtual transformation consists in isentropically slowing the fluid down to zero velocity. The corresponding variables are written with an '0' subscript, namely T_0, p_0 for instance. Those are the stagnation variables, resulting from the stagnation of the fluid. The stagnation variables are conserved by isentropic transformations. Useful relations can be derived from the energy equation. For example, according to Anderson, [2],the speed of sound is a function of the local flow velocity and the total speed of sound,

$$c = \sqrt{c_0^2 - \frac{\gamma - 1}{2} v^2} \tag{1.3}$$

Provided that c_0 remains unchanged (constant stagnation temperature), an increase in the flow speed will reduce the local speed of sound. The stagnation variables are related to the static variables by,

$$\frac{T_0}{T} = 1 + \frac{\gamma - 1}{2} M^2 \quad \frac{p_0}{p} = \left(1 + \frac{\gamma - 1}{2} M^2\right)^{\gamma/(\gamma-1)} \quad \frac{\rho_0}{\rho} = \left(1 + \frac{\gamma - 1}{2} M^2\right)^{1/(\gamma-1)} \tag{1.4}$$

The area-velocity relation

By combining the differential forms of the conservation equations inside a nozzle, a fundamental relation can be established,

$$\frac{dA}{A} = (M^2 - 1)\frac{dv}{v} \tag{1.5}$$

where A is the nozzle cross-section. Equation (1.5) is the *area-velocity* relation. Three cases may then be considered. In subsonic flow, $M < 1$, which means that A and v vary conversely: when the nozzle section decreases, the fluid velocity increases. The opposite holds for a supersonic flow, $M > 1$: A and v vary accordingly, which means that an increase in the nozzle cross-section will speed the flow up. As an example, consider the Vulcain 2 engine of Ariane 5 rocket, shown in Figure 1.1. Before exiting the engine, the supersonic flow is accelerated by the diverging nozzle. The case $M = 1$ corresponds to $dA = 0$. Physically, this means that for isentropic flows the transition from a subsonic to supersonic flow can only take place where the nozzle cross-section is minimum or

Figure 1.1: The Vulcain 2 engine, manufactured by Snecma. The supersonic flow is accelerated in the diverging nozzle

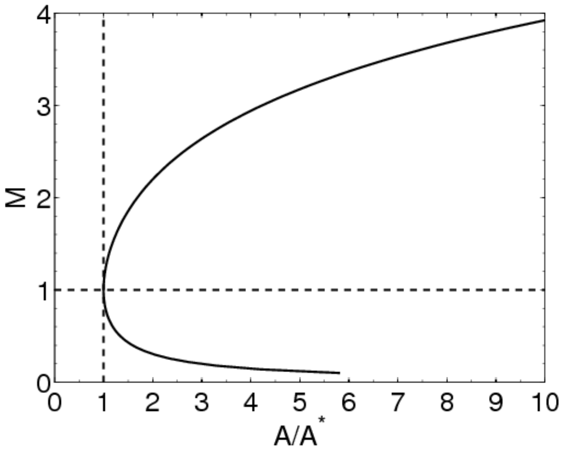

Figure 1.2: Evolution of the local Mach number as a function of the section ratio in a choked nozzle

maximum. The transition may take place at the minimum cross-section only. Nozzles in which the section decreases continuously till the exit are called convergent nozzles. If the section decreases and increases again, the nozzle is said to be converging-diverging. The point where the section is minimum is called the *throat* of the nozzle. This is where the subsonic-supersonic transition occurs.

The area-Mach relation

The conservation of mass provides another insightful result. It is assumed that $M = 1$ at the throat, the nozzle is said to be choked. Further explanation on choked nozzles is provided in 1.1.2 Then, according to Anderson [2],

$$\left(\frac{A}{A^*}\right)^2 = \frac{1}{M^2}\left[\frac{2}{\gamma+1}\left(1+\frac{\gamma-1}{2}M^2\right)\right]^{[(\gamma+1)/(\gamma-1)]} \tag{1.6}$$

Equation (1.6) is called the *area-Mach number* relation. It can be inverted, so that $M = f(A/A^*)$, that is in a choked nozzle, the Mach number depends on the *ratio* of the local cross-section to the throat section. In Figure 1.2, the evolution of M versus A/A^* is shown. For a given section ratio, there are two corresponding Mach numbers, depending on the flow: subsonic (lower part of the curve), or supersonic (higher part of the curve).

1.1.2 Influence of the Nozzle Pressure Ratio

The Nozzle Pressure Ratio (NPR) is a convenient parameter to describe the operating conditions of a nozzle. Assume that air entering the nozzle is coming from a reservoir and exits to the atmosphere. The air in the reservoir is almost at rest, at a stagnation pressure p_0 almost equal to its static pressure. The ambient pressure is p_{atm}. Then the NPR is defined as,

$$\text{NPR} = \frac{p_0}{p_{\text{atm}}} \tag{1.7}$$

It is easily understood that for air to flow through the nozzle requires NPR > 1. The pressure difference between the reservoir and the ambient medium $\Delta p = p_0 - p_{\text{atm}}$, is a function of the NPR:

$$\Delta p = p_{\text{atm}}(\text{NPR} - 1) \tag{1.8}$$

Subsonic flow

Consider the case of a converging-diverging nozzle, where the NPR is slightly above 1. Then the flow velocity will increase in the converging part till the throat, and decrease in the diverging part, according to Equation (1.5). It will stay subsonic throughout the nozzle, and the static pressure at the nozzle exit, p_e will match p_{atm}.

When increasing Δp, the mass flow in the nozzle $\dot{m} = \rho A v$ increases as well. At the throat, the mass flow is $\dot{m}_t = \rho_t A_t v_t$, where the subscript 't' stands for *throat*. Now assume the NPR is further increased. At some point, the flow will be sonic at the throat, that is $\dot{m}_t = \dot{m}^* = \rho^* A^* c^*$, and subsonic everywhere else. What happens if Δp is further increased?

Supersonic flow

Once the flow is sonic at the throat, the mass flow at the throat does not change when increasing Δp. This is the choking phenomenon mentioned above. The flow in the diverging part of the nozzle is now supersonic. For the flow in the nozzle to be isentropic, the pressure at the nozzle exit must satisfy Equation (1.4). If the NPR is not high enough, a normal shock will form inside the nozzle, and the flow will be subsonic behind it. The location of the shock depends on the pressure mismatch. For instance, it will stand exactly at the nozzle exit if the pressure behind the shock equals p_{atm}.

If the NPR is such that $p_e = p_{\mathrm{atm}}$, the flow will follow the isentropic solution given by Equation (1.4) and there will be no shock.

1.1.3 Structure of a subsonic jet

Subsonic jets are extensively covered in the literature. Lilley [46], among others, summarizes the state of the art. Subsonic jets also share many common characteristics with supersonic jets, that is the reason why they are described here first. The evolution of the turbulent kinetic energy and velocity profiles are shown in Figure 1.3. Three distinct regions can be identified in the jet.

Potential core

The potential core lies between $0 \leq x/D \leq 5$ where D is the jet diameter, see (1.9). In this region, the aerodynamic variables are self-similar. Lau *et al.* [41] observed experimentally that the potential core length L_c is a function of the jet Mach number,

$$\frac{L_c}{D} = 4.2 + 1.1 M_j^2 \tag{1.9}$$

According to them, this relation stands for the range of Mach numbers $0.3 - 1.4$, for isothermal jets. A mixing layer originates from the nozzle exit lip, between the jet flow and the ambient medium. It is very thin close to the exit plane and grows axially. Candel [17] gives an estimate of the mixing layer width δ by,

$$\frac{\delta}{D} = 0.153 \left(\frac{x}{D}\right) + 0.002 \tag{1.10}$$

where x is the axial position. Turbulence is created by velocity gradients in the mixing layer. It is shown in Figure 1.3 that the peak of turbulence intensity is initially sharp. When moving downstream, the mixing layer thickens inwards and outwards. Lau [40] showed that the large-scale vortices converge to the jet center-line when travelling downstream, thus destroying the potential core. This leads to a radial spread of the turbulent kinetic energy.

Transition zone

The transition zone connects the potential core to the fully developed region. It is located between $5D$ and $15D$ in Figure 1.3. In the transition region, Lau *et al.* [41] observed that,

$$\frac{v}{v_e} = 1 - \exp\left(\frac{1.35}{1 - \frac{x}{L_c}}\right) \tag{1.11}$$

where v_e is the jet exit velocity and v is the centerline velocity.

Fully developed region

The fully developed region is typically located at $x/D > 15D$ [12]. The turbulence intensity is constant on the jet axis in this region, and velocity on the jet axis decreases like $1/x$.

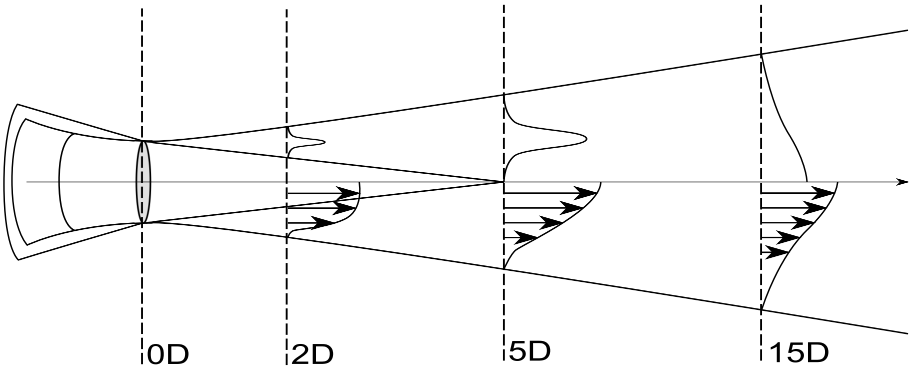

Figure 1.3: Profiles of turbulent kinetic energy (upper half-part) and velocity (lower half-part) in a subsonic jet

Turbulence in subsonic jets

The Reynolds number of the jet, based on its diameter, is defined by $Re = U_j D/\nu$, where U_j is the jet velocity. Re has a strong influence on the turbulent behavior of the jet. For $\mathrm{Re} \leq 10^5$, the jet switches from laminar to turbulent after several diameters, whereas the transition is much faster for $\mathrm{Re} \geq 10^5$.

Crow & Champagne [23] were among the first to observe the coherent structures of subsonic jets. The case of a fog jet at moderate $\mathrm{Re} = 1.95 \times 10^4$ is shown in Figure 1.4. The jet is initially laminar and becomes turbulent after a few diameters. The coherent behavior of large-scale structures is then obvious.

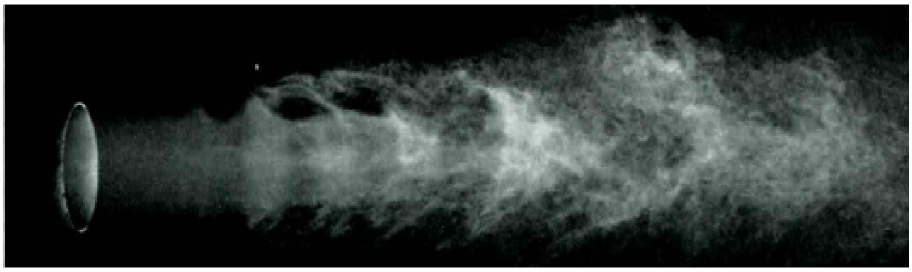

Figure 1.4: Photograph of a for jet at $\mathrm{Re} = 1.95 \times 10^4$, from Crow & Champagne [23]

Brown & Roshko [15] observed the development of large-scale coherent structures in mixing layers, as seen in Figure 1.5. In this Figure, a small perturbation originates at the beginning of the mixing layer and is amplified downstream, until it loses spatial coherence.

The development of large scale instabilities in jets and mixing layers is well predicted by theory. For inviscid flows, Rayleigh [70] showed that a small initial perturbation could be either amplified or damped, depending on the velocity profile of the flow. He derived a necessary condition for amplification: that the velocity profile should have an inflection point. This is the case for both jets and mixing layers. These unstable perturbations are called Kelvin-Helmholtz instabilities.

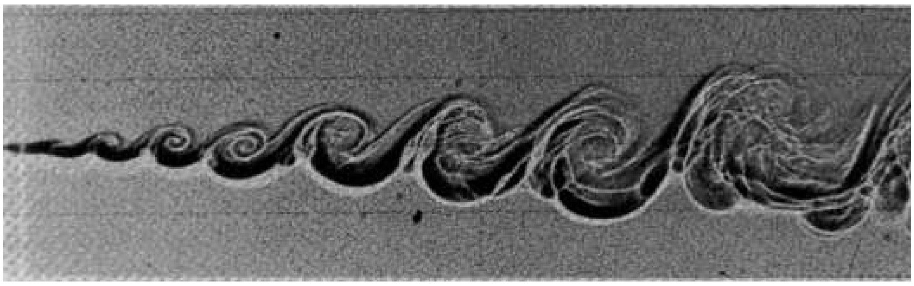

Figure 1.5: Visualization of instabilities in a mixing layer at low Mach number, from Brown & Roshko [15]

1.1.4 Structure of a supersonic shocked jet

As outlined above, subsonic and supersonic shocked jets have common features. The three regions described for subsonic jets (potential core, transition region, fully developed region) also exist in a supersonic jet.

The nature of a supersonic jet depends on the exit conditions. If the static pressure at the nozzle exit p_e is the same as the ambient pressure, then the jet exhausts isentropically into still air. If p_e is greater than the ambient pressure, the jet is said to be *underexpanded*.

Shock-cell structure

Only underexpanded jets are considered in this work. This case is shown in figure 1.6. At the nozzle exit, $p > p_{\mathrm{atm}}$, this creates an expansion fan (in blue), attached to the nozzle lips, that reduces p. When the expansion fan reaches the jet axis, $p = p_{\mathrm{atm}}$. It is nonetheless reflected on the jet axis, into another expansion fan. p decreases again so that $p < p_{\mathrm{atm}}$. When the expansion fan reflects on the jet boundary, it changes to a compression shock (in red), so that p increases again. When the compression shock hits the jet axis, $p = p_{\mathrm{atm}}$. It is reflected into another compression shock, this leads to $p > p_{\mathrm{atm}}$. This pattern forms a shock-cell, it is repeated a number of times, and gradually destroyed by the turbulent mixing layer. In the end, $p = p_{\mathrm{atm}}$.

Figure 1.7 is a schlieren image by André [3]. This is an experimental technique to visualize density gradients. From this image, it is clear that the shock-cell structure is quasi-periodic. Emden extensively observed the quasi-periodic shock-cell structure of shocked jets [29]. Based on these observations, he derived an empirical formula for the average shock-cell length $\overline{L}_s$. Prandtl [66] then accounted for Emden's result from a theoretical point of view. Using an expansion in Bessel's functions to solve the equations governing the flow-field, he found that the wave-length of the leading term was given by,

$$\overline{L}_s = 1.306D\sqrt{M_j^2 - 1} \tag{1.12}$$

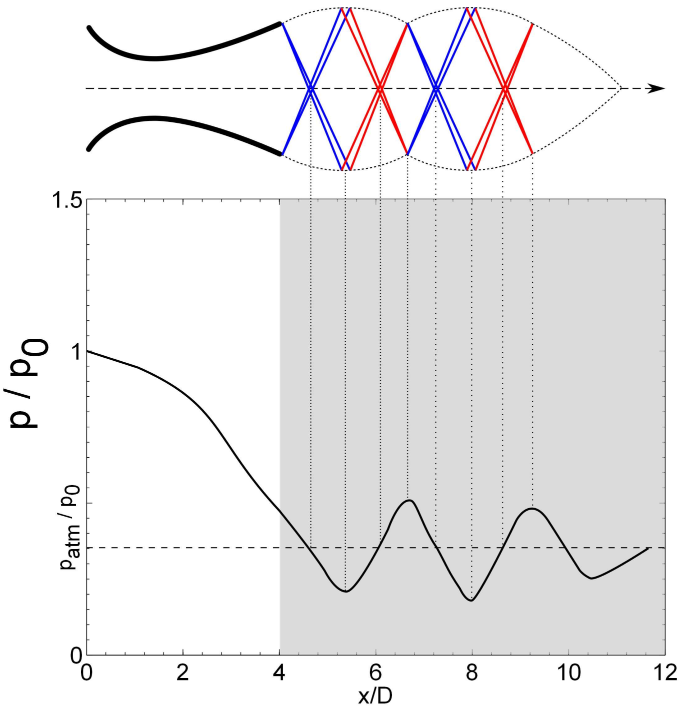

Figure 1.6: Evolution of p/p_0 for an underexpanded jet. —— : expansion fan, —— : compression shock

Pack [62] refined Prandtl's calculation and changed some of Prandtl's hypotheses, and finally obtained a similar formulation,

$$\overline{L}_s = 1.22D\sqrt{M_j^2 - 1} \tag{1.13}$$

A next significant step was to calculate the complete jet structure, that is the evolution of pressure oscillations in the jet. This was carried out by Tam [78] and Tam *et al.* [88]. In his simplest form, Tam's model gives the evolution of the static pressure for an axisymmetric jet,

$$p_{\text{stat}}(x, y) = \sum_{n=1}^{\infty} A_n J_0\left(\frac{2\mu_n y}{D_j}\right)\cos(k_n x) \tag{1.14}$$

The complete expression of A_n and k_n can be found in [78]. D_j is the jet fully expanded diameter, x is the axial position and y the radial position. The periodic structure of the jet is described by a Fourier series. This model does not account for the shortening of the shock-cells downstream and the eventual destruction of the pattern by the merging of the annular mixing layer of the jet. A model accounting for such effects was however developed later by Tam *et al.* [88].

Turbulence in supersonic jets

After the initial observations by Crow & Champagne [23] and Brown & Roshko [15], Tam and his coworkers [87, 92] suggested that turbulent structures could be divided into two categories: fine-scale structures and large-scale structures. Fine-scale structures are inherent to the energy cascade in turbulent flows.

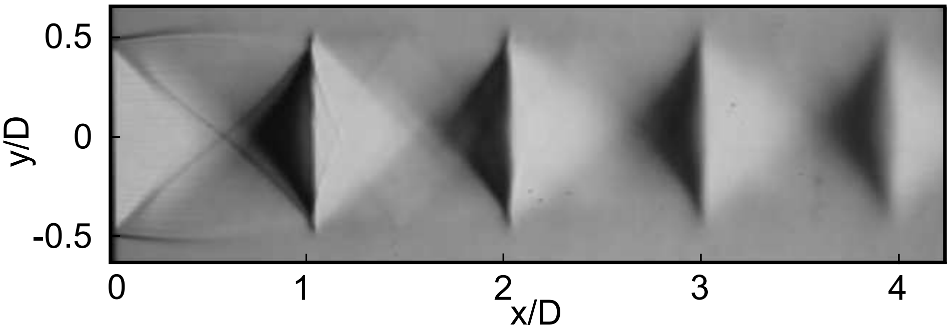

Figure 1.7: Schlieren image of a supersonic shocked jet, issuing from a convergent nozzle. $M_j = 1.15$. Measurements from André [3]

First observed in subsonic jets, large-scale structures also exist in supersonic jets. These jets being fully turbulent, it is more difficult to separate those large-scale structures from fine-scale structures, but they do exist anyway. Tam & Chen [85] used a superposition of normal wave modes of the mean flow, based on Rayleigh's equation and with arbitrary random amplitudes, to represent the coherent structures observed by Brown & Roshko in a mixing-layer, and to derive turbulence statistics. In the same way, Tam & Tanna [91] describe the large-scale structures in a jet by a linear combination of the hydrodynamic instability wave modes of the flow with random amplitude. As an illustration, the transverse velocity perturbation of an instability wave takes the general following form,

$$v' = \mathrm{Re}[a(x)\phi(r)e^{i(kx-\omega t)}] \tag{1.15}$$

where Re denotes the real part, $a(x)$ is the (random) wave amplitude, $\phi(r)$ is the eigenfunction of the mode, k its wave number, and ω its frequency.

1.2 Acoustics of supersonic shocked jets

A typical spectrum produced by a supersonic shocked jet at off-design conditions is shown in Figure 1.8. It is readily observed that there are three components to this spectrum: mixing noise (A), screech (B), BBSAN (C).

1.2.1 Mixing noise

Mixing noise is encountered in both subsonic and supersonic jets, and has been studied widely. It is produced by the self-interaction of turbulence.

Lighthill [44] was the first to address the noise generated by a turbulent jet flow, from the theoretical side. Lighthill considers that noise is produced by turbulence enclosed in a source volume. These sources then radiate into the free-field. By combining the Navier-Stokes equations and the conservation of mass, he derived his well-known acoustic analogy. On the left-hand side of the equation, a propagation operator is applied to an acoustic variable, and on the right-hand side stands a source term (Lighthill's tensor). Lighthill derived an eighth power law for the acoustic power W_{mix} of mixing noise in subsonic jets,

$$W_{\mathrm{mix}} \sim \frac{\rho_j}{\rho_\infty}\frac{U_j^5}{c_\infty^5}A\rho_j U_j^3 \tag{1.16}$$

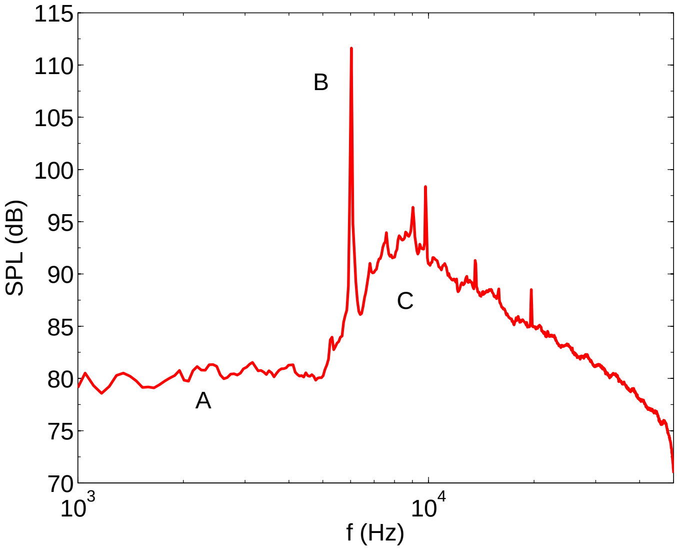

Figure 1.8: Far field sound pressure levels of a supersonic shocked jet. $M_j = 1.15$, $\theta = 130°$ (downstream reference), $R/D = 53.2$. A: mixing noise, B: screech, C: BBSAN. Measurements by André [4]

where A is the jet exit area, and U_j is the jet velocity. When the jet becomes supersonic, W_{mix} scales like U_j^3 [72], rather than U_j^8.

A finer description of mixing noise can be achieved by decomposing turbulence into fine-scale and large-scale structures. This is what Tam and his coworkers [92, 87, 86, 82] suggested. An illustration of this is given in Figure 1.9. The large-scale structures in the mixing layer are shown, as well as two sources of sound: small-scale turbulence, that radiates mainly at 90° from the jet axis, and large-scale turbulence, that emits Mach wave radiation. Tam *et al.* [87] assumed that both sources had different characteristic spectra, and that a mixing noise spectrum was just a combination of those two characteristic spectra.

1.2.2 Screech

The tonal component in Figure 1.8 and the subsequent harmonics are screech. This phenomenon was studied at length by Powell [65] in the fifties, and Raman [67] gives a more recent review of the state of the art. Screech is described as a feedback mechanism along the mixing layer of the jet. Perturbations in the mixing layer start at the nozzle lip and are convected downstream, where they interact with shock-cells. This interaction creates an acoustic wave that propagates upstream to the nozzle lip and triggers subsequent perturbations. This was clearly observed experimentally by Raman [68], see Figure 1.10.

The peak frequency of screech may be simply derived. The time T_{screech} required for a perturbation to be convected from the nozzle exit to the first shock-cell at velocity U_c, and to travel back in the ambient medium at velocity c_0 is,

$$T_{\text{screech}} = \frac{L_s}{U_c} + \frac{L_c}{c_0} \tag{1.17}$$

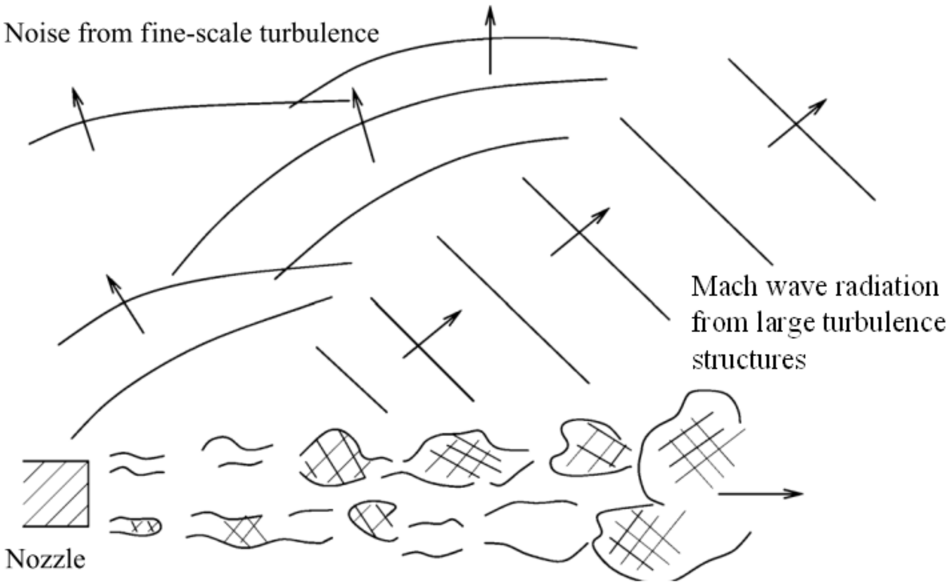

Figure 1.9: Schematic diagram showing the large turbulence structures of a high-speed jet, the sound fields from the fine-scale turbulence and the Mach wave radiation from the large turbulence structures, from Tam [92]

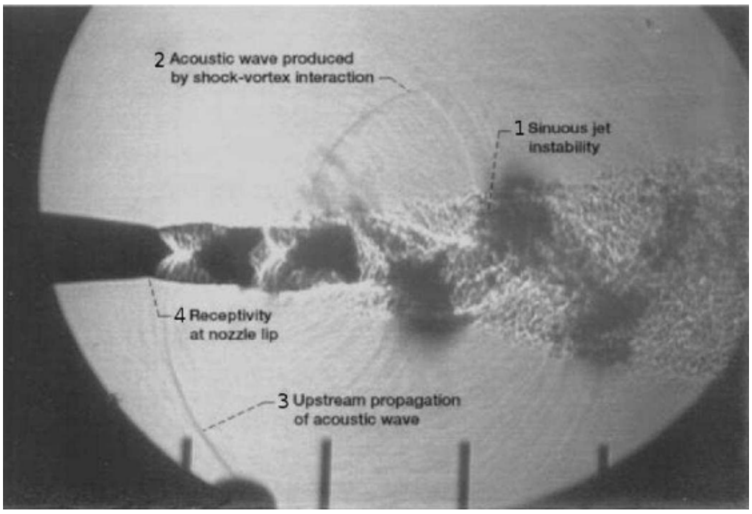

Figure 1.10: The mechanism of screech, as explained by Raman [69]

so that the characteristic frequency $f_{\text{screech}} = 1/T_{\text{screech}}$,

$$f_{\text{screech}} = \frac{1}{L_s}\frac{U_c}{1+M_c} \tag{1.18}$$

where M_c is the convective Mach number. f_{screech} does not vary with position, as opposed to the peak frequency of BBSAN as will be shown below.

The amplitude of screech is an increasing function of M_j, until screech disappears. Indeed, when M_j increases, the interaction between shocks and turbulence creates stronger acoustic waves. Concurrently, the jet swells at the nozzle exit, hence shielding the nozzle lip from the acoustic waves coming from downstream. The lip receptivity is then reduced, interrupting the feedback mechanism.

Directivity depends on the harmonic under consideration: the first peak radiates mainly upstream and downstream, whereas the second peak dominates at 90° from the jet axis.

It should be noted that screech is mostly observed on academic configurations, because they are cleaner. It is not observed on industrial configurations because the geometry is much more complex. For instance, the pylon that connects the engine to the wing breaks the axi-symmetry of the flow, and it is believed that this reduces the lip receptivity to aeroacoustic perturbations.

1.2.3 BBSAN

As opposed to screech, BBSAN is not omni-directional, as clearly seen from Figure 1.11 where spectra of a shocked jet are shown, for various locations. θ is measured from the jet axis. BBSAN is identified by a broadband hump dominating mixing noise at these angles. The characteristics of the hump change with θ: in the upstream direction, the hump compares with a peak, and overwhelms mixing noise by more than 10 dB. As moving to the downstream direction, the peak broadens, and the SPL diminishes.

Harper-Bourne & Fisher's model

Harper-Bourne & Fisher [33] were the first to model BBSAN, on convergent nozzles. They suggested that BBSAN was created by the interaction of turbulence, and shock-cells, like screech tones. Their model consists in a linear array of monopoles, located at the tip of each shock-cell. The monopoles are correlated, and the phasing between each source is set by an eddy convection speed. Then, BBSAN is due to the interference of the sound from those monopoles in the far-field. They were able to derive a complete spectrum with this formulation, as well as a formula for the peak frequency f_p of the hump. It is simply given by,

$$f_p = \frac{U_c}{L_s(1 - M_c\cos\theta)} \tag{1.19}$$

where L_s is the average shock-cell spacing, and θ is the observation angle measured from the jet axis. Equation (1.19) is compatible with previous observations on the evolution of f_p with θ. To assess the evolution of BBSAN intensity I_{BBSAN}, they introduced $\beta = \sqrt{M_j^2 - 1}$. From measurements, they noticed that over a wide range of β,

$$I_{\text{BBSAN}} \propto \beta^4 \tag{1.20}$$

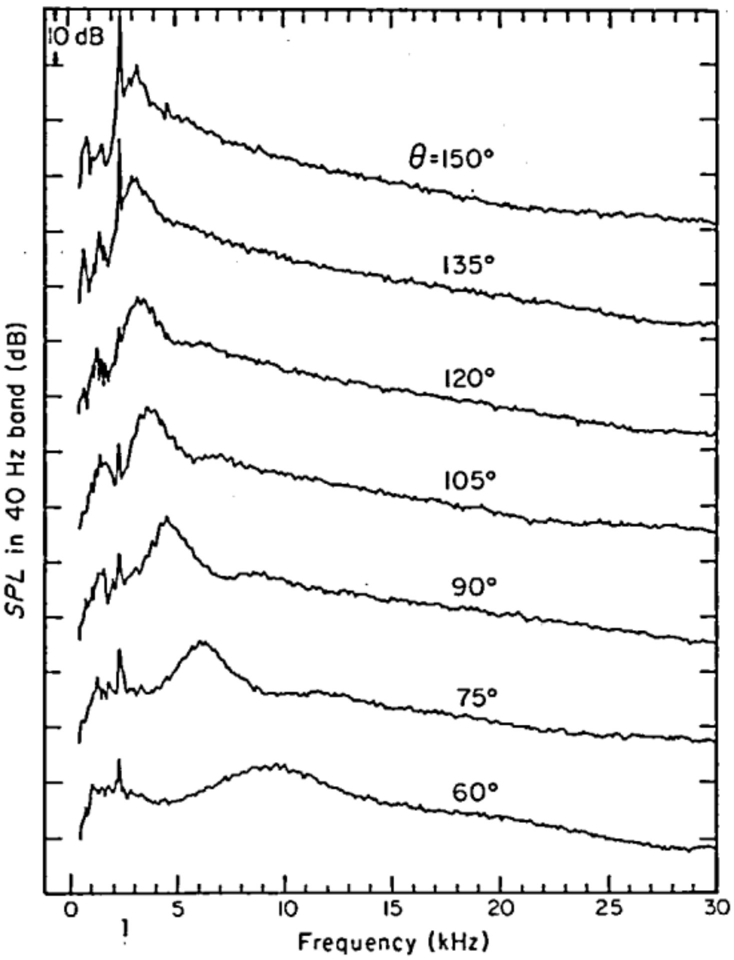

Figure 1.11: Narrow band shock associated noise spectrum from a convergent-divergent nozzle, $M_d = 1.5$, $M_j = 1.8$, from Norum & Seiner [60]. θ is the downstream angle

for convergent nozzles. They inferred that the source strength should scale like β^2, and it turns out that this corresponds to the pressure jump across a normal shock, which seems consistent. This dependence stops for low and large values of β, for distinct reasons. For large β, say $\beta > 1.1$ (or $M_j > 1.48$), the dependence on β is weaker. As noticed by Harper-Bourne & Fisher, a Mach disc is then formed in the first shock-cell, and reduces the source strength. Conversely, for low β, say $\beta < 0.4$ ($M_j < 1.08$), BBSAN becomes contaminated by mixing noise, and it is not possible to isolate it anymore.

Models by Tam *et al.*

Tam & Tanna [91] pointed out some limitations with Harper-Bourne & Fisher's model. Among others, the scaling formula holds only for convergent nozzles, an extension to convergent-divergent nozzles seems necessary. Noise sources are assumed to be very localized, which does not conform with measurements by Seiner & Norum [75]. Consequently, Tam & Tanna proposed another BBSAN generating mechanism. They suggested that BBSAN was created by the weak interaction between large scale turbulent structures in the mixing layer and the nearly periodic shock-cell structure of the jet.

Mathematically, the nearly-periodic shock-cell structure is described using Fourier modes (see Equation (1.14)) by Tam [78], and the large scale turbulent structures by a linear combination of the hydrodynamic instability wave modes of the flow with random amplitude. The weak interaction of shocks and turbulence has a wave nature, and components with supersonic phase velocity may propagate to the far-field. Tam & Tanna found that for any convergent-divergent nozzle,

$$I_{\mathrm{BBSAN}} \propto (M_j^2 - M_d^2)^2 \tag{1.21}$$

which is comparable with Harper-Bourne & Fisher's result for convergent nozzles ($M_d = 1$). They also obtained a similar formula for f_p, but no spectrum could be derived from this work. Tam [79] then pursued this direction, with the same physical explanations, to derive analytical SPLs for the near and far fields of slightly imperfectly expanded jets.

As mentioned before, when M_j increases, a Mach disc forms in the first shock-cell which somewhat changes BBSAN characteristics. Tam [80] showed that the previous model could be extended to such cases, by modifying the original shock cell strengths.

Numerical models

Though analytical models of BBSAN provide valuable results, several authors have developed numerical models to predict BBSAN. This approach is similar to what has been done for mixing noise by Bailly *et al.* [10], Morris & Farassat [55] or Khavaran *et al.* [38] among others.

The objective is to compute the turbulent flow numerically, usually thanks to a turbulence model like $k-\varepsilon$ or $k-\omega$ coupled to a steady simulation of the flow. Miller [50] and Miller & Morris [52, 53, 51] used this technique extensively to predict BBSAN. Their formulation will be used as a starting point for the present work, and is detailed in Chapter 3. Shen *et al.* [76] also proposed an extension of Harper-Bourne & Fisher's model using CFD calculations.

1.3 Shocked jets in flight

So far, only jets in static conditions have been considered. For industrial applications, such as aircraft engines, it is interesting to study the influence of flight on BBSAN. Different ways of simulating jets in flight are presented here. The effects of flight on BBSAN are also presented.

1.3.1 Simulation of flight

In the 1970's, engineers Drevet, Duponchel and Jacques [25] from Snecma used the so-called Aérotrain developed by Jean Bertin to simulate the flight effect. It is shown in Figure 1.12. This vehicle was similar to a hovertrain, so the only resistance would be that of air resistance. It was powered by a civil engine. The nozzle to be tested was located at the outlet of the engine, at the aft of the vehicle. Then, fixed microphones were placed along the track and the Aérotrain would pass by, at high speed. Snecma made measurements up to $M = 0.25$ with this technique.

Figure 1.12: Aérotrain developed by Jean Bertin and used by Snecma engineers for flight effect measurements in the 1970's [25]

A less expensive and more common technique to simulate the effect of flight is to have the main jet surrounded by another jet representing the external flow, as shown in Figure 1.13. The microphones are located outside the external stream. This technique was used at Ecole Centrale de Lyon by André. A simplified experimental setup is shown in Figure 1.14. The BBSAN sources are located at the interface between the main jet and the external stream. A wave emitted by a source at an angle θ_e is convected and bent by the external flow, forming an angle θ_c with the jet axis. When crossing the mixing layer, the propagation path is bent again due to refraction, and makes an angle θ_r with the jet axis. Hence, the wave emitted by the source at angle θ_e is finally received by the observer at angle θ_m.

It is readily seen why some corrections are required. Indeed, the spectrum measured at angle θ_m and distance R_m from the source is different from what would be measured if the microphone were in the same flow as the source (external stream), as in real flight conditions. When measuring at angle θ_m, the corresponding angle for a microphone in external stream jet is θ_c, this suggests that an angular correction is required. An amplitude correction is also required for two reasons: first, the real path followed in the measurements is longer than R_m; second, refraction occurring at the mixing layer changes the wave amplitude.

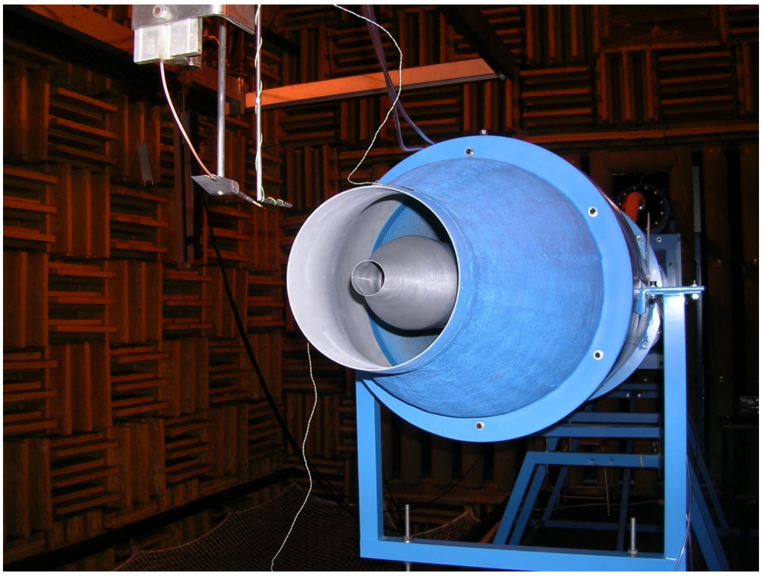

Figure 1.13: Simulation of flight using two coaxial nozzles at Ecole Centrale de Lyon. Photo by André

1.3.2 Amiet's corrections

Ribner [71] was among the first to experiment on this configuration. Later, Amiet [1] used Ribner's conclusions to derive his famous formula for measurements in a wind tunnel. The main results are recalled here. Amiet's corrections relate the different angles together, namely,

$$\tan\theta_c = \frac{\sqrt{(1-M_f\cos\theta_r)^2-\cos^2\theta_r}}{(1-M_f^2)\cos\theta_r+M_f} \tag{1.22}$$

$$R_m\cos\theta_m = \frac{h}{\tan\theta_c}+\frac{R_m\sin\theta_m-h}{\tan\theta_r} \tag{1.23}$$

$$\tan\theta_c = \frac{\sin\theta_e}{M_f+\cos\theta_e} \tag{1.24}$$

Assume θ_m and M_f are fixed. θ_r is found from Equations 1.22 and 1.23. Then θ_c is found using Equation (1.22). Finally, θ_e is determined with Equation (1.24).

The amplitude corrections for a cylindrical vortex sheet are given in [1] and are those used by André for his measurements [3].

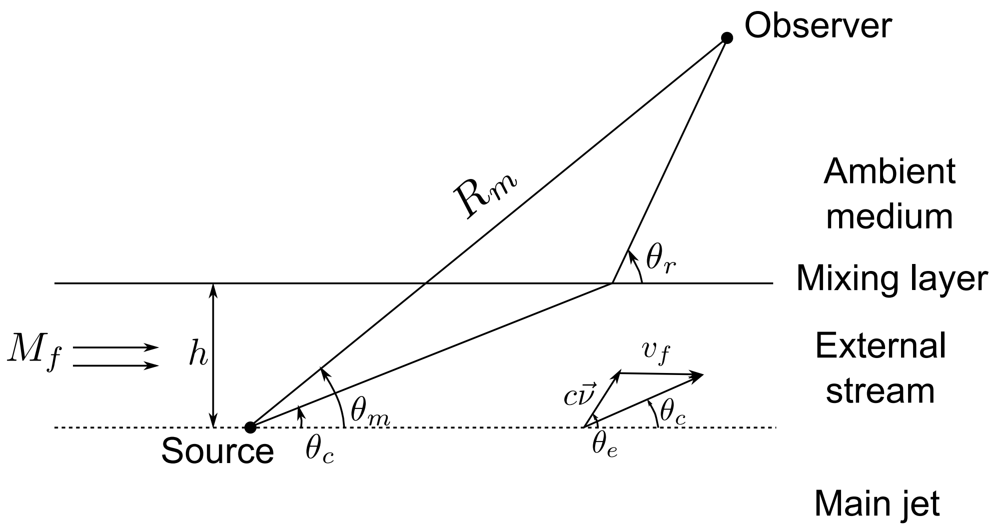

Figure 1.14: Refraction of a ray of sound emitted by a localized source in a jet, from Tam and Auriault [83]

Since for a single measurement there are different angles involved, the question is which angle to choose when comparing several measurements. Norum & Shearing [61] explain that it depends on what is to be investigated. The effect of the wind tunnel condition with the source and observer stationary with respect to each other, but moving with respect to the ground, is investigated at fixed convection angle θ_c. This is what happens if the observer is moving with the airplane for example.

The effect of motion on the intrinsic characteristics of the source (that is motion effect minus convection) are to be studied at constant emission angle θ_e.

1.3.3 Shock structure in flight

As indicated by Morris [54], the main effect of the freestream is to slow the development of the main jet. This is because shear in the mixing layer is reduced, due to lower velocity gradients. This directly increases the potential core length, as well as the number of observed shock cells. Tam [81] mentions that the reduced shear and the increased core length have opposite effects on the instability waves in the mixing layer. The spatial growth of the instability waves is reduced because of reduced shear. Conversely, the longer potential core provides a longer distance for the instabilities to grow. That is why in his model for the prediction of BBSAN in flight, Tam assumes that those two effects cancel out.

The rate of decrease of shock spacing with distance downstream is reduced. Morris also underlines that the flow at the nozzle exit is mostly unaffected by the freestream, because the velocity in the boundary layer that develops on the nozzle exterior is small.

Experimentally, Norum and Shearin [61] carried out extensive measurements on supersonic jets in simulated flight, up to Mach 0.4. They observed a gradual stretching of shock-cells downstream with increasing Mach number. There was no noticeable change in shock strength though.

In their measurements up to $M_f = 0.9$, Norum & Brown [59] noticed that the jet structure is affected significantly by flight from $M_f = 0.6$, though only minor changes occurred before.

1.3.4 Influence of flight on acoustics

Since flight influences the aerodynamics of shocked jets, it is also expected to influence BBSAN. Typical SPLs at increasing M_f are shown in Figure 1.15. $M_f = 0.0$ for the top spectrum, $M_f = 0.2$ for the middle spectrum and $M_f = 0.4$ for the bottom one. The main changes concern the peak frequency f_p of BBSAN and the width of the hump, those changes hold whether θ_e or θ_c is used. As M_f increases, f_p decreases, because the shock-cells lengthen. Flight also reduces the width of the BBSAN hump, as seen on SPLs (c) in Figure 1.15. High order BBSAN peaks may also be identified as M_f is increased. Tam [81] accounted for these modifications and derived a new formula for f_p, including flight effects. The omnidirectionality of BBSAN observed in static conditions is not modified by flight up to $M_f = 0.4$, as noticed by Norum & Shearin.

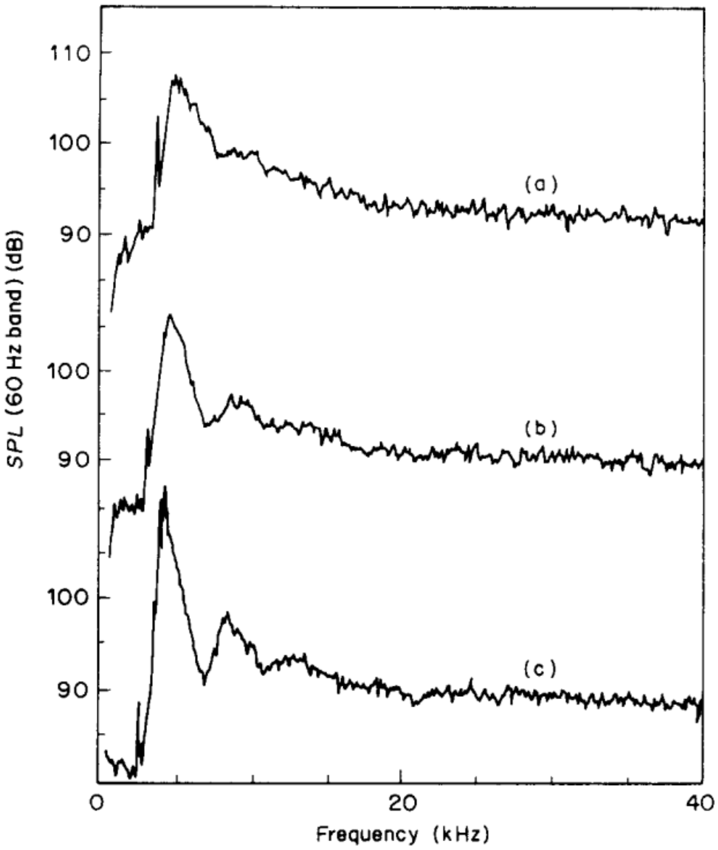

Figure 1.15: Spectra of BBSAN measured in open wind tunnel simulation experiment by Norum & Shearin [61]. $M_j = 1.80$, $M_d = 1.0$, $\theta = 130°$. (a) $M_f = 0.0$, (b) $M_f = 0.2$, (c) $M_f = 0.4$

Norum & Brown [59] noticed that the spectra at different M_f bear some similarity. They inferred that the intrinsic characteristics of the BBSAN sources were not modified, but that the observed differences in the measured noise were mainly due to convection effects. Using in-flow microphones, they clearly observed a convective amplification of

BBSAN in the forward arc with M_f. Brown *et al.* made the same observations. They found a 8 dB difference between the SPLs at $M_f = 0.8$ and $M_f = 0.0$.

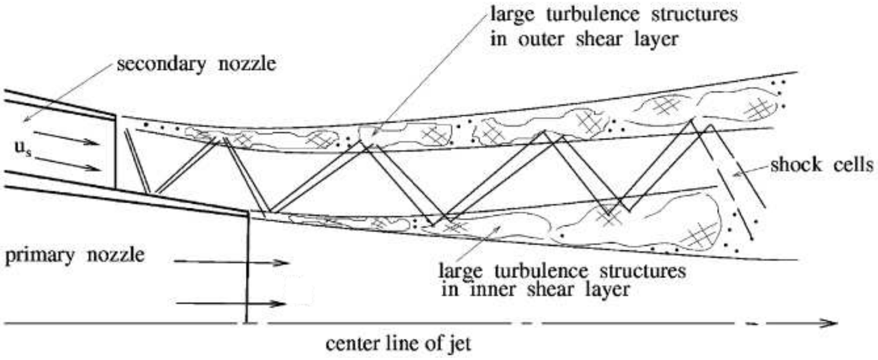

Figure 1.16: Illustration of shock-turbulence interaction, in the inner and outer shear layers, from Tam *et al* [90]

The case of dual-stream jets is more complex. Tam *et al.* [90] underline that in dual-stream jets, BBSAN sources are located in two shear layers, as shown in Figure 1.16: in the inner shear layer between the primary and secondary stream, and in the outer shear layer between the secondary stream and the external stream. Those sources contribute differently to the acoustic field, and their relative contribution has been examined and modeled by Tam *et al.*. The complex radiation of dual-stream jets in flight has been studied by Huber *et al.* [36]. They identified two types of BBSAN sources as well: a low-frequency source located in the outer shear layer, between 6D to 9D after the secondary stream exit, in green in Figure 1.17. The low-frequency source preferentially radiates at 90°. Huber *et al.* used ray tracing to show that this was due to strong convection imposed by the freestream, and found that without the freestream, the source would radiate preferentially in the upstream direction. This is similar to BBSAN sources for static single-stream jets. The high-frequency source is created by the interaction of shocks and turbulence in the inner shear layer and its contribution is measured further downstream on the fuselage. The result is that BBSAN in cruise is mostly perceived by

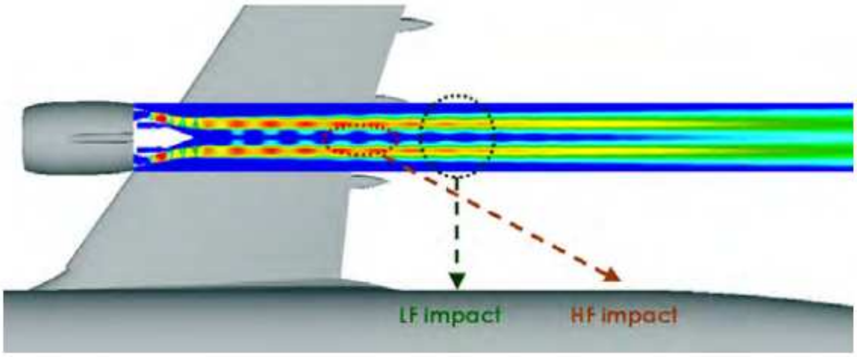

Figure 1.17: Illustration of the two sources contributing to BBSAN in flight. LF: low-frequency, HF: high-frequency, from Huber *et al.* [36]

passengers in the aft of the cabin. This is a major change compared to the static case. The next chapter describes methods for the prediction of the aerodynamic characteristics of shock-containing jets.

Chapter 2

Aerodynamic calculation of supersonic shocked jets

In this chapter, the Reynolds-Averaged Navier-Stokes equations (RANS) are derived. They will be used to compute the mean turbulent flow in the present work. The derivation starts with the Navier-Stokes equations, then the scales relevant to turbulence modeling are recalled. The RANS formulation is described next, followed by the chosen turbulence model. The effects of compressibility on the RANS formulation are presented. Finally, the finite volume method, used to solve the RANS equations, is described.

2.1 Governing equations

The Navier-Stokes equations, named after Claude-Louis Navier and George Gabriel Stokes, provide a general description of fluid motion. They rely on the application of Newton's second law to fluid motion, the stress on the fluid being the sum of a pressure term and a viscous term. The equations are presented in their conservative form. The conservation of mass is written as,

$$\frac{\partial \rho}{\partial t} + \frac{\partial}{\partial x_i}(\rho v_i) = 0 \tag{2.1}$$

where ρ is the density and $\boldsymbol{v}$ is the velocity vector. Einstein convention is used. The conservation of momentum takes the form,

$$\frac{\partial}{\partial t}(\rho v_i) + \frac{\partial}{\partial x_j}(\rho v_i v_j) = -\frac{\partial p}{\partial x_i} + \frac{\partial \tau_{ij}}{\partial x_j} \tag{2.2}$$

where p is the static pressure and $\boldsymbol{\tau}$ is the stress tensor. The convective term $\partial(\rho v_i v_j)/\partial x_j$ is mainly responsible for the strong non-linear behavior of the Navier-Stokes equations. Finally, the conservation of energy is given by,

$$\frac{\partial}{\partial t}\left[\rho\left(e + \frac{1}{2}v_i v_i\right)\right] + \frac{\partial}{\partial x_j}\left[\rho v_j\left(h + \frac{1}{2}v_i v_i\right)\right] = \frac{\partial}{\partial x_j}(v_i \tau_{ij}) - \frac{\partial q_j}{\partial x_j} \tag{2.3}$$

where e is the specific internal energy, $h = e + p/\rho$ is the specific enthalpy, and q_j is the heat flux vector.

Additional relations are required to close the system. It is assumed that the perfect gas law is applicable here, so that pressure, density and temperature satisfy,

$$p = \rho r T \tag{2.4}$$

where T is the absolute temperature and r is the ratio between the perfect gas constant and the molar mass of air, $r \backsimeq 287 J \cdot K^{-1} \cdot kg^{-1}$. Air is treated as a Newtonian fluid, so that the relation between the stress-rate tensor $\boldsymbol{\tau}$ and the strain-rate tensor $\boldsymbol{D}$ is

$$\boldsymbol{\tau} = 2\mu(\boldsymbol{D} - \frac{1}{3}\nabla \cdot \boldsymbol{v}\bar{\bar{I}}) \quad \text{and} \quad D_{ij} = \frac{1}{2}\left(\frac{\partial v_i}{\partial x_j} + \frac{\partial v_j}{\partial x_i}\right) \quad \text{where} \quad \left(\bar{\bar{I}}\right)_{ij} = \delta_{ij} \tag{2.5}$$

where μ is the fluid viscosity. The heat flux vector $\boldsymbol{q}$ is determined with Fourier's law. The fluid is assumed to be calorically perfect, so that

$$e = c_v T \quad \text{and} \quad h = c_p T \tag{2.6}$$

where c_v and c_p are the specific heat coefficients for constant volume and pressure respectively.

2.2 Scales of turbulence

Since the Navier-Stokes equations fully describe fluid motion, it may seem attractive to solve them directly, without any approximation. Depending on the application under consideration, this is not always possible, and different strategies may be considered as shown by Spalart [77]. The direct resolution of the Navier-Stokes equation is called Direct Numerical Simulation (DNS). An approximation of the number of points required to solve the equations is obtained as follows. The smallest length scale of turbulence is the Kolmogorovscale [12, 39], denoted l_η. The largest scales are close to the integral scale, denoted L. Then,

$$\frac{L}{l_\eta} \backsim Re_L^{3/4} \tag{2.7}$$

where $Re_L = \frac{u'L}{\nu}$ is a Reynolds number, u' is a characteristic velocity scale, and ν is the kinematic viscosity. Then, for a 3-D mesh, the total number of points required to resolve all the turbulence scales is

$$N \backsim Re_L^{9/4} \tag{2.8}$$

u' can be approximated by the square root of the turbulent kinetic energy, that is $u' \backsim \sqrt{2/3k}$. A simple application relevant to jet flows is now considered: $u' \backsim 0.2u_j$ and $u_j = 340m/s$. The integral scale is given by the jet diameter $L = D = 0.038m$. Then, $Re_L = 2.10^5$ and the number of points is $N \backsim 10^{12}$. This clearly overwhelms the current computational capabilities.

A coarser approach consists in resolving only the largest scales of turbulence, down to the Taylor length scale λ_g. The Taylor microscale is defined as the largest length scale at which viscous effects significantly alter the dynamics of turbulent eddies [12]. Smaller scales are modeled using a subgrid-scale model. This approach is called Large Eddy Simulation (LES). The following relation holds,

$$\frac{L}{\lambda_g} \backsim Re_L^{1/2} \tag{2.9}$$

The number of points required for the given example is $N \backsim 80 \times 10^6$. Such large meshes are realistic for research purposes but a less demanding approach is required for design work in an industrial context.

The Reynolds-Averaged Navier-Stokes (RANS) equations addresses this issue. The mean flow is computed explicitly, whereas all the scales of turbulence are modeled. As a result, this method is much less time consuming than DNS and LES.

2.3 The Reynolds-Averaged Navier-Stokes equations

The underlying idea in RANS modeling is to split up the true flow field into a mean field and a turbulent field. The mean field is computed explicitly while the turbulent field is modeled.

Let $q(\boldsymbol{x},t)$ be any aerodynamic quantity. It is split up between a mean quantity $< q(\boldsymbol{x},t) >$ and a fluctuating part $q'(\boldsymbol{x},t)$. $< q(\boldsymbol{x},t) >$ is the ensemble average, computed by averaging N independent realizations of $q(\boldsymbol{x},t)$,

$$< q(\boldsymbol{x},t) > \triangleq \lim_{N\to\infty} \frac{1}{N} \sum_{k=1}^{N} q^{(k)}(\boldsymbol{x},t) \tag{2.10}$$

where $q^{(k)}$ is the k-th realization of $q(\boldsymbol{x},t)$. For turbulent jets, turbulence is commonly assumed to be stationary. Then the ensemble average is conveniently replaced by a time average using the ergodicity property

$$< q(\boldsymbol{x},t) > = \overline{q}(\boldsymbol{x},t) \triangleq \lim_{T\to\infty} \frac{1}{2T} \int_{t-T}^{t+T} q(\boldsymbol{x},t')dt' \tag{2.11}$$

The new decomposition for $q(\boldsymbol{x},t)$ is then,

$$q(\boldsymbol{x},t) = \overline{q}(\boldsymbol{x},t) + q'(\boldsymbol{x},t) \qquad \overline{q'} = 0 \tag{2.12}$$

For the sake of simplicity, the consequences of this decomposition are first illustrated for the incompressible Navier-Stokes equations. Substitution (2.12) into the incompressible equations of fluid motion leads to,

$$\frac{\partial \overline{v}_i}{\partial x_i} = 0 \tag{2.13}$$

$$\rho\frac{\partial \overline{v}_i}{\partial t} + \rho\overline{v}_j\frac{\partial \overline{v}_i}{\partial x_j} = -\frac{\partial \overline{p}}{\partial x_i} + \frac{\partial}{\partial x_j}(2\mu\overline{D}_{ij} - \rho\overline{v_i'v_j'}) \tag{2.14}$$

Equation (2.14) is the classical RANS equation for incompressible flow. The quantity $-\rho\overline{v_i'v_j'}$ is the Reynolds stress tensor. Hence, 6 new unknown variables were produced by the averaging process, $-\rho\overline{v_i'v_j'}$ being symmetrical, and the system (2.13)-(2.14) is not closed.

The most common closure for the RANS equations relies on an analogy between the Reynolds stress tensor and the stress tensor. For a Newtonian fluid, the stress and deformation tensors satisfy equation (2.5). Boussinesq [14] assumed that a similar relation linked the Reynolds stress tensor to the rate-of-strain rate tensor:

$$-\rho\overline{v_i'v_j'} = 2\mu_t\overline{D}_{ij} - \frac{2}{3}\rho k\delta_{ij} \quad \text{and} \quad k = \frac{1}{2}\overline{v_i'v_j'} \tag{2.15}$$

where k is the mean turbulent kinetic energy and μ_t is the turbulent viscosity. The determination of the Reynolds stress tensor is then reduced to the computation of the turbulent viscosity. Unlike the fluid viscosity, the eddy viscosity is not an intrinsic property of the fluid. Dimensional analysis shows that μ_t has dimensions of (density × speed × length). It thus depends on the characteristic turbulence scales of the flow under consideration. μ_t will be computed thanks to appropriate turbulence models.

2.4 The $k - \omega -$ SST turbulence model

Various models exist to determine μ_t and the turbulence scales. Georgiadis *et al.* [32] conducted a comparative study of turbulence models for jet flow predictions: they compared classical turbulence models such as $k - \varepsilon$ [37], and $k - \omega -$ SST [94] to turbulence models tuned for jet flows. They concluded that those specific models improved predictions of mean axial velocities for a heated jet, but do not improve the prediction of k upon standard models.

In this work, use is made of the mean turbulent kinetic energy k and the specific dissipation rate ω, whose dimensions are $(\text{time})^{-1}$. $k^{1/2}$ has dimensions of (speed), $k^{1/2}\omega$ has dimensions of (length). On dimensional grounds,

$$\mu_t = \rho \times \underbrace{k^{1/2}}_{\text{speed}} \times \underbrace{k^{1/2}/\omega}_{\text{length}} = \rho \frac{k}{\omega} \tag{2.16}$$

The knowledge of k and ω thus makes it possible to compute μ_t. Two transport equations are used to account for the evolution of k and ω in the turbulent flow. Wilcox [94] suggested that

$$\underbrace{\frac{\partial k}{\partial t} + \overline{v}_j \frac{\partial k}{\partial x_j}}_{(a)} = \underbrace{-\rho \overline{v'_i v'_j} \frac{\partial \overline{v}_i}{\partial x_j}}_{b} - \underbrace{\beta^* k \omega}_{(c)} + \underbrace{\nabla.[(\nu + \sigma^* \nu_t)\, \nabla k]}_{(d)} \tag{2.17}$$

$$\underbrace{\frac{\partial \omega}{\partial t} + \boldsymbol{v}.\nabla\omega}_{(e)} = \underbrace{\frac{\gamma}{\mu_t}}_{(f)} P_k - \underbrace{\beta\omega^2}_{(g)} + \underbrace{\nabla.[(\nu + \sigma\nu_t)\nabla\omega]}_{(h)} \tag{2.18}$$

where β^*, σ^*, γ and σ are constants of the model. In (2.17), (a) is the **material derivative** of the turbulent kinetic energy. (b) is the **production term**, accounting for the transfer of turbulent kinetic energy from the mean flow to turbulence. (c) is the **dissipation term**, it represents the conversion of k into internal energy (heat). (d) is a complex term. $\nu\nabla k$ describes the diffusion of k by molecular motion in the fluid. $(\sigma^*\nu_t)\nabla k$ results from the sum of triple velocity fluctuations (regarded as the transport of k by turbulent fluctuations), and a correlation term between velocity fluctuations and pressure.

(2.18) bears a similarity with (2.17): the specific dissipation is convected through the flow by the **material derivative** (e), (f) is the **production** term, (g) models **dissipation** and (h) accounts for **diffusion**.

This model is robust, properly handles adverse pressure gradients and does not use a damping function in the viscous sub-layer [95]. The main flaw is that it is very sensitive to the freestream value ω_∞ of the dissipation rate. In [49], Menter reports that similar values of ω_∞ may change ν_t by 100%. This is the reason why Menter developed a so-called "BaSeLine" model or BSL formulation.

2.4.1 The $k-\omega-$BSL model

This model combines the qualities of Wilcox's model close to the wall, with the weak dependence of the $k-\varepsilon$ model on the freestream conditions. In the $k-\varepsilon$ formulation [37], ε is the dissipation rate of the turbulent kinetic energy. This is achieved by re-writing the $k-\varepsilon$ model in terms of $k-\omega$ variables, and a blending function joins the two formulations. The governing equations are,

$$\frac{\partial k}{\partial t} + \boldsymbol{v}.\nabla k = P_k - \beta^* \omega k + \nabla.[(\nu + \sigma_k \nu_t)\nabla k] \tag{2.19}$$

$$\frac{\partial \omega}{\partial t} + \boldsymbol{v}.\nabla \omega = \frac{\gamma}{\rho} P_\omega - \beta \omega^2 + 2(1-F_1)\sigma_{\omega_2}\frac{1}{\omega}\nabla k.\nabla\omega + \nabla.[(\nu + \sigma_\omega \nu_t)\nabla \omega] \tag{2.20}$$

The determination of the model constants is detailed in Annex A.1. In summary, the $k-\omega-$BSL model is identical to Wilcox's model in the viscous sub-layer, it then switches to a high-Reynolds number version of Jones-Launder's $k-\varepsilon$ farther from the wall.

2.4.2 The $k-\omega-SST$ model

The $k-\omega-$SST model was developed by Menter [48]. SST stands for Shear Stress Transport. Indeed, the objective of this model is to correctly transport shear in a boundary layer facing an adverse pressure gradient. Menter noticed that classical formulations of the $k-\omega$ model overestimated the shear stress in boundary layers with adverse pressure gradient. To circumvent this flaw, he modified the expression of ν_t in the case of boundary layers with adverse pressure gradient. This expression was then combined with the expression for standard boundary layers, leading to

$$\nu_t = \frac{a_1 k}{\max(a_1\omega, \Omega F_2)}, \quad F_2 = \tanh(arg^2), \quad arg = \max\left(2\frac{\sqrt{k}}{0.09\omega y}, \frac{400\nu}{y^2\omega}\right) \tag{2.21}$$

where $a_1 = 0.3$ and $\Omega = ||\nabla \boldsymbol{v}||$. For free shear flows, another expression of ν_t is used and the transition is made with a blending function. Details are given in Annex A.1. This is the model used in this work to compute supersonic jet flows.

2.5 Effects of compressibility

The RANS equations derived above assumed the mean flow was incompressible as a first approximation. When dealing with supersonic jets, compressibility effects cannot be neglected. Thus, the previous equations should be modified to account for compressibility. It appears convenient to use a density-weighted average, known as the Favre average. The Favre average $\tilde{q}$ of a flow variable q is defined by

$$\tilde{q} = \frac{\overline{\rho q}}{\overline{\rho}} \tag{2.22}$$

So that the new decomposition is,

$$q = \tilde{q} + q'' \qquad \widetilde{q''} = 0 \tag{2.23}$$

Applying this decomposition to the Navier-Stokes equations leads to the compressible RANS equations,

$$\frac{\partial \overline{\rho}}{\partial t} + \frac{\partial}{\partial x_i}(\overline{\rho}\tilde{v}_i) = 0 \tag{2.24}$$

$$\frac{\partial}{\partial t}(\overline{\rho}\tilde{v}_i) + \frac{\partial}{\partial x_j}(\overline{\rho}\tilde{v}_j\tilde{v}_i) = -\frac{\partial P}{\partial x_i} + \frac{\partial}{\partial x_j}\left[\tau_{ji} - \overline{\rho v_j'' v_i''}\right] \tag{2.25}$$

$$\begin{aligned} &\frac{\partial}{\partial t}\left[\overline{\rho}\left(\tilde{e} + \frac{\tilde{v}_i\tilde{v}_i}{2}\right) + \frac{\overline{\rho v_i'' v_i''}}{2}\right] + \frac{\partial}{\partial x_j}\left[\overline{\rho}\tilde{v}_j\left(\tilde{h} + \frac{\tilde{v}_i\tilde{v}_i}{2}\right) + \tilde{v}_j\frac{\overline{\rho v_i'' v_i''}}{2}\right] \\ &= \frac{\partial}{\partial x_j}\left[-q_{L_j} - \overline{\rho v_j'' h''} + \overline{\tau_{ji} v_i''} - \overline{\rho v_j'' \frac{1}{2} v_i'' v_i''}\right] + \frac{\partial}{\partial x_j}\left[\tilde{v}_i(\overline{\tau_{ij}} - \overline{\rho v_i'' v_j''})\right] \end{aligned} \tag{2.26}$$

This decomposition is applied to the variables of the Navier-Stokes equations and to the transport equations of turbulent quantities such as k and ω. This leads to the compressible RANS equations.

2.6 Finite volume method

The RANS equations described before are solved with the elsA solver by Onera [42]. This solver uses a finite volume method to solve the equations. First, the RANS equations are written in an integral form on the CFD domain, stating the conservation of mass, momentum and energy. The domain is then split up into elementary control volumes (known as cells) and the integral equations are solved for each elementary cell.

The RANS equations may be recast into a conservative form on a volume Ω, stating the balance between the variations of a state vector $\boldsymbol{W}$ and the flux crossing Ω through its border $\partial\Omega$,

$$\frac{\partial}{\partial t}\int_{\Omega} \boldsymbol{W}\, d\Omega + \int_{\partial\Omega} \boldsymbol{F} \cdot d\boldsymbol{S} = 0 \tag{2.27}$$

Let's assume that Ω is now an elementary cell, the coordinates of its center being (i, j, k). Then the balance of any conservative variable becomes,

$$V_{i,j,k}\frac{dW_{i,j,k}}{dt} + R_{i,j,k} = 0 \tag{2.28}$$

where $W_{i,j,k}$ designates any conservative component of the state vector $\boldsymbol{W}$, $V_{i,j,k}$ is the cell volume and $R_{i,j,k}$ is the residual stating the balance between the fluxes entering and leaving the cell. More explicitly,

$$R_{i,j,k} = (F_{i+1/2,j,k} - F_{i-1/2,j,k}) + (F_{i,j+1/2,k} - F_{i,j-1/2,k}) + (F_{i,j,k+1/2} - F_{i,j,k-1/2}) \tag{2.29}$$

The notations are defined in Figure 2.1. For instance, $F_{i+1/2,j,k}$ designates the flux crossing the face BCGF. In order to compute the residual $R_{i,j,k}$, the fluxes need to be evaluated numerically. This is detailed in the next section.

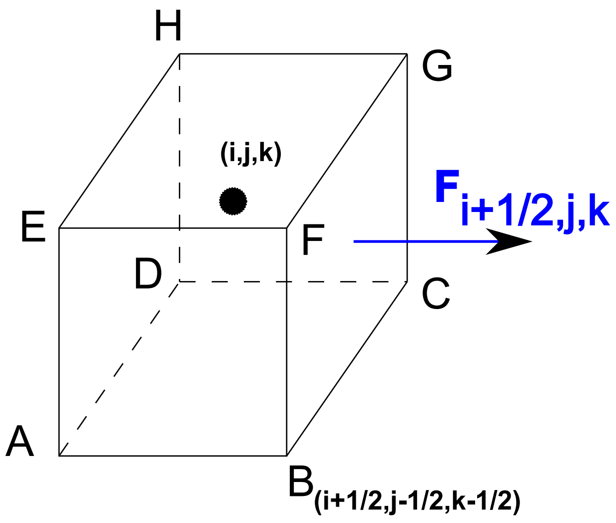

Figure 2.1: Elementary cell used in the finite volume formulation and associated notations

2.6.1 Spatial integration

The first step to evaluate the residual term is to split up the flux tensor into a convective and diffusive part, respectively written $\boldsymbol{F}_c$ and $\boldsymbol{F}_d$. The integral form of the RANS equations is then,

$$\frac{\partial}{\partial t}\int_{\Omega}\boldsymbol{W}d\Omega+\int_{\partial\Omega}\boldsymbol{F}_c\cdot d\boldsymbol{S}+\int_{\partial\Omega}\boldsymbol{F}_d\cdot d\boldsymbol{S}=0 \tag{2.30}$$

The complete expressions of $\boldsymbol{W}$ and the flux vectors are given in Appendix A.2. The convective flux contains first order space derivatives, whereas the diffusive flux contains second order space derivatives. The convective and diffusive fluxes are evaluated separately, starting with the convective fluxes.

2.6.2 Computation of convective fluxes

The convective fluxes are computed with a Roe numerical scheme [73]. This scheme solves the Riemann problem for hyperbolic equations. As a reminder, consider the initial-value problem

$$\frac{\partial\boldsymbol{u}}{\partial t}+\frac{\partial\boldsymbol{F}}{\partial x}=0 \tag{2.31}$$

where $\boldsymbol{u}(x,t)$ is unknown and $\boldsymbol{F}$ is a non-linear function of $\boldsymbol{u}$. It is assumed that the Jacobian matrix $\boldsymbol{A}=\frac{\partial\boldsymbol{F}}{\partial\boldsymbol{u}}$ has only real eigenvalues, which is the case for a hyperbolic system. The general initial condition is

$$\boldsymbol{u}(x,0)=\boldsymbol{u}_0(x) \tag{2.32}$$

The Riemann problem corresponds to restricting the initial condition (2.32) to

$$\boldsymbol{u}(x,0)\triangleq\boldsymbol{u}_L\ (x<0)\quad\text{and}\quad\boldsymbol{u}(x,0)\triangleq\boldsymbol{u}_R\ (x>0) \tag{2.33}$$

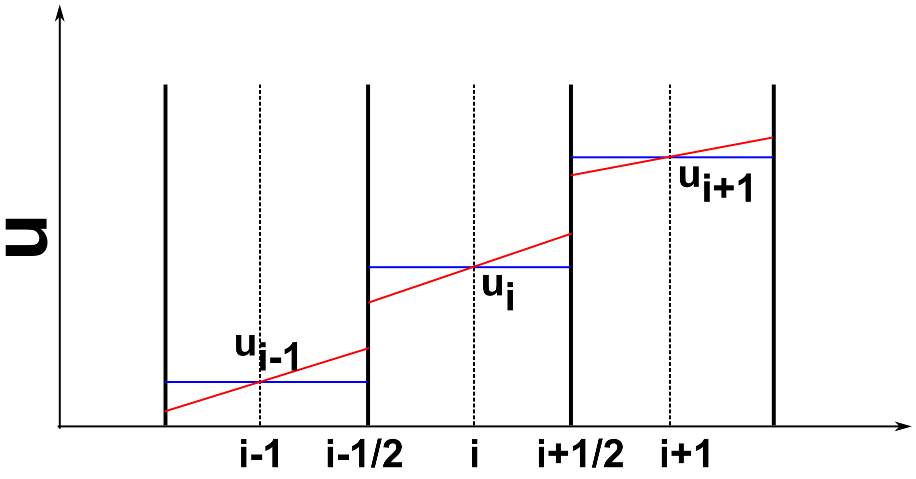

Figure 2.2: First and second order approximation of convective fluxes

where $\boldsymbol{u}_R$ and $\boldsymbol{u}_L$ are constants. Thus, solving the Riemann problem consists in studying the propagation of a discontinuity through the fluid. In the case of the Roe scheme, the convective flux $\boldsymbol{F}_c$ at the interface between two cells is approximated by

$$\boldsymbol{F}_c(\boldsymbol{W}_L, \boldsymbol{W}_R) = \frac{\boldsymbol{F}_c(\boldsymbol{W}_L) + \boldsymbol{F}_c(\boldsymbol{W}_R)}{2} - \frac{1}{2}|\tilde{\boldsymbol{A}}|(\boldsymbol{W}_R - \boldsymbol{W}_L) \tag{2.34}$$

where $\boldsymbol{W}_L$ and $\boldsymbol{W}_R$ are the state vectors in the left and right adjacent cells respectively. $\tilde{\boldsymbol{A}}$ is the Roe matrix that satisfies the following properties

1. As $\boldsymbol{W}_L \to \boldsymbol{W}$ and $\boldsymbol{W}_R \to \boldsymbol{W}$, $\tilde{\boldsymbol{A}} \to \boldsymbol{A}$, where $\boldsymbol{A} = \partial \boldsymbol{F}_c / \partial \boldsymbol{W}$
2. $\forall(\boldsymbol{W}_R, \boldsymbol{W}_L)$, $\tilde{\boldsymbol{A}}(\boldsymbol{W}_L - \boldsymbol{W}_R) = \boldsymbol{F}_L - \boldsymbol{F}_R$
3. The eigenvectors of $\tilde{\boldsymbol{A}}$ are linearly independent

In Figure 2.2, the approximation of the numerical fluxes is detailed, in the case where u is a primitive variable (velocity, mass or pressure). The variables at the interface $i + 1/2$ are approximated by

$$u^L_{i+1/2} = u_i \quad u^R_{i+1/2} = u_{i+1} \tag{2.35}$$

This approximation is illustrated in blue in Figure 2.2. The discontinuities in a supersonic flow are correctly captured with this approximation, without oscillations. Nonetheless, the scheme is first order accurate in space only. Accuracy is extended to second order using a MUSCL (Monotone Upwind Schemes for Conservation Laws) approach. This is shown in red in Figure 2.2: the primitive variables are assumed to vary linearly inside each cell. The drawback of this approach is that it creates wiggles in regions of strong gradients. In these regions, this issue is circumvented with slope limiters. The primitive variables including slope limiters are determined by,

$$u^L_{i+1/2} = u_i + \frac{1}{2}\sigma_i \tag{2.36}$$

$$u^R_{i+1/2} = u_{i+1} - \frac{1}{2}\sigma_{i+1} \tag{2.37}$$

where $\sigma_i = \psi(u_i - u_{i-1}, u_{i+1} - u_i)$ is the slope. There are several formulations for the slope limiter ψ. Van Albada's expression [93] has been used in this work, that is,

$$\psi(u, v) = \frac{(v^2 + \varepsilon)u + (u^2 + \varepsilon)v}{u^2 + v^2 + 2\varepsilon} \qquad \varepsilon << 1 \tag{2.38}$$

This limiter is robust and deals correctly with discontinuities in supersonic flows.

2.6.3 Computation of diffusive fluxes

The diffusive fluxes are computed separately from the convective fluxes. The gradients of velocity, temperature and turbulent quantities are involved in their expression. The gradients are approximated with the average value formula: the gradient of any scalar quantity ϕ in a given cell Ω is estimated by,

$$\nabla\phi = \frac{1}{V(\Omega)} \int_{\Omega} \nabla\phi d\Omega \tag{2.39}$$

where $V(\Omega)$ is the volume of the cell. Further information is given in [42].

2.6.4 Time integration

A classic Euler scheme is used for time integration. The discrete version of (2.28) at two time steps t_n and t_{n+1} is

$$V_{i,j,k} \frac{W^{n+1}_{i,j,k} - W^{n}_{i,j,k}}{\Delta t} + R_{i,j,k} = 0 \tag{2.40}$$

where Δt is the time step. The state variable at t_{n+1}, namely $W^{n+1}_{i,j,k}$ is readily given by,

$$W^{n+1}_{i,j,k} = -\frac{\Delta t}{V_{i,j,k}} W^{n}_{i,j,k} \tag{2.41}$$

This scheme is of first order in time, which is sufficient because only the steady flow is to be computed.

2.7 Conclusion

The equations governing a compressible turbulent flow have been briefly presented. Starting from the Navier-Stokes equations, the steady RANS formulation was derived. Turbulence was accounted for using a $k - \omega -$ SST model. The finite volume method was described. Tt is used to solve the RANS equations. The formulation is implemented in elsA, a CFD solver developed by Onera used to compute the mean turbulent flow. The output of the aerodynamic calculation will serve as input for the acoustic model presented in next chapters.

Chapter 3

Development of a BBSAN model

3.1 Overview

As explained in Section 1.2.3, the objective of the present study is to develop a statistical model of BBSAN, using a mean turbulent flow as input. The model relies on the well-accepted idea that BBSAN is created by the interaction of turbulence and shocks. The initial steps in the derivation of the model are similar to the work by Morris and Miller [52, 57, 56], though significant changes are made in the end.

This chapter is organized as follows: first the equations governing the acoustic pressure are derived. Second, it is shown how to compute the Green's functions associated with these equations. The cross-correlation and the PSD of the acoustic pressure are computed in next two sections respectively. The correlation function of the source term is examined in a fifth part. Finally, the technical implementation of the model is described.

Refraction effects are neglected in this chapter as a first approximation. They will be modeled using geometrical acoustics in Chapter 5.

3.2 Governing equations

The model relies on the LEE (Linearized Euler Equations). A dimensionless pressure variable π is introduced, according to Phillips [63],

$$\pi = \frac{1}{\gamma} \ln \left(\frac{p}{p_\infty} \right) \tag{3.1}$$

where p is the static pressure and γ is the specific heat ratio of air. For air considered as a perfect gas, the relation $p = p(\rho, s)$ defines an equation of state, where s is the entropy and ρ the density. The total derivative of p is,

$$dp = \left.\frac{\partial p}{\partial \rho}\right|_s d\rho + \left.\frac{\partial p}{\partial s}\right|_\rho ds \quad \text{that is} \quad dp = c^2 d\rho + \frac{p}{c_v} ds \tag{3.2}$$

where c denotes the speed of sound and c_v the specific heat capacity at constant volume. The sound velocity is given by $c^2 = \gamma p/\rho$ so that,

$$\frac{dp}{p} - \gamma \frac{d\rho}{\rho} = \frac{1}{c_v} ds \tag{3.3}$$

The conservation of mass can thus be rearranged as,

$$\frac{\partial v_i}{\partial x_i} = -\frac{1}{\rho}\frac{D\rho}{Dt} = \frac{1}{\gamma}\left(\frac{1}{c_v}\frac{Ds}{Dt} - \frac{1}{p}\frac{Dp}{Dt}\right) \tag{3.4}$$

for a perfect gas, where D/Dt is the material derivative. The flow is assumed to be isentropic, i.e. $Ds/Dt = 0$, which leads to,

$$\frac{\partial v_i}{\partial x_i} = -\frac{1}{\gamma p}\frac{Dp}{Dt} = -\frac{1}{\gamma}\frac{D}{Dt}\left[\ln\left(\frac{p}{p_\infty}\right)\right] \tag{3.5}$$

Making use of π, the conservation of mass takes the following form,

$$\frac{D\pi}{Dt} + \frac{\partial v_i}{\partial x_i} = 0 \tag{3.6}$$

In the same way, the conservation of momentum can be written as,

$$\frac{Dv_i}{Dt} + c^2\frac{\partial \pi}{\partial x_i} = 0 \tag{3.7}$$

where v_i is the velocity component in the i-direction. To linearize (3.6) and (3.7), the flow field is split up among four contributions, as also proposed by Lele [43] and Tam [79]

$$\begin{Bmatrix} \pi \\ v_i \end{Bmatrix} = \begin{Bmatrix} \bar{\pi} + \varepsilon_s \pi_s + \varepsilon_t \pi_t + \varepsilon_s \varepsilon_t \pi' \\ \bar{v}_i + \varepsilon_s v_{si} + \varepsilon_t v_{ti} + \varepsilon_s \varepsilon_t v' \end{Bmatrix} \tag{3.8}$$

where the overline denotes an average term, the subscripts s and t represent the perturbations due to the shock-cells and turbulence respectively, and the superscript $'$ accounts for the interaction between shock and turbulence, containing acoustic perturbations. ε_s and ε_t are two dimensionless parameters used to quantify the orders of magnitude of each perturbation. When inserting (3.8) into (2.1) and (3.7), only the terms of order $\varepsilon_s \varepsilon_t$ are kept. Indeed, the physical mechanism generating BBSAN is the interaction between shock-cells and turbulence, which makes sense for this approximation consistent. Especially, interaction of turbulence with itself (ε_t^2 terms) is neglected. Mixing noise is generally much weaker than shock-cell noise for the considered problem. The shock-cell structure is assumed to be fixed with time and thus satisfies the steady version of (3.5)-(3.7). Taking this into account, the unsteady linearized system is,

$$\begin{aligned} \frac{\partial \pi'}{\partial t} + \bar{v}_j \frac{\partial \pi'}{\partial x_j} + \frac{\partial v'_i}{\partial x_i} &= \theta \\ \frac{\partial v'_i}{\partial t} + \bar{v}_j \frac{\partial v'_i}{\partial x_j} + v'_j \frac{\partial \bar{v}_i}{\partial x_j} + \bar{c}^2 \frac{\partial \pi'}{\partial x_i} &= f_i^v + f_i^a \qquad i = 1,2,3 \end{aligned} \tag{3.9}$$

An interpretation of (3.9) is that a linear propagation operator is applied to the acoustic field, and source terms are identified on the right-hand side, namely,

$$\begin{aligned} \theta &= -v_{sj}\frac{\partial \pi_t}{\partial x_j} - v_{tj}\frac{\partial \pi_s}{\partial x_j} \\ f_i^v &= -v_{sj}\frac{\partial v_{ti}}{\partial x_j} - v_{tj}\frac{\partial v_{si}}{\partial x_j} \\ f_i^a &= -c_s^2\frac{\partial \pi_t}{\partial x_i} - c_t^2\frac{\partial \pi_s}{\partial x_i} \end{aligned} \tag{3.10}$$

Only f_i^v is of interest in the present study dealing with BBSAN. This term accounts for the interaction of the velocity perturbations due to shock-cells and turbulence. Consequently, f_i^a and θ are now neglected in what follows. The simplified system to be solved is finally given by,

$$\frac{\partial \pi'}{\partial t} + \overline{v_j}\frac{\partial \pi'}{\partial x_j} + \frac{\partial v_i'}{\partial x_i} = 0 \tag{3.11a}$$

$$\frac{\partial v_i'}{\partial t} + \overline{v_j}\frac{\partial v_i'}{\partial x_j} + v_j'\frac{\partial \overline{v_i}}{\partial x_j} + \overline{c}^2\frac{\partial \pi'}{\partial x_i} = f_i \tag{3.11b}$$

where f_i^v is simply written f_i.

3.3 Calculation of the vector Green functions

Since (3.11a)-(3.11b) is a linear differential system, the Green's functions technique is well suited. According to Duffy[26], one has to find a set of vectorial functions $\{\Pi_n, V_{ni},\ 0 \leq n \leq 3\}$ satisfying,

$$\frac{\partial \Pi_n}{\partial t} + \overline{v}_j\frac{\partial \Pi_n}{\partial x_j} + \frac{\partial V_{ni}}{\partial x_i} = \delta(\boldsymbol{x}-\boldsymbol{y})\delta(t-t_1)\delta_{0n} \tag{3.12a}$$

$$\frac{\partial V_{ni}}{\partial t} + \overline{v}_j\frac{\partial V_{ni}}{\partial x_j} + V_{nj}\frac{\partial \overline{v}_i}{\partial x_j} + \overline{c}^2\frac{\partial \Pi_n}{\partial x_i} = \delta(\boldsymbol{x}-\boldsymbol{y})\delta(t-t_1)\delta_{in} \tag{3.12b}$$

where δ is the Dirac distribution and δ_{in} is the Kronecker delta. Note that indices i and j are associated with the space dimension $1 \leq i, j \leq 3$, while n is linked to the number of scalar equations in system (3.9). Since there is no source term in (3.11a), $\Pi_0 = 0$ and $V_{0i} = 0$ for $1 \leq i \leq 3$. The acoustic pressure π' is directly related to the source terms through the following integral,

$$\pi'(\boldsymbol{x},t) = \int_{t_1}\int_{\boldsymbol{y}} \Pi_n(\boldsymbol{x},\boldsymbol{y},t-t_1) f_n(\boldsymbol{y},t_1)d\boldsymbol{y}dt_1 \tag{3.13}$$

The vector Green's functions in the absence of a mean flow are now derived. Physically, refraction due to the jet shear layer or any external flow surrounding the shocked jet is thus neglected. This approximation is discussed further in Chapter 5. The speed of sound is constant in the present case and $\overline{c} = c_\infty$. Mathematically, the mean velocity components are set to $\overline{v}_j = 0$ in (3.11a)-(3.11b), and the system is reduced to,

$$\frac{\partial \pi'}{\partial t} + \frac{\partial v_i'}{\partial x_i} = 0 \tag{3.14a}$$

$$\frac{\partial v_i'}{\partial t} + c_\infty^2\frac{\partial \pi'}{\partial x_i} = f_i \tag{3.14b}$$

System (3.14) describes the propagation of an acoustic perturbation due to a source term f_i in a medium at rest. The velocity fluctuations may be eliminated by combining (3.14a) and (3.14b) into,

$$\frac{\partial}{\partial t}(3.14a) - \frac{\partial}{\partial x_i}(3.14b) = \frac{\partial^2 \pi'}{\partial t^2} - c_\infty^2 \Delta \pi' = -\frac{\partial f_i}{\partial x_i} \tag{3.15}$$

to form the well-known d'Alembert wave operator equation, and where $-\nabla \cdot \boldsymbol{f}$ is a force source term. What is shown here, is that the pressure perturbation π' satisfies a set of ordinary differential equations (the LEE) as well as a wave equation. The free field Green's function $g_0(\boldsymbol{x}, t|\boldsymbol{y}, t_1)$ associated with the wave equation satisfies

$$\frac{\partial^2 g_0}{\partial t^2} - c_\infty^2 \Delta g_0 = \delta(\boldsymbol{x} - \boldsymbol{y})\delta(t - t_1) \tag{3.16}$$

This is the response of the medium at location $\boldsymbol{x}$ and time t for a pulse emitted at location $\boldsymbol{y}$ and time t_1. This function is given by [26],

$$g_0(\boldsymbol{x}, t|\boldsymbol{y}, t_1) = \frac{\delta(t - t_1 - |\boldsymbol{x} - \boldsymbol{y}|/c_\infty)}{4\pi|\boldsymbol{x} - \boldsymbol{y}|c_\infty^2} \tag{3.17}$$

and the formal solution to (3.16) can be expressed as,

$$\pi'(\boldsymbol{x}, t) = -\int_{t_1}\int_{\boldsymbol{y}} g_0(\boldsymbol{x}, \boldsymbol{y}, t - t_1)\nabla \cdot \boldsymbol{f}(\boldsymbol{y}, t_1) d\boldsymbol{y} dt_1 \tag{3.18}$$

Using properties of the convolution product, the divergence operator can be applied to the Green's function,

$$\pi'(\boldsymbol{x}, t) = \int_{t_1}\int_{\boldsymbol{y}} \left(\frac{\partial g_0}{\partial y_n}(\boldsymbol{x}, \boldsymbol{y}, t - t_1)\right) f_n(\boldsymbol{y}, t_1) d\boldsymbol{y} dt_1 \tag{3.19}$$

Direct comparison between (3.13) and (3.19) provides,

$$\Pi_n(\boldsymbol{x}, \boldsymbol{y}, t - t_1) = \frac{\partial g_0}{\partial y_n}(\boldsymbol{x}, \boldsymbol{y}, t - t_1) \tag{3.20}$$

This equation relates the vector Green's functions Π_n of the LEE to the free field Green's function g_0 of the wave equation. The next calculations are performed in the frequency domain. The following convention is used for the Fourier transform,

$$h(\omega) = \int_{-\infty}^{+\infty} h(t) e^{-i\omega t} dt \qquad h(t) = \frac{1}{2\pi}\int_{-\infty}^{+\infty} h(\omega) e^{i\omega t} d\omega \tag{3.21}$$

where $h(t)$ is a time signal and $h(\omega)$ is its Fourier transform. In the frequency domain, the vector Green's functions are given by,

$$\Pi_n(\boldsymbol{x}, \boldsymbol{y}, \omega) = \frac{\partial g_0}{\partial y_n}(\boldsymbol{x}, \boldsymbol{y}, \omega) \tag{3.22}$$

The free field Green's function in the frequency domain is straightforwardly computed,

$$g_0(\boldsymbol{x}, \boldsymbol{y}, \omega) = \frac{e^{-i\omega \frac{|\boldsymbol{x} - \boldsymbol{y}|}{c_\infty}}}{4\pi c_\infty^2 |\boldsymbol{x} - \boldsymbol{y}|} \tag{3.23}$$

After some algebra (details are reported in Appendix B.1), it can be shown that the Green's functions associated with the initial LEE system is,

$$\Pi_n(\boldsymbol{x}, \boldsymbol{y}, \omega) = \frac{e^{-i\omega|\boldsymbol{x} - \boldsymbol{y}|/c_\infty}}{4\pi c_\infty^2} \frac{i\omega}{c_\infty} \frac{x_n}{|\boldsymbol{x}|^2} \tag{3.24}$$

This expression relies on a far field approximation. The observation distance $|\boldsymbol{x}|$ is assumed to be much larger than the size of the source domain $|\boldsymbol{y}|$, that is $|\boldsymbol{y}|/|\boldsymbol{x}| \ll 1$, corresponding to the geometric far field assumption. Moreover, the observation distance is also much larger than the characteristic wavelength. For a nozzle diameter $D = 0.038$m at a jet Mach number $M_j = 1.15$, the lowest frequency of interest is around $f = 1000$Hz, which corresponds to a wavelength $\lambda = c/f \approx 10$D. Typical distances of observation range from 50D to 100D so that the acoustic far field condition is clearly met

Since π' is now known, π can be expanded asymptotically assuming small perturbations,

$$\pi = \frac{1}{\gamma} \ln \left(\frac{\overline{p} + p_s + p_t + p'}{p_\infty} \right) = \overline{\pi} + \frac{1}{\gamma} \left(\frac{p_s}{p_\infty} + \frac{p_t}{p_\infty} + \frac{p'}{p_\infty} \right) \tag{3.25}$$

Comparing (3.25) with the original expression of π leads to the approximation $p' = \gamma p_\infty \pi'$ and recalling that $c_\infty^2 = \gamma p_\infty / \rho_\infty$ gives $p' = \rho_\infty c_\infty^2 \pi'$. The final expression for the acoustic pressure as a function of the Green's functions and the source terms is

$$p'(\boldsymbol{x}, t) = \rho_\infty c_\infty^2 \int_{t_1} \int_{\boldsymbol{y}} \Pi_n(\boldsymbol{x}, \boldsymbol{y}, t - t_1) f_n(\boldsymbol{y}, t_1) \, d\boldsymbol{y} \, dt_1 \tag{3.26}$$

3.4 Estimation of the pressure correlation function

In this section, the pressure correlation function R_{pp} is formally derived. The pressure signal is treated as a random, time-dependent, signal. Physically, N acoustic pressure measurements will give N different spectra, but the signal is assumed to be stationary, which means that its statistical properties are constant over time. Mathematically, the k^{th} realization of this process is

$$p^{(k)}(\boldsymbol{x}, t) = \rho_\infty c_\infty^2 \int_{t_1} \int_{\boldsymbol{y}} \Pi_n(\boldsymbol{x}, \boldsymbol{y}, t - t_1) f_n^{(k)}(\boldsymbol{y}, t_1) \, d\boldsymbol{y} \, dt_1 \tag{3.27}$$

The randomness of the signal is due to the source terms, not to the deterministic Green's functions. It is more convenient to make use of the spectral Green's functions in (3.27), so that the acoustic pressure is given by

$$p^{(k)}(\boldsymbol{x}, t) = \frac{\rho_\infty c_\infty^2}{2\pi} \int_{t_1} \int_{\boldsymbol{y}} \int_{\omega} \Pi_n(\boldsymbol{x}, \boldsymbol{y}, \omega) f_n^{(k)}(\boldsymbol{y}, t_1) e^{i\omega(t-t_1)} d\omega d\boldsymbol{y} dt_1 \tag{3.28}$$

The pressure correlation function over time is obtained by taking the following ensemble average,

$$\begin{aligned} R_{pp}(\boldsymbol{x}, \tau) &= < p^{(k)}(\boldsymbol{x}, t) p^{*(k)}(\boldsymbol{x}, t + \tau) > \\ &= \lim_{N \to +\infty} \frac{1}{N} \sum_{k=1}^{N} p^{(k)}(\boldsymbol{x}, t) p^{*(k)}(\boldsymbol{x}, t + \tau) \end{aligned} \tag{3.29}$$

where the star superscript stands for a complex conjugate. Replacing the pressure terms by their explicit expressions, the pressure correlation function is given by

$$\begin{aligned} R_{pp}(\boldsymbol{x}, \tau) = \left(\frac{\rho_\infty c_\infty^2}{2\pi} \right)^2 \int \ldots \int \Pi_n(\boldsymbol{x}, \boldsymbol{y_1}, \omega_1) \Pi_m^*(\boldsymbol{x}, \boldsymbol{y_2}, \omega_2) < f_n(\boldsymbol{y_1}, t_1) f_m(\boldsymbol{y_2}, t_2) > \times \ldots \\ e^{i[\omega_1(t-t_1) - \omega_2(t+\tau-t_2)]} d\omega_1 d\omega_2 d\boldsymbol{y_1} d\boldsymbol{y_2} dt_1 dt_2 \end{aligned} \tag{3.30}$$

In this expression, the time variable t can take any value. It will have no influence on the final result as will be shown below, thanks to the statistical stationarity of the signals.

3.5 Estimation of the Power Spectral Density

The Power Spectral Density (PSD) is the time Fourier transform of $R_{pp}(\boldsymbol{x},\tau)$. One has,

$$S_{pp}(\boldsymbol{x},\omega)=\left(\frac{\rho_\infty c_\infty^2}{2\pi}\right)^2\int\dots\int \Pi_n(\boldsymbol{x},\boldsymbol{y_1},\omega_1)\Pi_m^*(\boldsymbol{x},\boldsymbol{y_2},\omega_2) < f_n(\boldsymbol{y_1},t_1)f_m(\boldsymbol{y_2},t_2) > \times\dots$$
$$e^{i[\omega_1(t-t_1)-\omega_2(t-t_2)-(\omega+\omega_2)\tau]}d\omega_1 d\omega_2 d\boldsymbol{y_1}d\boldsymbol{y_2}dt_1dt_2d\tau \tag{3.31}$$

The integration over τ and ω_2 are straightforward. Moreover, the change of variables,

$$(t_1,t_2)\mapsto\begin{cases}t_1=t_1\\ \tau=t_2-t_1\end{cases} \tag{3.32}$$

completes the integration over t_2. The PSD is given by,

$$S_{pp}(\boldsymbol{x},\omega)=\frac{(\rho_\infty c_\infty^2)^2}{2\pi}\int\dots\int \Pi_n(\boldsymbol{x},\boldsymbol{y_1},\omega_1)\Pi_m^*(\boldsymbol{x},\boldsymbol{y_2},-\omega) < f_n(\boldsymbol{y_1},t_1)f_m(\boldsymbol{y_2},t_1+\tau) > \times\dots$$
$$e^{i[-(\omega_1+\omega)t_1+\omega_1 t+\omega(t-\tau)]}d\omega_1 d\boldsymbol{y_1}d\boldsymbol{y_2}dt_1d\tau \tag{3.33}$$

Since the sources are stationary, their correlation function depends only on location and time difference, i.e.

$$< f_n(\boldsymbol{y_1},t_1)f_m(\boldsymbol{y_2},t_1+\tau) > = R_{nm}(\boldsymbol{y_1},\boldsymbol{\eta},\tau) \tag{3.34}$$

where $\boldsymbol{\eta}=\boldsymbol{y_2}-\boldsymbol{y_1}$ is the vector joining two sources. The notations are illustrated in Figure 3.1. Substitution of this expression into the PSD and integrating over t_1 and ω_1 gives,

$$S_{pp}(\boldsymbol{x},\omega)=(\rho_\infty c_\infty^2)^2\int\dots\int \Pi_n(\boldsymbol{x},\boldsymbol{y_1},-\omega)\Pi_m^*(\boldsymbol{x},\boldsymbol{y_1}+\boldsymbol{\eta},-\omega)R_{nm}(\boldsymbol{y_1},\boldsymbol{\eta},\tau)e^{-i\omega\tau}d\boldsymbol{y_1}d\boldsymbol{\eta}d\tau \tag{3.35}$$

Using an asymptotic expansion of the vector Green's functions (details in Appendix B.2) with respect to $\boldsymbol{\eta}$, one has

$$\Pi_m^*(\boldsymbol{x},\boldsymbol{y}+\boldsymbol{\eta},-\omega)\backsimeq\Pi_m^*(\boldsymbol{x},\boldsymbol{y},-\omega)e^{i\frac{\omega}{c_\infty}\frac{\boldsymbol{x}.\boldsymbol{\eta}}{|\boldsymbol{x}-\boldsymbol{y}|}} \tag{3.36}$$

The exponential factor is the phase factor accounting for the retarded time difference for an observer located at $\boldsymbol{x}$ and two source terms located at $\boldsymbol{y_1}$ and $\boldsymbol{y_1}+\boldsymbol{\eta}$. Substitution of this expression into the PSD,

$$S_{pp}(\boldsymbol{x},\omega)=\frac{\rho_\infty^2\omega^2}{16\pi^2c_\infty^2}\frac{1}{R^2}\int\dots\int\frac{x_nx_m}{R^2}R_{nm}(\boldsymbol{y_1},\boldsymbol{\eta},\tau)e^{i\omega\left(\frac{1}{c_\infty}\frac{\boldsymbol{x}.\boldsymbol{\eta}}{R}-\tau\right)}d\boldsymbol{y_1}d\boldsymbol{\eta}d\tau \tag{3.37}$$

where $|\boldsymbol{x}-\boldsymbol{y}|\approx|\boldsymbol{x}|=R$. The computation of S_{pp} requires R_{nm} to be known, which is the subject of the next section.

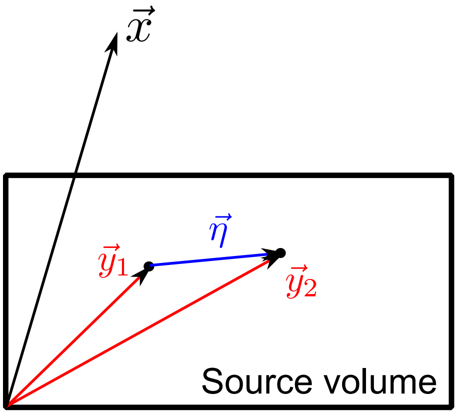

Figure 3.1: Illustration of the integration variables for the PSD

3.6 Estimation of the source term correlation

The initial expression for the source terms in (3.11b) is

$$f_i = -v_{sj}\frac{\partial v_{ti}}{\partial x_j} - v_{tj}\frac{\partial v_{si}}{\partial x_j} \tag{3.38}$$

According to the continuity for the shock-cell structure,

$$\overline{v}_j\frac{\partial \pi_s}{\partial x_j} + \frac{\partial v_{si}}{\partial x_i} = 0 \tag{3.39}$$

which gives,

$$v_{si} \sim \overline{v}\pi_s \tag{3.40}$$

Using dimensional analysis and the previous equation,

$$f_i \sim \overline{v}\pi_s\frac{v_{ti}}{l} + \overline{v}\pi_s\frac{v_{tj}}{l} \tag{3.41}$$

where l is the local characteristic length scale of turbulence in the streamwise direction. Turbulence will be modeled using a classical two-equation turbulence model, for which anisotropic effects are difficult to correctly capture. Assuming that the BBSAN source terms are isotropic appears to be a reasonable level of approximation. Therefore,

$$f_i(\boldsymbol{y_1}, t) = f(\boldsymbol{y_1}, t) \text{ for } 1 \leq i \leq 3 \tag{3.42}$$

Finally,

$$f(\boldsymbol{y_1}, t) = \frac{p_s(\boldsymbol{y_1})v_t(\boldsymbol{y_1}, t)}{\rho_\infty c_\infty l(\boldsymbol{y_1})} \tag{3.43}$$

The source terms being isotropic, so is the correlation function. Hence $R_{nm}(\boldsymbol{y_1}, \eta, \tau) = R_{iso}(\boldsymbol{y_1}, \eta, \tau)$ for $n = m$ and there is no contribution of the terms for $n \neq m$. As a result,

$$\frac{x_n x_m}{R^2}R_{nm}(\boldsymbol{y_1}, \boldsymbol{\eta}, \tau) = \frac{x_1^2 + x_2^2 + x_3^2}{R^2}R_{iso}(\boldsymbol{y_1}, \boldsymbol{\eta}, \tau) = R_{iso}(\boldsymbol{y_1}, \boldsymbol{\eta}, \tau) \tag{3.44}$$

	c_τ	c_l	$c_\perp$
Tam [84]	0.233	0.256	1
Morris & Miller (screeched jet) [56, 57]	1.25	3.25	0.30
Morris & Miller (un-screeched jet) [56, 57]	0.85	3.00	0.30

Table 3.1: Scaling constants for the correlation function R_v

Inserting (3.43) into (3.34),

$$R_{iso}(\boldsymbol{y_1}, \eta, \tau) = \frac{p_s(\boldsymbol{y_1})p_s(\boldsymbol{y_1}+\boldsymbol{\eta})}{\rho_\infty^2 c_\infty^2 l(\boldsymbol{y_1})^2} < v_t(\boldsymbol{y_1}, t_1) v_t(\boldsymbol{y_1}+\boldsymbol{\eta}, t_1+\tau) > \tag{3.45}$$

where the ensemble average $< >$ applies only on unsteady terms and l was considered as constant over the distance $\boldsymbol{\eta}$. p_s will be determined directly from the RANS calculation, whereas $< v_t(\boldsymbol{y_1}, t_1) v_t(\boldsymbol{y_1}+\boldsymbol{\eta}, t_1+\tau) >$ requires some modeling. It represents the correlation of the turbulent velocity fluctuations and is modeled after Tam [84] by,

$$R_v(\boldsymbol{y_1}, \boldsymbol{\eta}, \tau) = k(\boldsymbol{y_1}) \exp\left[-\frac{|\xi|}{u_c\tau_s} - \frac{(\xi-u_c\tau)^2}{l^2} - \frac{\gamma^2+\zeta^2}{l_\perp^2}\right] \tag{3.46}$$

where $\boldsymbol{\eta} = (\xi, \gamma, \zeta)$ is the distance between two source terms, k is the turbulence kinetic energy, τ_s is the characteristic time scale of turbulence and $l_\perp$ is the characteristic length scale of turbulence in the cross stream direction, u_c is the local convection velocity. This expression was chosen because it makes the analytical computation of S_{pp} easier. Morris & Miller [56, 57] and Miller & Morris [50, 53, 52] used an alternative form, but this resulted in more complex analytical calculations afterwards: they had to compute the Fourier transform of the static pressure along the jet axis, which may be cumbersome in some cases. The isotropic correlation is now given by,

$$R_{iso}(\boldsymbol{y_1}, \boldsymbol{\eta}, \tau) = k(\boldsymbol{y_1})\frac{p_s(\boldsymbol{y_1})p_s(\boldsymbol{y_1}+\boldsymbol{\eta})}{\rho_\infty^2 c_\infty^2 l(\boldsymbol{y_1})^2} \exp\left[-\frac{|\xi|}{u_c\tau_s} - \frac{(\xi-u_c\tau)^2}{l^2} - \frac{\gamma^2+\zeta^2}{l_\perp^2}\right] \tag{3.47}$$

The characteristic scales are determined thanks to the RANS calculation of the jet flow. Using dimensional analysis, Tam [84] suggested that,

$$\tau_s = c_\tau \frac{k}{\varepsilon} \quad l = c_l \frac{k^{3/2}}{\varepsilon} \quad l_\perp = c_\perp l \tag{3.48}$$

where c_τ, c_l and $c_\perp$ are constants. Several sets of constants were tried, they are shown in Table 3.1. The constants proposed by Morris and Miller for a screeched jet were finally retained.

The final expression for the PSD is determined by substitution of (3.47) into (3.37) and integrating over τ at fixed ξ, giving

$$\begin{aligned} S_{pp}(\boldsymbol{x}, \omega) = \frac{\omega^2}{16\pi\sqrt{\pi}c_\infty^4 R^2} \int_{\boldsymbol{y}} \int_{\boldsymbol{\eta}} \frac{k}{l u_c} \exp\left(-\frac{\omega^2}{4}\frac{l^2}{u_c^2}\right) p_s(\boldsymbol{y})p_s(\boldsymbol{y}+\boldsymbol{\eta}) \times \ldots \\ \exp\left(-i\frac{\omega\xi}{u_c}\right) \exp\left[-\frac{|\xi|}{u_c\tau_s} - \frac{\gamma^2+\zeta^2}{l_\perp^2}\right] \exp\left(i\frac{\omega}{c_\infty}\frac{x_1\xi+x_2\gamma+x_3\zeta}{R}\right) d\boldsymbol{\eta} d\boldsymbol{y} \end{aligned} \tag{3.49}$$

3.7 Implementation

Equation (3.49) consists in a double spatial integral over the BBSAN source domain, that is the jet flow. It is implemented in Fortran 90. The shock pressure p_s is given by subtracting the ambient pressure from the computed static pressure in the jet. The convection velocity is approximated by the local mean velocity.

A flow chart describes the structure of the BBSAN code, see Figure 3.2. In order to reduce computation times, some numerical filters are used. For example, cells where $k < 900$ m^2.s^{-2} are not included in the calculation, because they are not expected to contribute significantly to BBSAN.

3.8 Conclusion

Following the work of Morris & Miller [57], a model has been developed to predict BBSAN from a statistical approach. A convenient decomposition of the LEE exhibited the sources of BBSAN, as the interaction of shocks and turbulence. These elements are known through a RANS calculation, and propagation of sound is achieved with the free field Green's function.

At this stage, the main difference with Morris and Miller's model [56] is that the Fourier transform of the static pressure along the jet axis has not been used here. Morris and Miller argued that this resulted in a simpler numerical implementation, which is true, because it simplifies the final expression for the PSD: the PSD here requires the evaluation of 6 spatial integrals, whereas Morris and Miller only use 3 spatial integrals and one along the spatial wave number.

It should be noted that computing the Fourier transform with a fast algorithm such as FFT requires an equally spaced mesh in the jet direction. If the original CFD mesh does not meet this requirement, it is possible to interpolate the original mesh to a regular grid, as Morris and Miller did. Consequently, the Morris and Miller's approach is probably more efficient for academic configurations. On the other hand, industrial geometries are dual-stream and include a plug (a cone-shaped part in the center of the primary flow). Then, the flows are not parallel to the jet axis but follow the plug slopes. The FFT technique may not be so proficient then, compared to the approach described here.

The next chapter deals with the application of the model, from the RANS computation of the mean turbulent flow, to the comparison of calculated spectra with measurements.

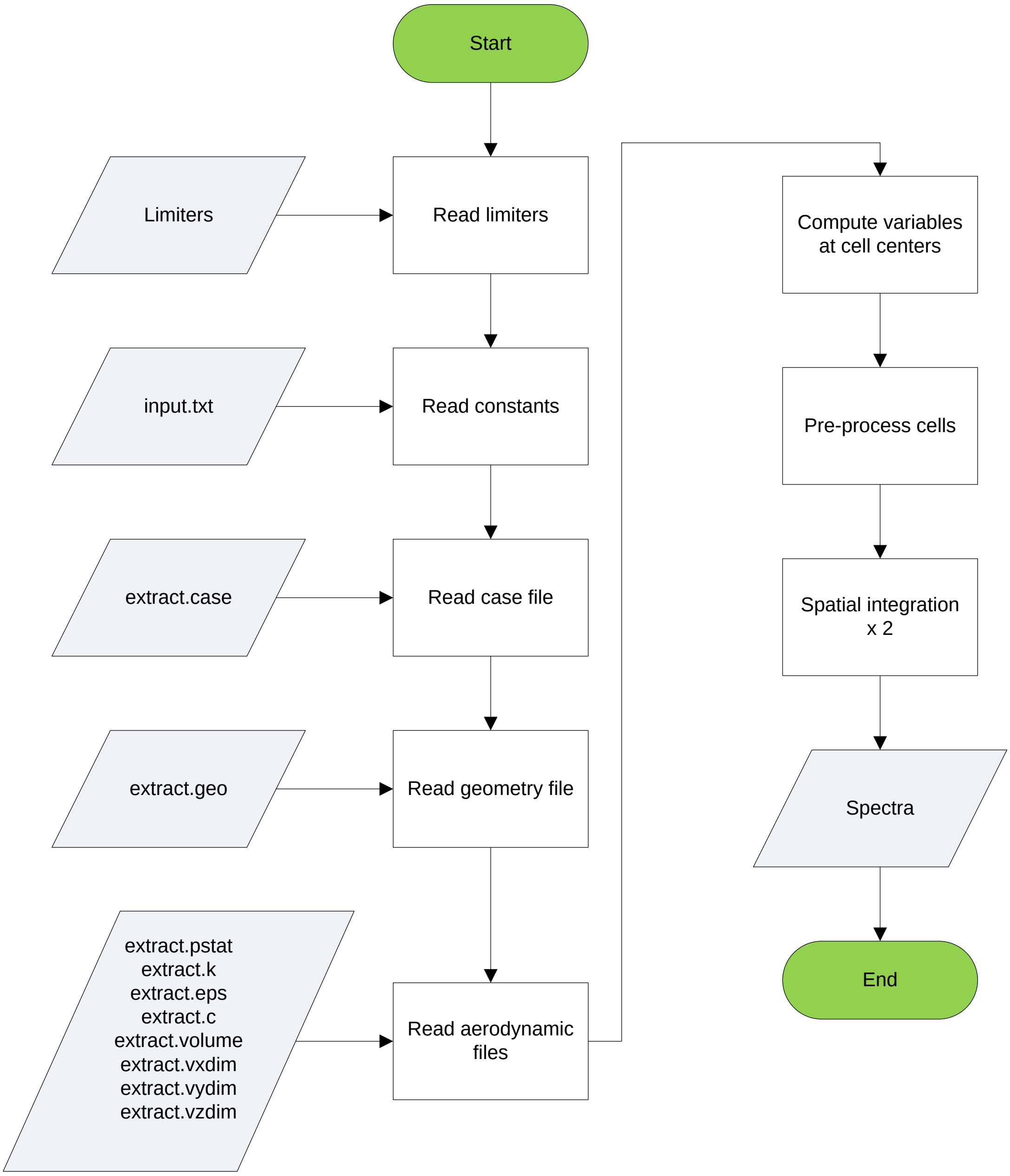

Figure 3.2: Structure of the acoustic program

Chapter 4

BBSAN of static jets

This chapter describes the aerodynamic and acoustic results concerning static single-stream jets without refraction effects. This is the first step in assessing the model on more complex configurations. The computational case is described first, then the numerical choices are presented. Aerodynamic results are shown and compared to measurements to ensure the validity of the calculation. Finally the correlation of acoustic predictions with measurements is discussed.

4.1 Case description

Single-stream jets are typical academic configurations. A thorough test campaign has been conducted at Ecole Centrale de Lyon by André *et al.* [5, 6, 4] to characterize BBSAN and flight effects. Measurements include aerodynamic quantities (static pressure, Particle Image Velocimetry, Schlieren imaging) as well as acoustic data (near and far field spectra). The case presented here is a convergent nozzle, whose exit diameter is $D = 0.038$ m. The nozzle lines are presented in Figure 4.1. The jet issuing from this nozzle will be computed with RANS CFD at Mach numbers ranging from $M_j = 1.0$ to $M_j = 1.5$.

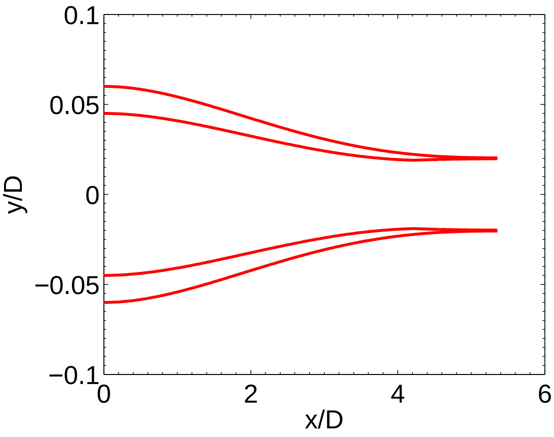

Figure 4.1: Geometry of the single-stream nozzle

4.2 Aerodynamic preprocessing

The classical steps involved in the preprocessing of an aerodynamic calculation are described here. They are: the choice of a mesh topology, grid generation, boundary conditions and the numerical procedure.

4.2.1 Mesh topology

The mesh is a $2D$ axisymmetric multi-block structured mesh: it is composed of several blocks, each block being structured. Any node is represented by a unique set of integers (i, j). As a result, the neighboring nodes are simply given by shifting i or j by ± 1. This makes the implementation of numerical spatial schemes easier than in an unstructured case. The drawback is that it usually takes longer to mesh a complex geometry with a structured mesh.

The multi-block structure is shown in Figure 4.2. It is a closeup of the nozzle lip. The nozzle is in black (it is not meshed), whereas each colored part indicates a specific block. The nozzle lip is a strong generator of instabilities, because the internal and external flows traveling at different speeds meet at this point. As a result, instabilities form and are convected downstream. It is not possible to render this phenomenon in a RANS simulation, because it only computes the steady part of the flow. As a result, if instabilities appear in the RANS calculation, they will not be physical and will even prevent the calculation from converging. This is why the nozzle lip was meshed using a C-grid topology, as shown by the yellow block in Figure 4.2. This topology was found to be more robust to deal with lip instabilities.

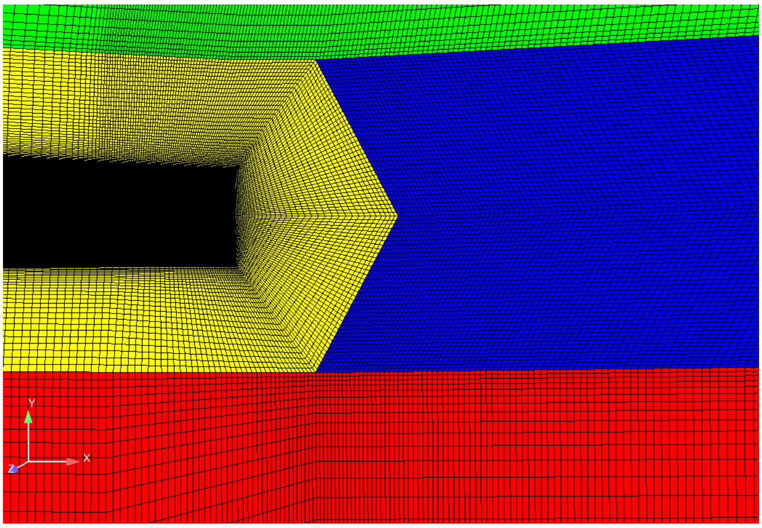

Figure 4.2: Closeup of the C-grid topology at the nozzle lip

The domain size is set to prevent any reflection problem at the boundaries. It typically extends 50D downstream of the nozzle exit and extends 20D radially. The nozzle exit is located at $x/D = 0$ and the axis of symmetry is $y/D = 0$.

4.2.2 Grid generation

The grid is generated using ICEM software by ANSYS. The size of the cells in a given region is determined by the physical phenomenon to be captured.

Axial direction

In the first diameters downstream of the jet exit, it is essential to correctly capture the location of the shocks and their amplitude. This determines the cell size in the axial direction in the shock region, set to

$$10^{-5} \leq \frac{\Delta x}{D} \leq 10^{-1}, \quad \frac{\Delta y}{D} \simeq 10^{-3} \tag{4.1}$$

where Δx is the cell size in the jet direction. The smallest cells are obviously located close to the nozzle exit, and there are 30 points per shock-cell for the first shock-cells.

Radial direction

In the radial direction, there are two phenomena to be captured: the mixing layer between the jet and the ambient medium, and the boundary layer on the inside and outside of the nozzle.

To correctly capture a boundary layer, the driving parameters are the number of points in the radial direction and the distance to the wall from the first node. A common practice is to take at least 20 points in the boundary layer, which was done here. The distance to the wall from the first node is determined using a dimensionless distance to the wall defined by

$$y^+ = \frac{y v_\tau}{\nu} = \frac{y}{\nu / v_\tau} \tag{4.2}$$

where v_τ is the friction velocity and ν is the fluid viscosity. Bailly and Comte-Bellot [12] state that

$$\frac{v_\tau}{v_\infty} \simeq 4\% \tag{4.3}$$

where v_∞ is the free stream velocity. The classical rule is to impose a dimensionless value $y^+ = 1$ for the first cell height, which leads to the physical size

$$y = \frac{\nu}{0.04 v_\infty} \tag{4.4}$$

for the first cell height. For a typical flow velocity of 300m/s in the nozzle, this leads to $y = 1.25 \times 10^{-6}$m.

A sufficient number of points should be used in the developing mixing layer as well. Candel [17] relates the mixing layer width δ to the axial position in the jet by,

$$\frac{\delta}{D} = 0.153 \left(\frac{x}{D} \right) + 0.002 \tag{4.5}$$

For instance, at $x/D = 1$, $\delta/D \simeq 15/100$. At least 20 points were used in the mixing layer region and the typical cell height was set to $\Delta y/D = 10^{-3}$.

Applying the aforementioned criteria produces a mesh containing approximately 150 000 nodes.

4.2.3 Boundary conditions

The different boundaries are shown in Figure 4.3. Boundary A is the nozzle inlet and boundary B is the inlet for the external flow. For these boundaries, the conditions are given by the stagnation pressure and enthalpy, that are directly related to the operating conditions. The boundary value of $(\rho k)_\infty$ and $(\rho\omega)_\infty$ should also be specified for turbulence to be generated. For this, the turbulence intensity I_k is defined as

$$I_k = \frac{\sqrt{\overline{v'^2}}}{v_\infty} = \frac{\sqrt{2/3k}}{v_\infty} \tag{4.6}$$

Here, v_∞ represents the velocity at the nozzle inlet, before the flow is accelerated. It is determined with the area-Mach law given in the first chapter. I_k simply compares the turbulent velocity fluctuations with the mean velocity v_∞. The assumption is made that $I_k \simeq 10\%$ in the nozzle. This value gives good results for the development of turbulence in the jet as will be seen later on. For the external flow, I_k is consistently set to a smaller value of 1%. Then, $(\rho k)_\infty$ is found using,

$$(\rho k)_\infty = \frac{3}{2}\rho_\infty v_\infty^2 I_k^2 \tag{4.7}$$

$(\rho\omega)_\infty$ is estimated with,

$$(\rho\omega)_\infty = \frac{\rho_\infty(\rho k)_\infty}{\mu_t} \tag{4.8}$$

where μ_{t_∞} is the user-defined eddy viscosity at the nozzle inlet. In elsA, the initial eddy viscosity for the whole flow field is set as a fraction of the fluid viscosity, i.e. the user sets the ratio μ_{t_∞}/μ. A parametric study was conducted and the best results were obtained for $\mu_{t_\infty}/\mu = 100$ at the nozzle inlet and $\mu_{t_\infty}/\mu = 50$ at the inlet of the external domain.

The stagnation conditions at boundary B obviously depend on the speed of the external flow surrounding the jet, if any. Strictly speaking, since static jets are considered here, there is no inflow at boundary B. Nonetheless, for numerical reasons, it is not possible to use a null velocity at boundary B. This would make the calculation unstable. The workaround is to use a numerical coflow, with a small Mach number M_{coflow} compared to the jet Mach number. This numerical artifact has an experimental counterpart: in a test facility, when the jet exits in a quiescent medium, the ambient air surrounding the jet is sucked in, thus inducing a slow coflow as well. The value given to M_{coflow} is determined in Section 4.2.4.

For regions C and D, a pressure boundary condition is applied, and an axis condition is applied to region E. The walls of the nozzle have an adiabatic wall boundary condition.

4.2.4 Numerical procedure

The calculation is organized around three main steps.

Step 1: computation of a laminar solution

The initial field is uniform (the Mach number is set to 0.3 everywhere), the aerodynamic variables are set to their free stream values. The flaw of this initial field is that it does

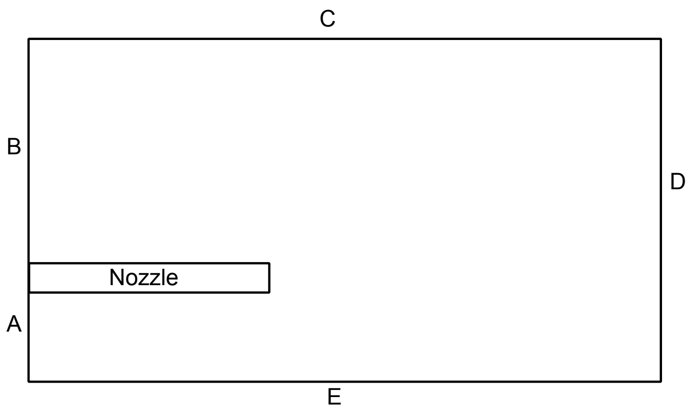

Figure 4.3: Region of application of boundary conditions

not satisfy the conservation laws (the flow is uniform throughout the nozzle, which is physically impossible). Nonetheless, it is not possible to create a more realistic field from scratch with the available tools. Directly solving the turbulent RANS problem from this field often leads to divergence, especially for supersonic flows, so a laminar solution is computed at first. The slope limiter in the Roe scheme is set to *null* and 5 000 iterations are performed. This results in a laminar field with consistent velocity profiles in the nozzle. Since there is no turbulence, the jet development is not realistic in this step but this is the purpose of the next step. It is sometimes possible to skip this step and directly compute a turbulent field (step 2).

Step 2: approximation of the RANS solution

Starting from the previously computed field, a second calculation of 20 000 iterations is performed. The turbulence model is switched on (a $k-\omega-\text{SST}$ model is used), the slope limiter is still *null* and the coflow is set to a target value ($M_{\text{coflow}} = 0.03$ for a static case). At the end of this step, the jet is properly developed, though the aerodynamic variables are over-damped by the *null* slope limiter.

Step 3: final step

The slope limiter is switched to *Van Albada* which is much softer: the shock-cell damping is reduced and the cells may shift a little bit axially. The numerical coflow may still be reduced if necessary. After 10 000 iterations, convergence is reached.

4.3 Aerodynamic results

The numerical procedure is applied to the case described in Section 4.1. Results concern Schlieren visualizations, static pressure profiles, turbulence profiles, Mach number and shock-cell evolution. These numerical results are compared with measurements by André [3], and good agreement is found. This is essential, because the acoustic model will be based on this data.

4.3.1 Schlieren visualization

Schlieren imaging is an experimental technique which allows to capture density gradient variations. Schlieren visualization is very convenient to show the shock-cell structure of the jet and its evolution with M_j. Numerically, Schlieren can be mimicked by plotting the norm of the density gradient.

Case $M_j = 1.15$

In Figure 4.4, Schlieren visualization for a jet at $M_j = 1.15$ is shown. The calculation is in the upper part, and the measurement in the lower part. The jet flows from left to right and color gradients represent density gradients in the jet. The overall agreement is good.

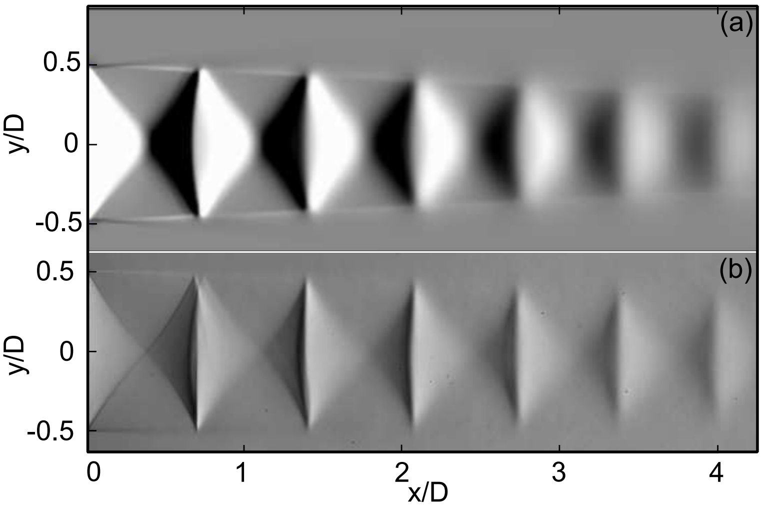

Figure 4.4: Average view of Schlieren images of a $M_j =$ 1.15 jet. (a): calculation (b): measurement [7]

Case $M_j = 1.35$

Comparing Figure 4.4 with Figure 4.5, where a $M_j = 1.35$ jet is shown, provides insightful information. The shock-cells lengthen in the second case and the shocks become stronger. The free jet boundary is also altered: the angle of the expansion fan at the nozzle exit increases when increasing M_j. The free jet boundary in the first shock-cell bends and results in a barrel-like shape. The strength of the shocks decreases downstream, so that the next shock-cells look like those for the $M_j = 1.15$ jet.

Case $M_j = 1.5$

The last comparison concerns a $M_j = 1.5$ underexpanded jet. The shocks are even stronger than in the previous case, and the barrel shape of the first shock-cell is more visible. The angle of the expansion fan attached to the nozzle lip is increased. In the first cell, the intersection of the intercepting shock, the Mach disk and the reflected shock form a triple point. It is clearly visible on the measurement, but in the calculation the Mach disk is damped.

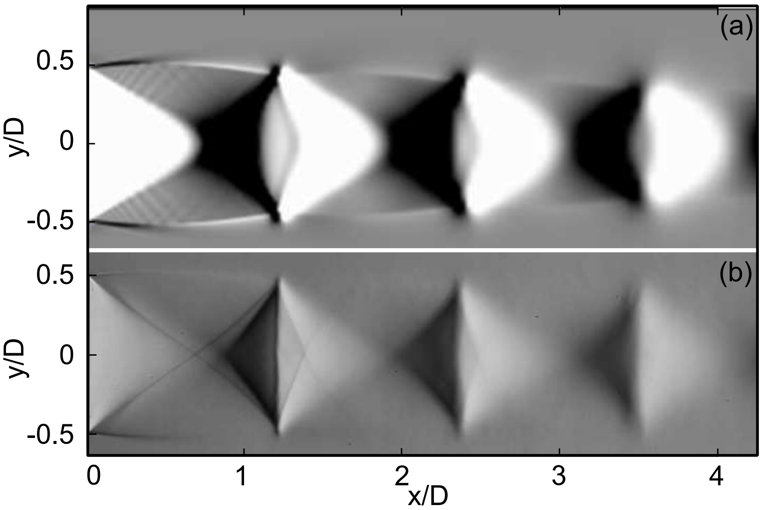

Figure 4.5: Average view of Schlieren images of a $M_j = 1.35$ jet. (a): calculation (b): measurement [7]

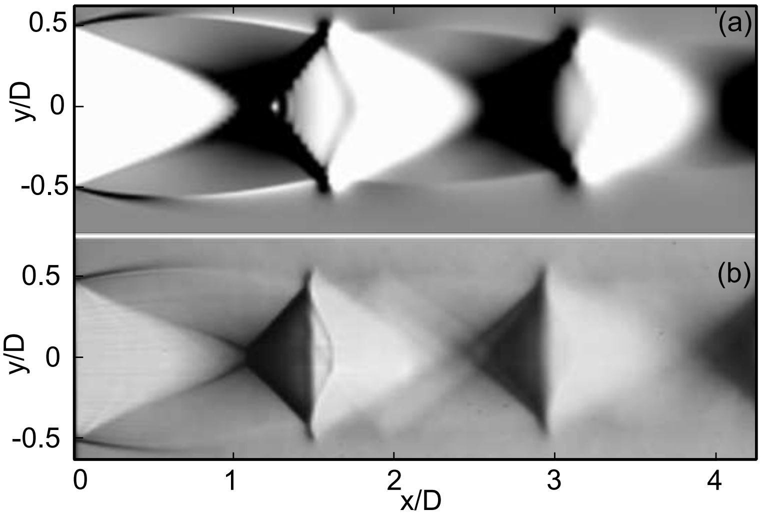

Figure 4.6: Average view of Schlieren images of a $M_j = 1.5$ jet. (a): calculation (b): measurement [7]

4.3.2 Static pressure

The static pressure is an essential quantitative variable: it is a direct input for the acoustic model. It also characterizes the spatial structure of shocks as well as their strength. The calculations are compared to measurements made by André [3]. First of all, it should be noted that measuring the total and static pressure in a supersonic jet cannot be done using a classical Pitot tube. Indeed, when using a Pitot tube in a supersonic flow, a shock will form ahead of the probe. Without any other modification, this results in an incorrect value for the total pressure measured at the tip of the tube. This issue was addressed by Pinckney [64] and Norum & Seiner [60]. They both designed conical shaped probes, accounting for the shock forming ahead of the probe. Similar designs were used by André for the measurements at ECL. Another specificity of these probes is that their operating conditions are limited to a supersonic flow, which means that they will produce incorrect results for transonic flows. More information on the probes can be found in reference [3].

Case $M_j = 1.15$

The case of a $M_j = 1.15$ jet is examined first. The static pressure on the jet axis is shown in Figure 4.7, where measurements and calculations are compared. The agreement is excellent. The shock locations are correctly predicted by the calculation. The trend in amplitude decay is similar between measurements and calculation, though the CFD solution slightly overestimates the shock damping. Numerical dissipation is probably responsible for this difference. It should be noted that the presence of shocks in the jet flow requires some numerical dissipation to be added on purpose. This is the role of the limiter used with the Roe scheme. The numerical dissipation should be strong enough to ensure the convergence of the calculation, but as low as possible not to flatten the shocks. For $x/D > 6$, p_{stat}/p_∞ tends to unity in the calculation and to a lower value experimentally, which may look surprising. This difference probably stems from the pressure probe: it is designed to work at supersonic Mach numbers, and for $x/D > 6$ the flow becomes transonic. Hence, far downstream the probe is out of its operating range, which may explain the difference.

Radial profiles are shown in Figures 4.8, 4.9, and 4.10, at respectively $x/D = 0.157$, $x/D = 0.342$, and $x/D = 0.528$. The overall agreement is very good. A systematic discrepancy is observed at $y/D = 0.4$. It is believed that this is due to a flow-probe interaction: at this position, the probe is close enough to the mixing layer, so that the shock at the probe tip may reach the mixing layer, reflect on it, and interact downstream with the probe, thus creating such discrepancies. When exiting the jet, the static pressure reaches the ambient pressure in both calculation and measurements, which is consistent.

Case $M_j = 1.35$

The case $M_j = 1.35$ is shown in Figure 4.11. The shock-cells are longer than in the previous case, and the shocks are stronger: measured values of p_{stat}/p_∞ peak around 1.1 for $M_j = 1.15$, whereas the peak value for $M_j = 1.35$ is more than 1.4. As before, the freestream experimental value of p_{stat}/p_∞ is shifted with respect to the calculation.

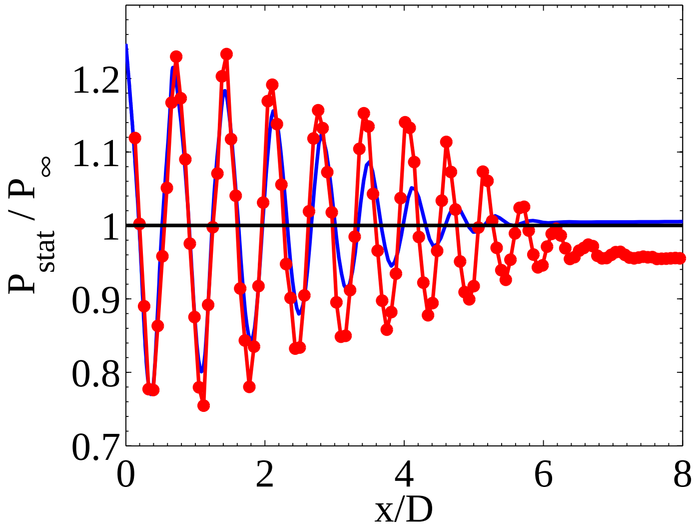

Figure 4.7: Static pressure on the jet axis, $M_j = 1.15$. —— calculations, —●— measurements

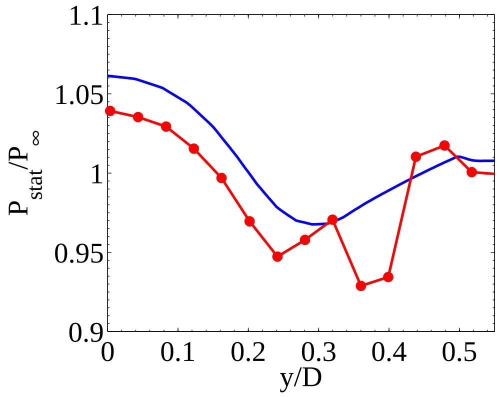

Figure 4.8: adial profiles of static pressure, $M_j = 1.15$, $x/D = 0.157$. —— calculations, —●— measurements

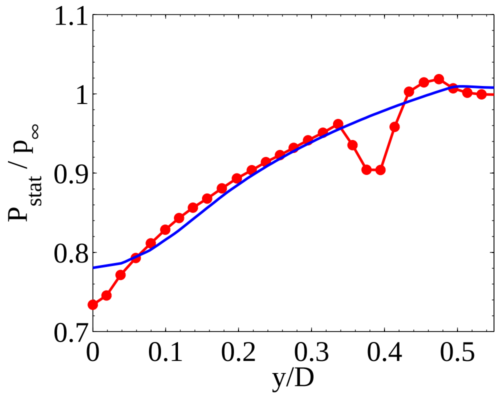

Figure 4.9: Radial profiles of static pressure, $M_j = 1.15$, $x/D = 0.342$. —— calculations, —●— measurements

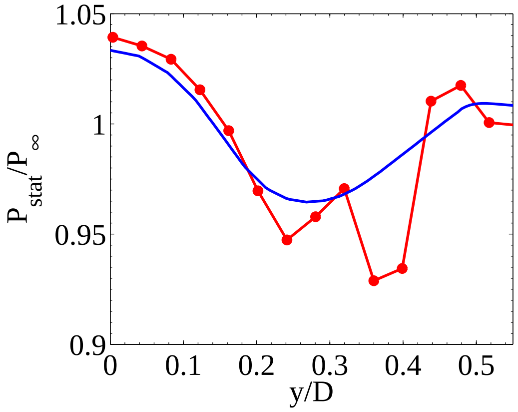

Figure 4.10: Radial profiles of static pressure, $M_j = 1.15$, $x/D = 0.528$. —— calculations, —●— measurements

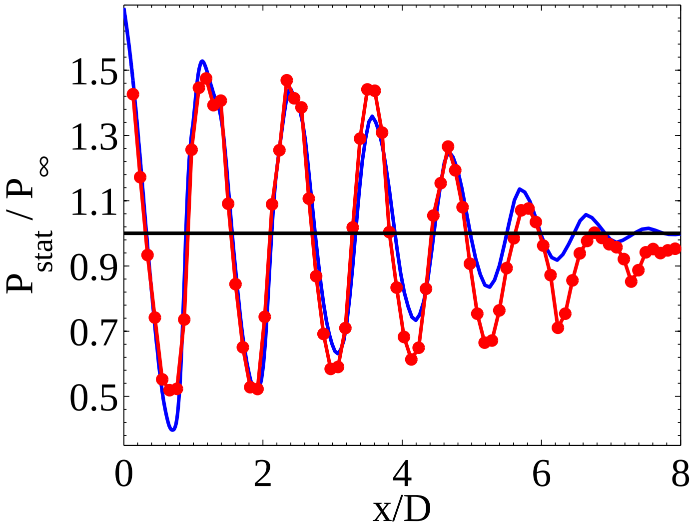

Figure 4.11: Static pressure on the jet axis, $M_j = 1.35$. —— calculations, —●— measurements

4.3.3 Turbulence

Since the calculations use a $k-\omega-$SST turbulence model, turbulence is assumed to be locally isotropic. The velocity fluctuations in the RANS calculation are given by,

$$v'_x = \sqrt{\frac{2}{3}k} \tag{4.9}$$

This is the velocity fluctuation used for comparison with measurements. Substantial research has been conducted on turbulence in jets. Davies *et al.* [24] studied subsonic jets at $M_j < 0.6$ with hot-wire measurements. Fleury [31] used PIV to characterize turbulence in subsonic jets at $M_j = 0.6$ and $M_j = 0.9$. Morris and Zaman [58] studied the statistical properties of turbulence (second and fourth order velocity correlations, length scales) of a jet at $M_j = 0.26$. Lau *et al.* [41] used laser velocimeter and hot-wire anemometer techniques, to obtain radial and center-line distributions of the axial and radial, mean and fluctuating velocities.

The data provided by André and Lau *et al.* is used here for comparison. In the ECL test campaign, mean and fluctuating velocity are acquired using PIV at $M_j = 1.15$ and $M_j = 1.35$. Though the jet is operated in static conditions, a low speed external flow is used in the PIV measurements by André. This is achieved using a secondary nozzle, coaxial to the main nozzle, as explained earlier in 1.3.1. The Mach number of the external flow is $M_{\text{ext}} = 0.05$. As detailed before, a numerical coflow $M_{\text{coflow}} = 0.03$ is set around the jet. Since M_{ext} and M_{coflow} are the same order of magnitude, the results may be directly compared.

$M_{\text{ext}} = 0.05$ $(17m/s)$ is also the typical speed of the flow induced by a jet exhausting into still air in a closed facility such as CEPRA 19 (ONERA facility). Unpublished work at Snecma shows that the effect of the induced flow is to reduce jet noise by approximately 1 dB. Though negligible here, this phenomenon should be taken into account when comparing acoustic measurements from open and closed wind facilities.

Case $M_j = 1.15$

The computed velocity fluctuations along the x-axis are now compared to PIV measurements by André [3], for $M_j = 1.15$. The results are shown in Figure 4.12, the calculations are in the upper part, the measurements in the lower part. Condensation formed in the jet core during measurements, resulting in some unphysical values for v'_x, from $x/D = 3$ near the jet axis. These values should be ignored for the comparison. Several observations can be made.

From these two visualizations, turbulence clearly stems from the nozzle lip, located at $X/D = 0$ and $Y/D = 0.5$. In the calculation, velocity fluctuations are very small throughout the jet core, whereas shocks induce velocity fluctuations in the measurements. One can distinguish the shock structure in the measurements but not in the calculations. However, those fluctuations are small, compared to values in the mixing layer. The lower part of the mixing layer is bent by the shocks, this is more visible in the measurements than in the calculations. Turbulence spreads out a bit more rapidly in the calculations than in the measurements.

Another indicator of velocity fluctuations compared to the jet velocity is given by

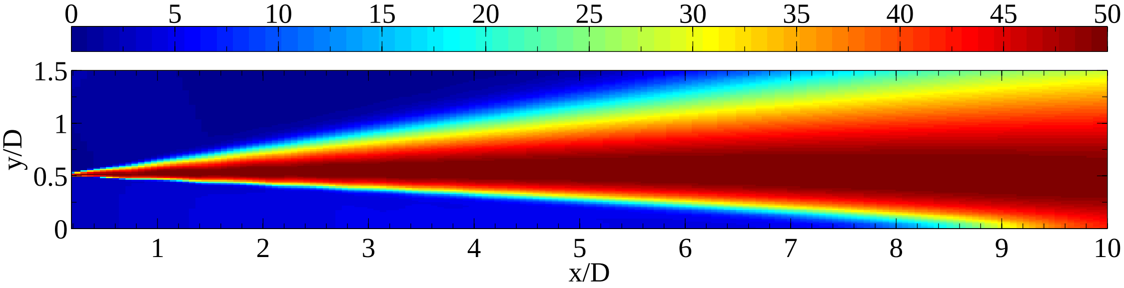

(a)

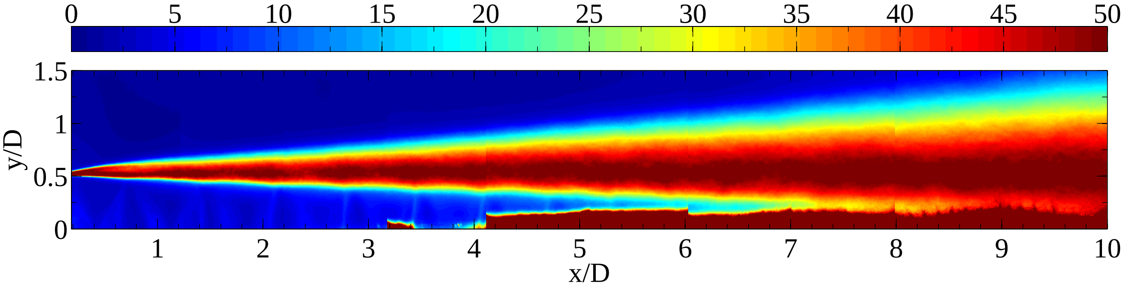

(b)

Figure 4.12: Visualization of v'_x (m/s), $M_j = 1.15$. (a) calculations, (b) measurements [3]

turbulence intensity, or turbulence rate, I_k, computed by

$$I_k = \frac{v'_x}{U_j} \tag{4.10}$$

where U_j is the isentropic jet velocity. Only axial velocity fluctuations are considered here. Profiles of the calculated turbulence rate on the jet axis are plotted in Figure 4.13. The axial distance is non-dimensionalized by the potential core length, as suggested by Lau *et al.* [41]. The calculation is compared to measurements by Lau *et al.* only, because condensation in the jet core at $M_j = 1.15$ in André's measurements prevents any computation of I_k along the jet axis. Lau *et al.* investigated on jets at $M_j = 0.9$ and $M_j = 1.37$. The supersonic jet is perfectly expanded, so no shock-turbulence interaction is to be expected in their measurements. In Figure 4.13, I_k remains low till the end of the potential core ($x/x_c < 1$) and then sharply rises. I_k peaks around 13% at approximately two potential core lengths, and then softly decreases.

The axial profile of I_k on the jet lip-line ($y/D = 0.5$) is shown in Figure 4.14. Both calculation and measurements by André predict a rather flat evolution of I_k along the x-axis, around a 15% value. The humps between $X/D = 0$ and $X/D = 5$ reflect the interaction of the shock-cell structure with the boundary layer. Fleury [31] observed a similar flat evolution of I_k in the mixing-layer.

The radial profiles of I_k are shown in Figure 4.15. The data are plotted versus the non-dimensional parameter $\eta^* = (y - y_{0.5})/x$ as done by Lau *et al.* [41], where $y_{0.5}$ is the radial distance at which the velocity is half the velocity on the jet axis. Thus, $\eta^* = 0$ corresponds to the half velocity point. Measurements include those by Lau *et al.* [41] and

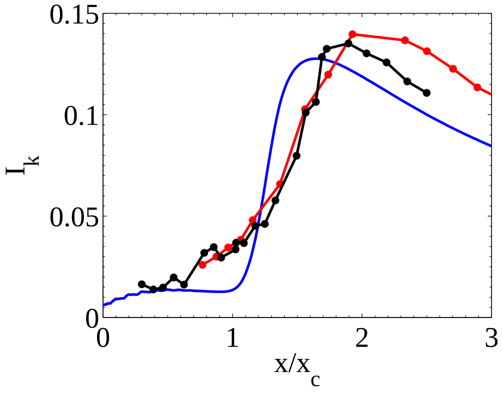

Figure 4.13: Axial turbulence rate on the jet axis, $M_j = 1.15$. —— calculations, measurements [41]: —●— $M_j = 0.9$, —●— $M_j = 1.37$

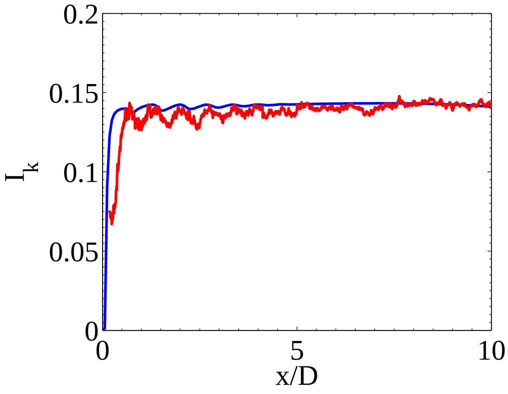

Figure 4.14: Axial turbulence rate, $y/D = 0.5$, $M_j = 1.15$. —— calculations, —— measurements [3]

André [3] at various radial locations and for different M_j. With this representation, all data collapses pretty well. I_k peaks between 14% and 19% at $\eta^* = 0$, the half-velocity point. Comparison between calculations and measurements by André gives good results. As noticed before, turbulence spreads out radially a bit more in the calculations than in the measurements. The computed I_k is higher than the measured I_k for $\eta^* > 0$.

Hence, the $k-\omega-$SST model predicts realistic levels of I_k and a reasonable spreading of the jet.

Case $M_j = 1.35$

The velocity fluctuations are presented in Figure 4.16 for $M_j = 1.35$. There is no condensation at this operating condition so that the data by André [3] may be fully exploited. It is clear from these visualizations that turbulence in the mixing layer is affected by the presence of shock-cells: the mixing layer is bent by the shocks, and this is more visible in the measurements. Turbulence extents are also increased compared to the $M_j = 1.15$ case, which may be explained by stronger velocity gradients in the mixing layer. Quantitative information is provided in Figure 4.17 where the evolution of I_k on the jet axis is presented. Peaks of I_k are measured, whereas forward facing steps only are observed in the calculation. The $k-\omega-$SST turbulence model is not able to correctly predict the decrease of I_k behind the shocks.

I_k is tracked along the lip line in Figure 4.18. The match between calculations and measurement is good. I_k oscillates around 15% but with stronger amplitude than for $M_j = 1.15$. The tip of the mixing layer, attached to the nozzle lip, is bent upward by the strong expansion fan. As a result, points right after the nozzle exit ($x/D < 1$), on the lip line ($y/D = 0.5$), are still in the jet core, rather than in the mixing layer. Farther downstream ($x/D > 1$) on the lip line, points are in the mixing layer. This explains the initial low value of I_k followed by a sharp rise.

The radial evolution of I_k is shown in Figure 4.19. Calculations at $x/D = 2$ and $x/D = 10$ are compared to measurements by André at the same M_j and locations and to measurements by Lau *et al.* at $x/D = 2$ and $x/D = 4$ with $M_j = 1.37$. The overall

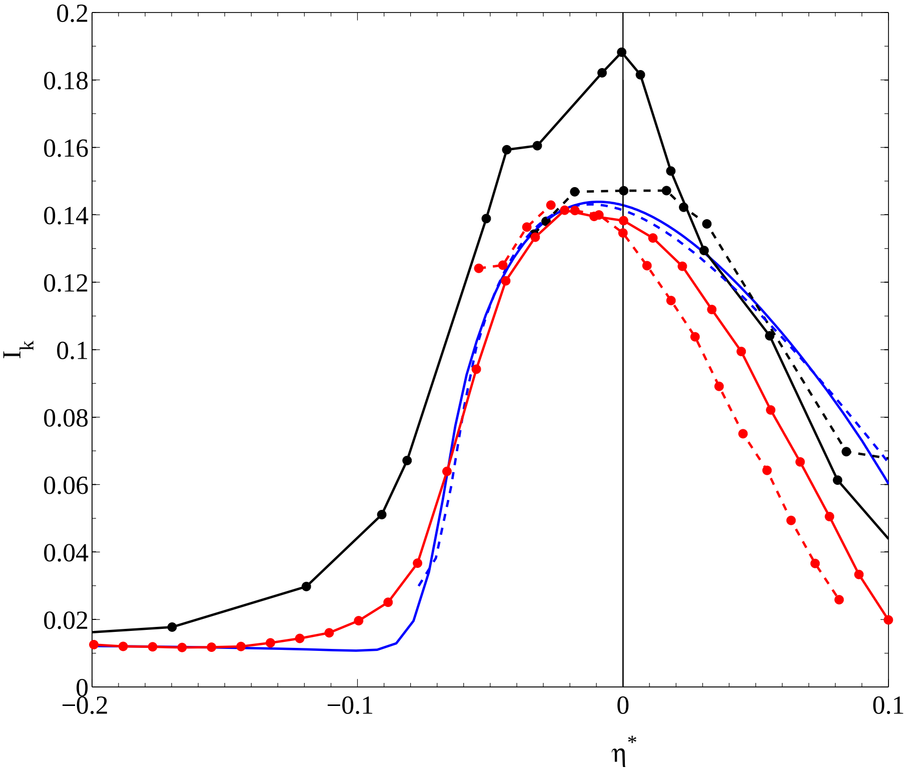

Figure 4.15: Radial profiles of I_k versus $\eta^* = (y - y_{0.5})/x$. Calculations at $M_j = 1.15$: —— $x/D = 2$, - - - $x/D = 12$. Measurements at $M_j = 0.9$ [41]: —●— $x/D = 2$, - ● - $x/D = 12$. Measurements at $M_j = 1.15$ [3]: —●— $x/D = 2$, - ● - $x/D = 9.8$

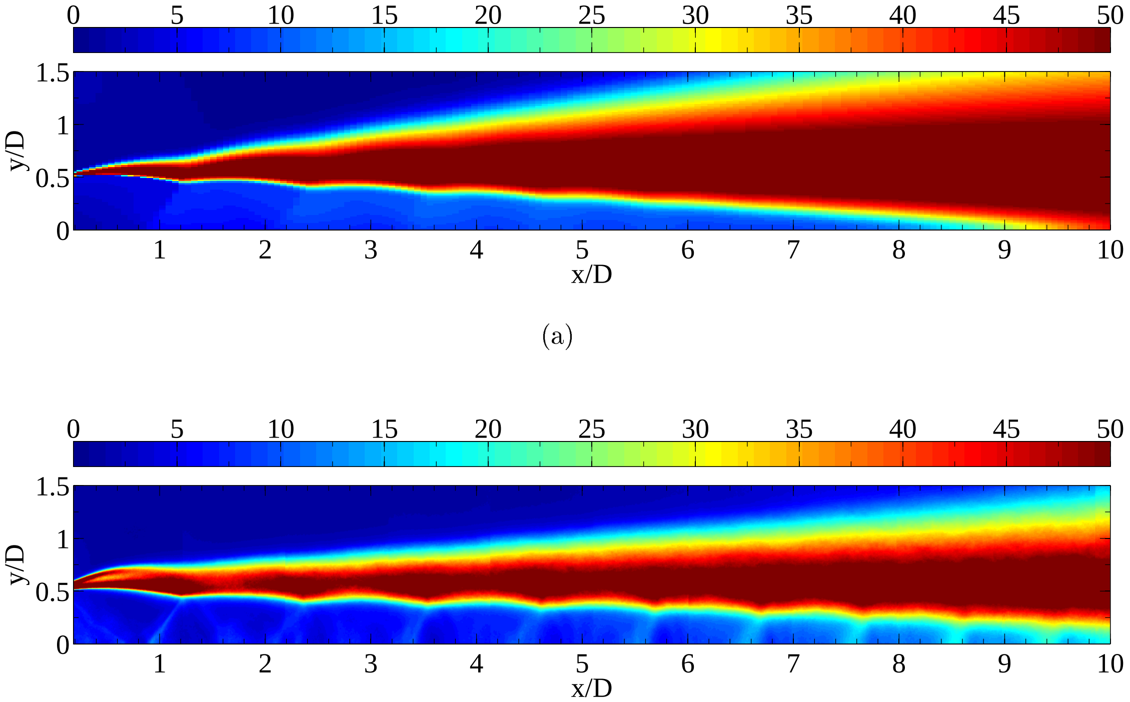

(a)

(b)

Figure 4.16: Visualization of v_x' (m/s), $M_j = 1.35$. (a) calculations, (b) measurements [3]

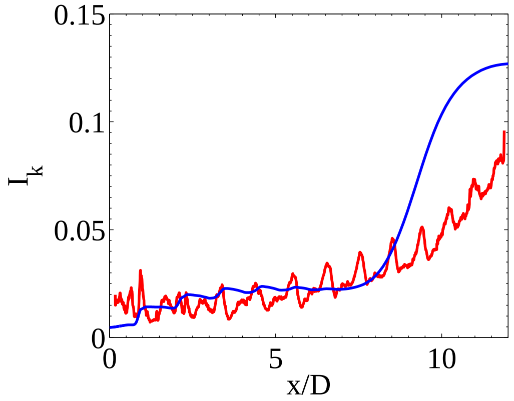

Figure 4.17: Axial turbulence rate on the jet axis, $M_j = 1.35$. —— calculations, —— measurements [3]

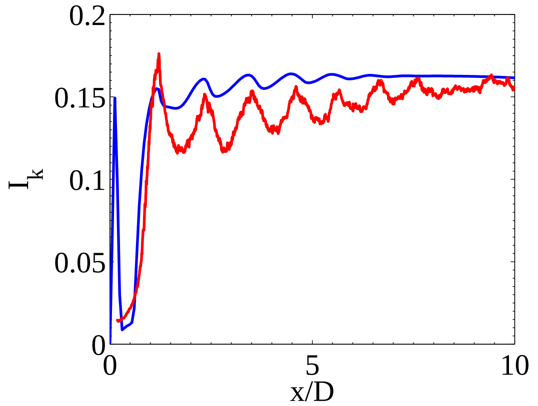

Figure 4.18: Axial turbulence rate, $y/D = 0.5$, $M_j = 1.35$. —— calculations, —— measurements [3]

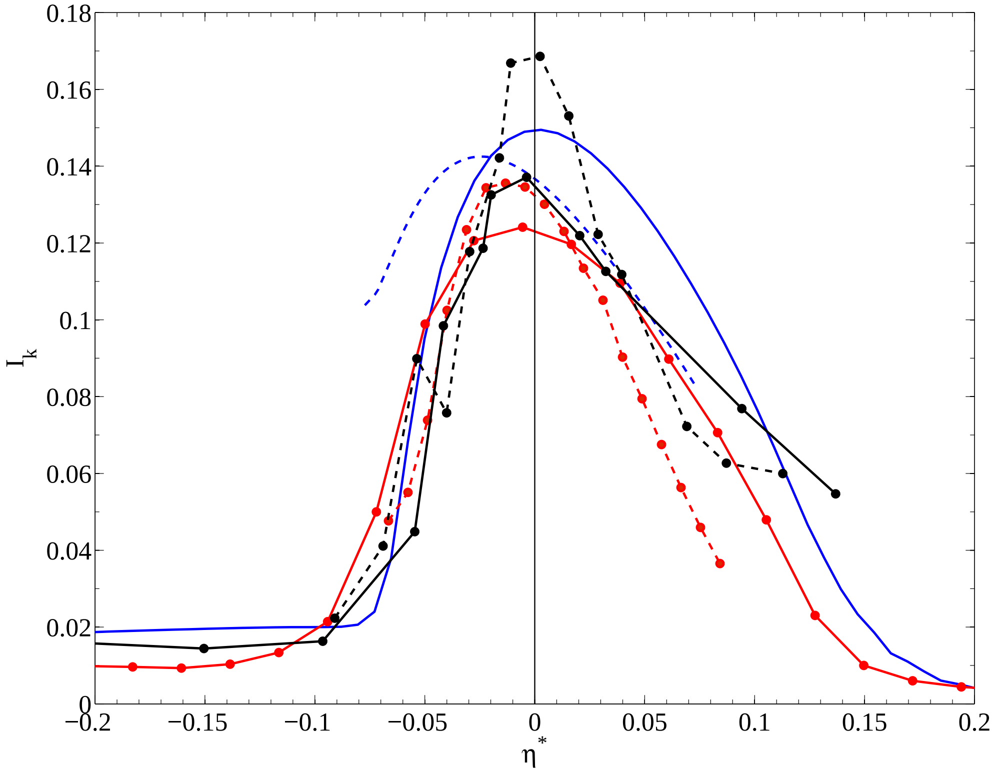

Figure 4.19: Radial profiles of I_k versus $\eta^* = (y - y_{0.5})/x$. Calculations at $M_j = 1.35$: —— $x/D = 2$, - - - $x/D = 10$. Measurements at $M_j = 1.37$ [41]: —●— $x/D = 2$, - ● - $x/D = 4$. Measurements at $M_j = 1.35$ [3]: —●— $x/D = 2$, - ● - $x/D = 10$

collapse of data is good. There is no clear trend when changing M_j or x/D, but a general conclusion would be that I_k decreases when increasing M_j and moving downstream.

4.3.4 Mach number

The evolution of the local Mach number at $M_j = 1.15$ is shown in Figure 4.20. The iso-lines $M = 1$ are also plotted. It is interesting to notice that the whole jet remains supersonic up to $x/D = 7$, except in the first shock-cell, where a small subsonic region exists, behind a normal shock. There are no subsonic regions in the next cells, that is no normal shock. This is because normal shocks are strong shocks, and the shocks in the downstream cells are rather weak.

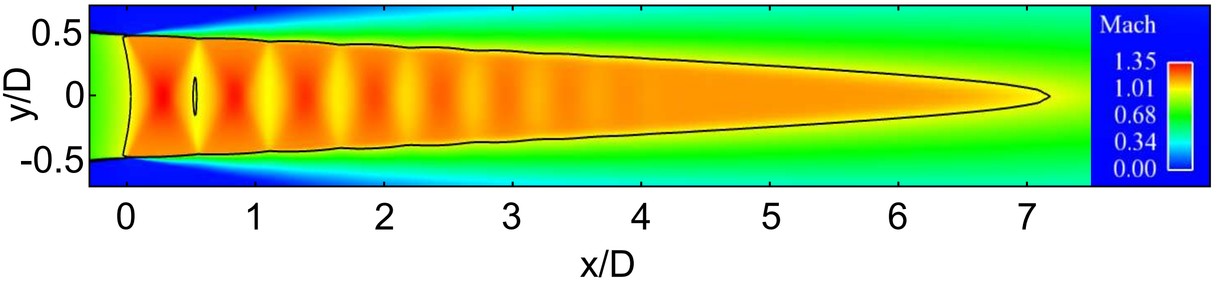

Figure 4.20: Visualization of the Mach number at $M_j = 1.15$, with iso-lines $M = 1$

The evolution of the Mach number on the jet axis for $M_j = 1.15$ is presented in Figure 4.21. The calculation is compared to measurements. Experimentally, the Mach number is determined with a pressure probe, from the static and total pressure. The local Mach number oscillates around the isentropic jet Mach number $M_j = 1.15$ in the shock-cells. After the last shock-cell, the jet Mach number equals M_j in the calculation.

4.3.5 Length and strength of the shock-cells

The evolution of the non-dimensional, individual shock-cell length $L_s/\beta D$ is shown in Figure 4.22, for measurements and calculations. The global trend is a decrease in the

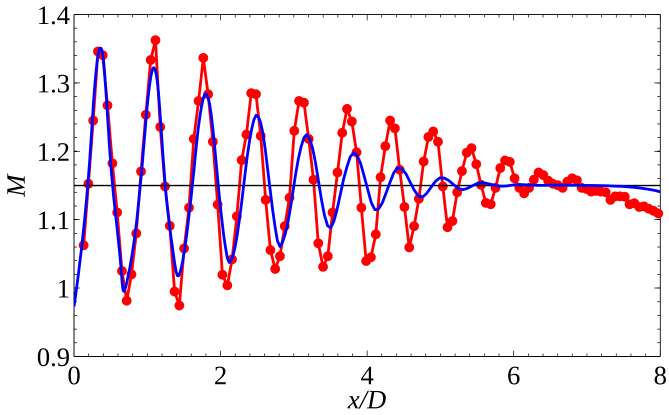

Figure 4.21: Mach number on the jet axis, $M_j = 1.15$.
—— calculations, —— measurements

shock-cell length when the shock number increases. This comes from the gradual destruction of the periodic structure by turbulence. A linear regression on the measurements was performed and it lead to $L_s = 1.325\beta D$ for the first shock, and a decay of $0.044\beta D$ per shock. The regression fits both measurements and calculations correctly. Hence, the length of the n^{th} shock-cell may be approximated by,

$$L_n = 1.325\beta D - 0.044(n-1)\beta D \tag{4.11}$$

which compares favorably to the expression proposed by Harper-Bourne & Fisher [33].

Shock-cell strength in a cell is defined after Seiner & Norum [75] by,

$$\text{shock-cell strength} = \frac{p_M - p_m}{p_m} \tag{4.12}$$

where p_M and p_m are respectively the maximum and minimum static pressure in a given cell. The study of shock strengths provides information on the amplitude of BBSAN sources. Indeed, according to Harper-Bourne & Fisher [33] those two variables are directly proportional. Shock-cell strengths have been computed for the calculations and the results are shown in Figure 4.23. As expected, shocks are stronger for $M_j = 1.35$ than for $M_j = 1.15$, which is logical because the pressure mismatch in the jet is higher at $M_j = 1.35$. For a given M_j, shock strength decreases downstream: as for shock-cell length, turbulence in the mixing-layer weakens downstream shocks.

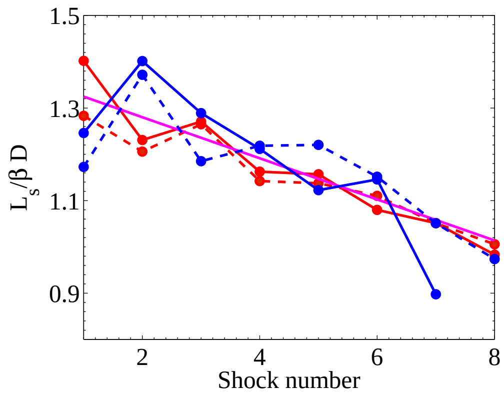

Figure 4.22: Shock-cell length versus shock-number. Measurements: - ● - $M_j = 1.15$, —●— $M_j = 1.35$. Calculations: - ● - $M_j = 1.15$, —●— $M_j = 1.35$

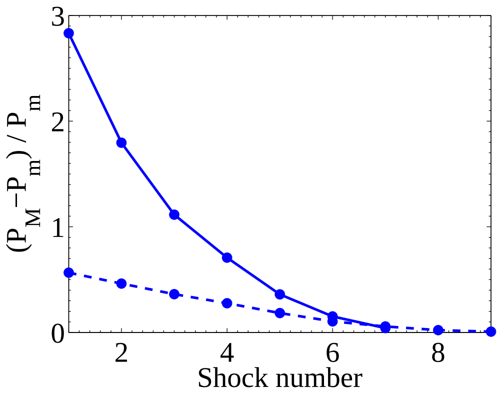

Figure 4.23: Calculated shock stength: - ● - $M_j = 1.15$, —●— $M_j = 1.35$

4.3.6 Discussion

RANS calculations of supersonic shocked jets in static conditions have been extensively compared to measurements. The overall agreement is good, especially for the shock location and strength. Turbulence levels are also realistic. This provides a solid basis to use this data as input for the acoustic model, as will be done in the next section.

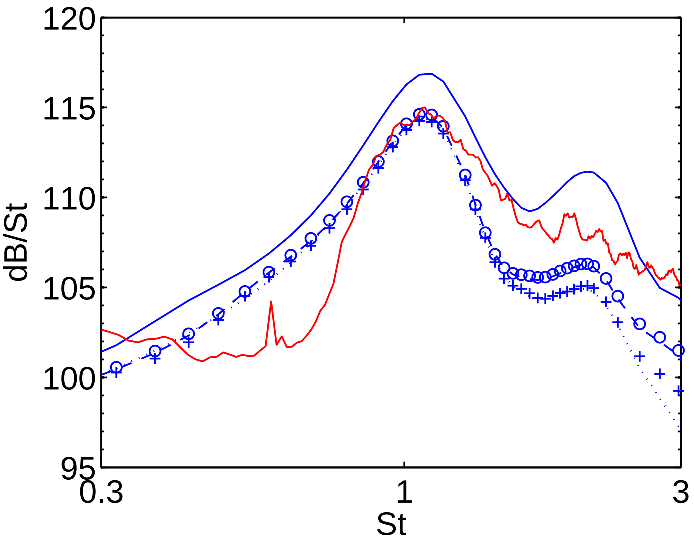

Figure 4.24: SPLs at $M_j = 1.15$, $\theta = 110°$ for various grid parameters $n_I \times n_J$. ——: 250×25, - - - : 250×50, ⋯: 250×100, +: 150×50, ○ : 350×50 —— measurements [3]

4.4 Acoustic results

The BBSAN model developed in Chapter 3 is applied to the cases described above. First, a grid convergence study is carried out, to determine the best grid parameters. Then, the model is assessed at two M_j. SPLS are computed and compared to measurements, and visualization of acoustics sources are shown.

4.4.1 Grid convergence

The spatial integration described in Equation (3.49) is not carried out on the entire CFD domain. Indeed, integration is restricted to $0 \leq x/D \leq 10$ and $0 \leq y/D \leq 1$, where BBSAN sources are expected to be located. As for any numerical integration, the number of grid points has an influence on the final result. The influence of the number of grid points is shown in Figure 4.24. Computed SPLs at $M_j = 1.15$ and $\theta = 110°$ are shown and compared to measurements. There are n_I points along the jet axis, and n_J points in the radial direction.

First, consider the curves with fixed n_I ($n_I = 250$) and varying n_J. This exhibits the influence of the mixing layer discretization, where shocks interact with turbulence. $n_J = 50$ is a good compromise to reach convergence: $n_J = 25$ is clearly not sufficient, whereas $n_J = 100$ does not change significantly the SPL. For a more general approach, $\overline{\delta}$, the average mixing layer width between $0 \leq x/D \leq 8$ is computed. Then, the number of grid points in the mixing-layer n_δ is,

$$n_\delta = n_J \frac{\overline{\delta}}{D} = 38 \tag{4.13}$$

Such a number of points suffices to reach grid convergence in the radial direction.

Now, consider the curves at fixed n_J ($n_J = 50$), with varying n_I. This isolates the influence of shock-cell discretization. Convergence is reached for $n_I = 250$. In the calculations at $M_j = 1.15$, shock-cells extend up to $x/D = 6$ and there are 9 shock-cells, see Figure 4.7. Thus the average shock-cell length is $\overline{L}_s/D \simeq 0.67$. For $n_I = 250$, this means that there are approximately 16 grid points per shock-cell.

These criteria are used for subsequent calculations.

4.4.2 Results

Case $M_j = 1.15$

The first results concern a jet at $M_j = 1.15$. This Mach number is a typical value of the secondary stream of a civil engine. The PSDs were computed using Equation (3.49). A Strouhal representation is used: let $f_c = u_j/D$ be a characteristic frequency of the jet, then the frequencies (in Hertz) are divided by f_c to get a Strouhal representation. A $10\log_{10}(f_c)$ factor is added to the PSDs: the PSDs are in dB/St and energy is thus preserved.

Four observation angles Φ (inlet angle, $\Phi = \pi - \theta$) were computed, from the upstream to the downstream direction. PSDs are shown in Figure 4.25, and calculations are compared to measurements by André [3]. The first encouraging result is that the peak frequency is correctly captured numerically for all observer locations: f_p increases with inlet angle, both experimentally and numerically. Experimentally, the emergence of BBSAN diminishes as Φ increases, which is also the case with the computations. On quantitative grounds, the shape of the hump is generally well captured, especially for $\Phi = 70°$ (see Figure 4.4.2) and $\Phi = 90°$ (see Figure 4.4.2). The fact that the calculated PSDs agree well with measurements for low frequencies ($St < 0.5$ for $\Phi = 50°$) is a coincidence: at such low frequencies, mixing noise is dominant and the model is not expected to account for mixing noise.

The proposed model makes it easy to study the sources of BBSAN. By plotting the elementary contributions of Equation (3.49) for a given frequency, Figures 4.26 and 4.27 are produced. Iso-lines of static pressure are plotted in white on these figures. Iso-lines are convenient to observe that source terms are located along the shock-cell boundary, in the mixing layer. The source domain extends from the nozzle exit to the downstream region, up to $x/D = 6$ for low frequencies and up to $x/D = 2$ only, for highest frequencies.

At $f = 3000$ Hz (see Figure 4.4.2), sources stand essentially at the tip of each shock-cell, as assumed by Harper-Bourne & Fisher [33] in their model. Nonetheless, at higher frequencies such as $f = 10000$ Hz (see Figure 4.4.2), sources appear to spread all along the the shock-cell boundary.

Source characteristics vary with frequency. Close to the peak frequency, sources are strong and widely spread, see Figure 4.4.2. As frequency increases, sources weaken, which corresponds to the decay observed on the PSD in Figure 4.4.2. High frequency sources are located close to the nozzle lip: this is because fine-scale turbulence, producing high frequencies, is predominant in this region.

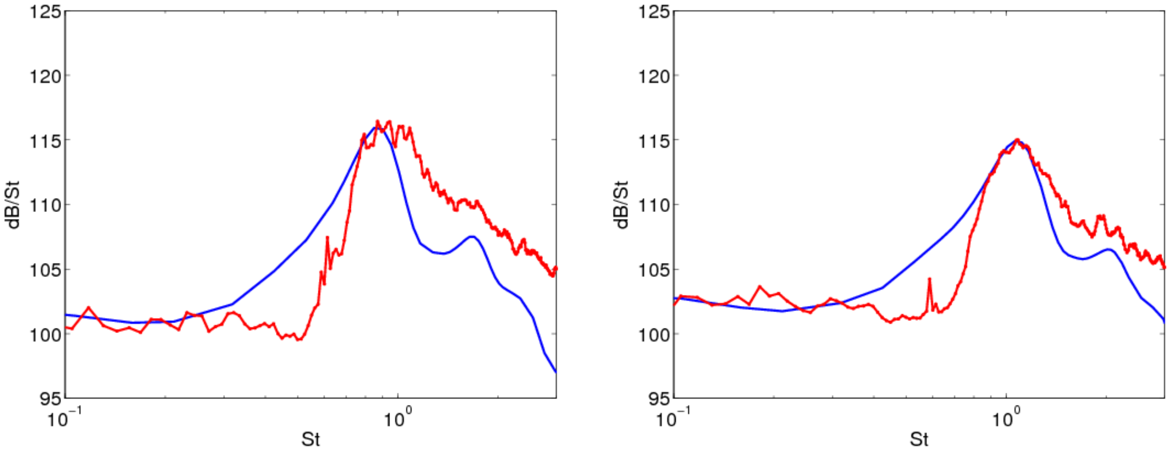

(a) $\Phi = 50°$ (b) $\Phi = 70°$

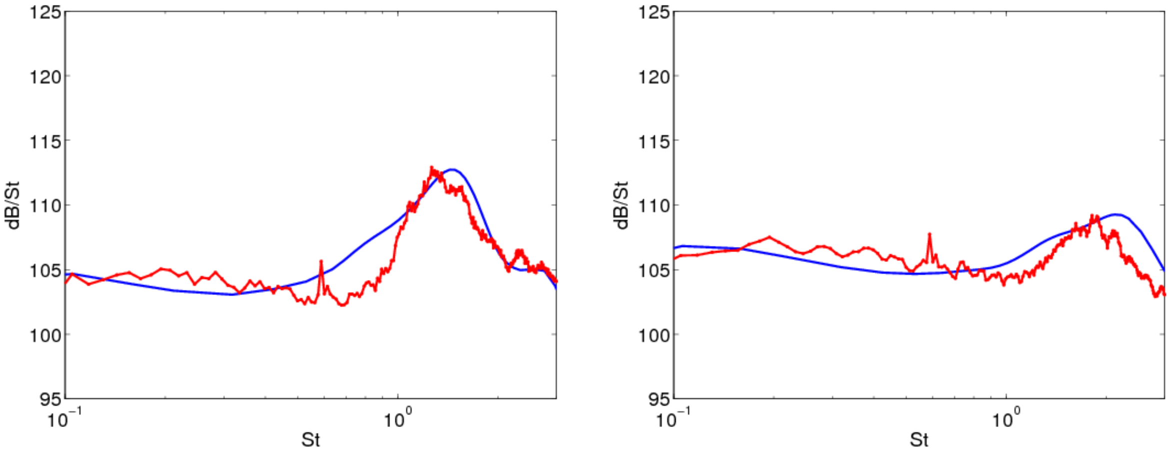

(c) $\Phi = 90°$ (d) $\Phi = 110°$

Figure 4.25: PSDs of a shocked jet, $M_j = 1.15$ for various observer locations. Φ is the inlet angle. —— Measurements by André *et al.*, —— Calculations

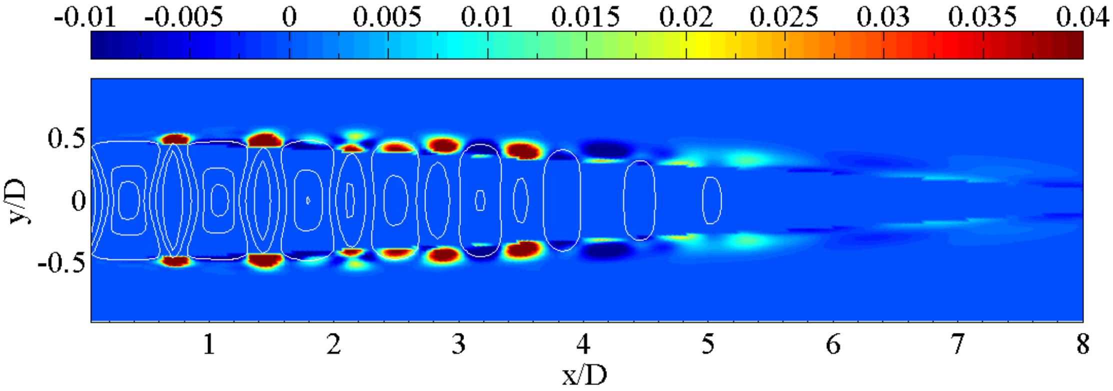

(a) $St = 0.32$, $f = 3000$ Hz

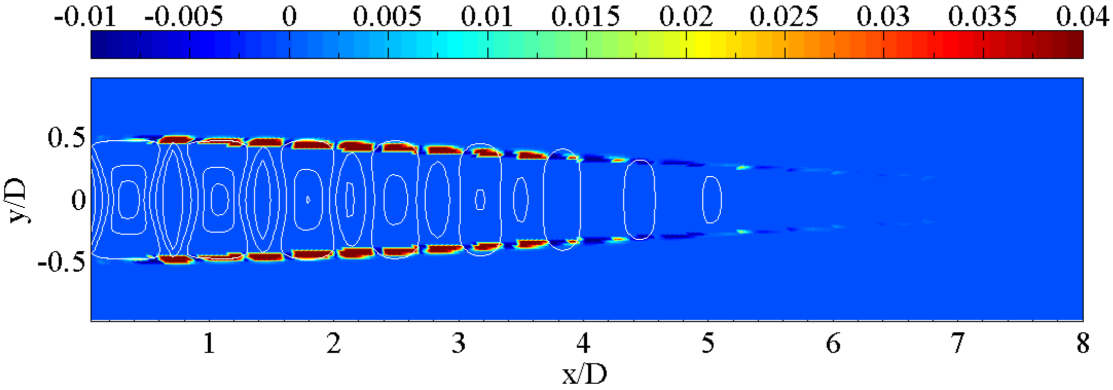

(b) $St = 1.06$, $f = 10000$ Hz

Figure 4.26: Visualization of source terms at $M_j = 1.15$, $\Phi = 70°$ for different frequencies. Pressure iso-lines are shown in white

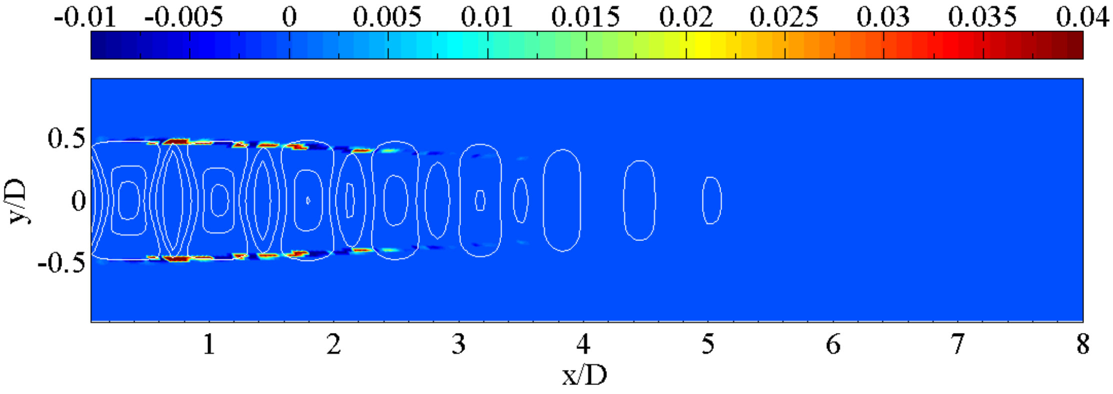

(a) $St = 2.01$, $f = 19000$ Hz

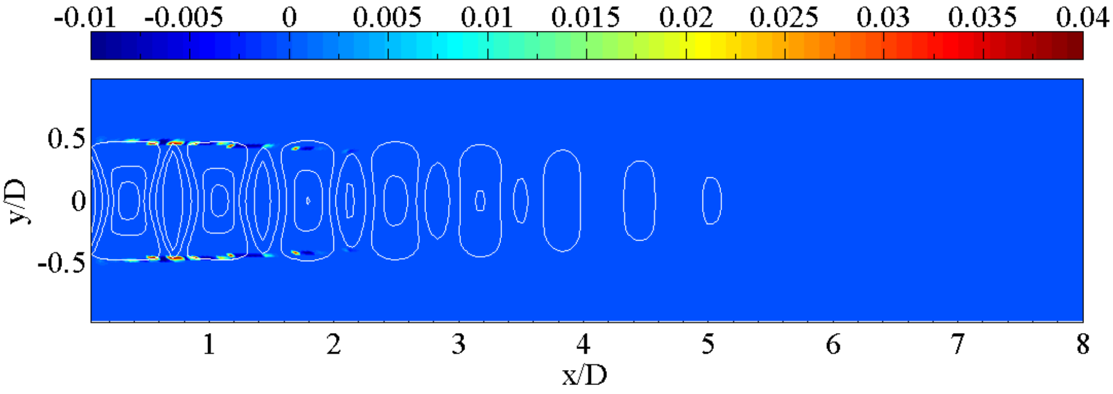

(b) $St = 2.96$, $f = 28000$ Hz

Figure 4.27: Visualization of source terms at $M_j = 1.15$, $\Phi = 70°$ for different frequencies. Pressure iso-lines are shown in white

Case $M_j = 1.35$

The case of a jet at $M_j = 1.35$ is now considered. The PSDs at different angles are presented in Figure 4.28. As compared to the $M_j = 1.15$ case, BBSAN is expected to peak at lower frequencies because of longer shock-cells due to the increased jet Mach number.

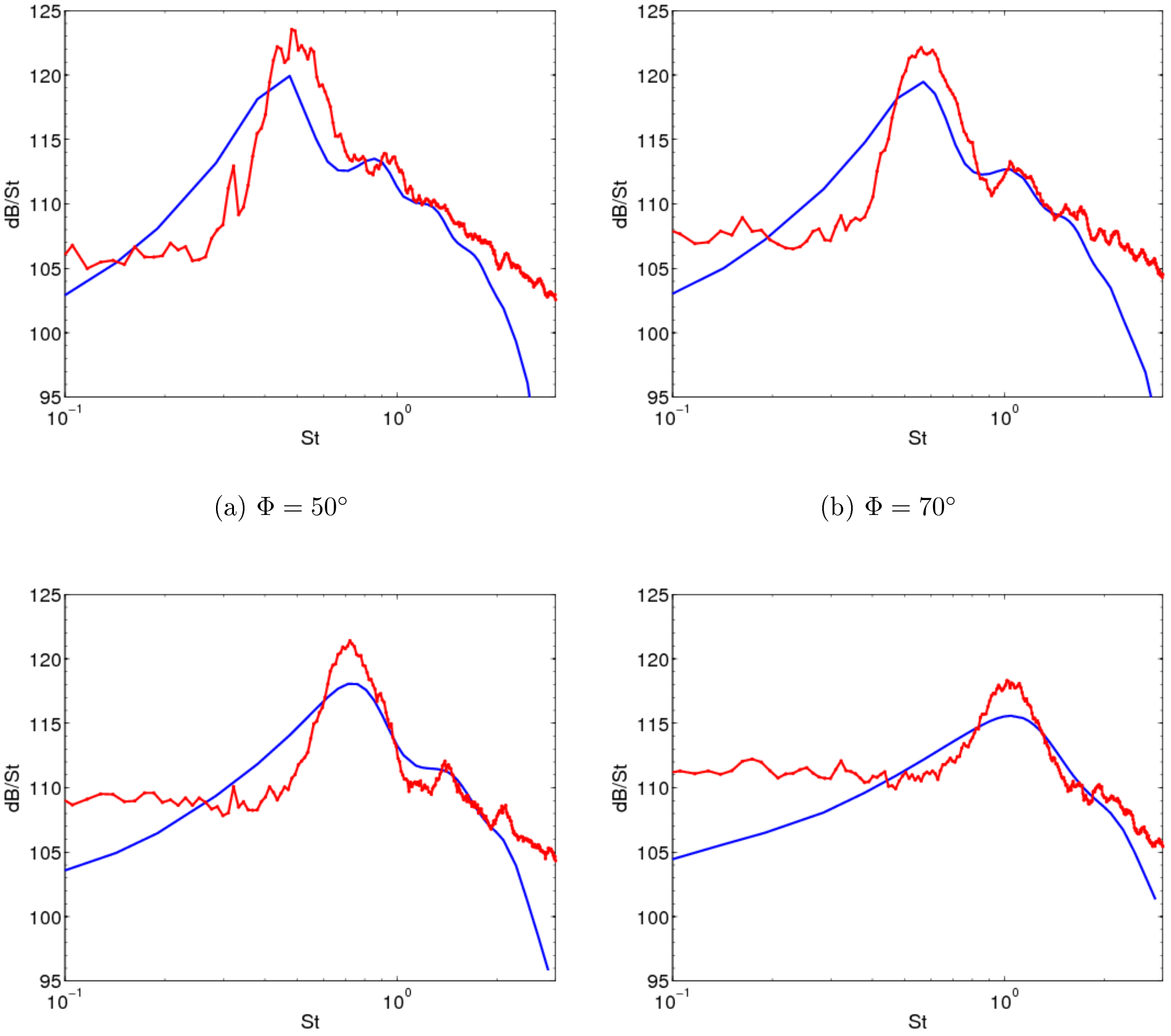

(a) $\Phi = 50°$

(b) $\Phi = 70°$

(c) $\Phi = 90°$

(d) $\Phi = 110°$

Figure 4.28: PSDs of a shocked jet, $M_j = 1.35$ for various observer locations. Φ is the inlet angle. —— Measurements by André *et al.*, —— Calculations

The general shape of the spectrum agrees reasonably well with measurements. The model correctly captures the change in peak frequency with respect to M_j: for $\Phi = 70°$, the peak frequency decreases from $St = 1.0$ to $St = 0.7$ both in calculations and measurements, see Figures 4.4.2 and 4.4.2. Multiple BBSAN humps are also visible in the measurements at this M_j. They are correctly predicted by the model as well, though their amplitude decays a bit too fast.

Source terms are shown in Figures 4.29 and 4.30, for $\Phi = 70°$. There are two major

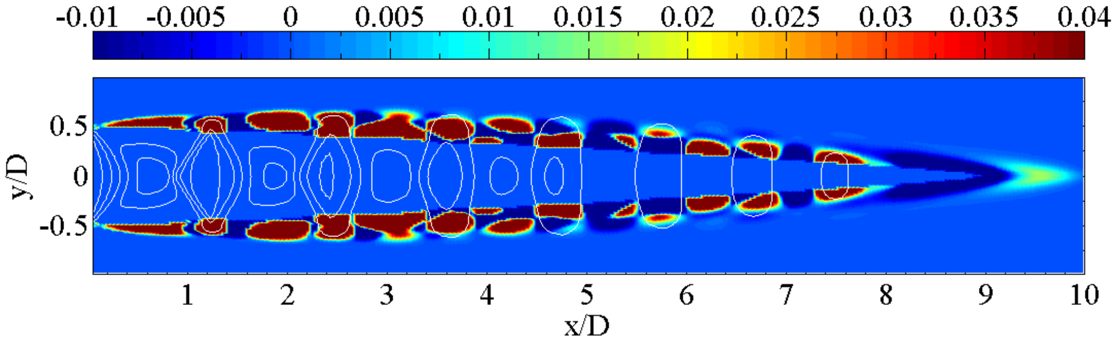

(a) $St = 0.28$, $f = 3000$ Hz

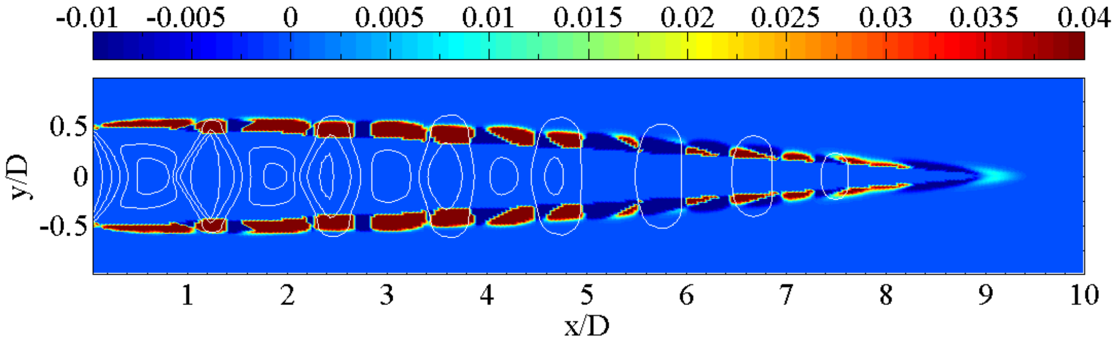

(b) $St = 0.56$, $f = 6000$ Hz

Figure 4.29: Visualization of source terms at $M_j = 1.35$, $\Phi = 70°$ for different frequencies. Pressure iso-lines are shown in white

differences compared to the case $M_j = 1.15$. First, BBSAN sources are stronger in the current case. This is clearly seen in those Figures and also on the PSDs. At $M_j = 1.15$, the maximum SPL was about 115 dB, where it is approximately 120 dB at $M_j = 1.35$. This of course comes from stronger acoustic sources. The second difference is the increased extent of the source domain. This is because shocks are stronger at $M_j = 1.35$, so that it takes more distance downstream for the shock pattern to be destroyed.

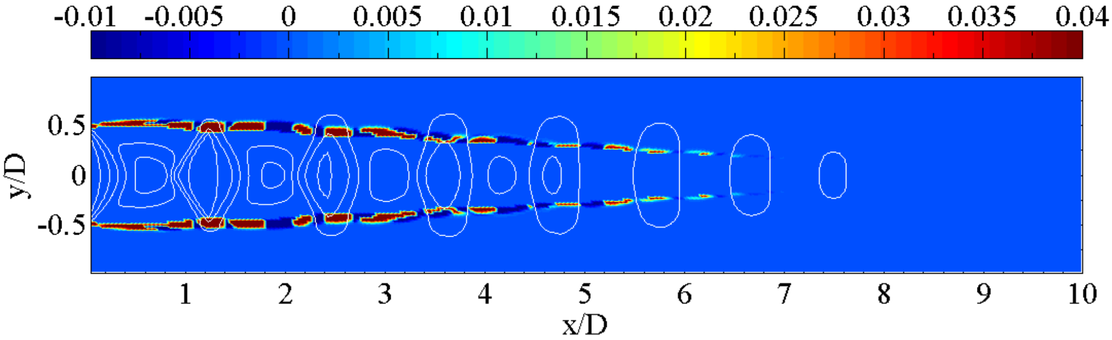

(a) $St = 1.03$, $f = 11000$ Hz

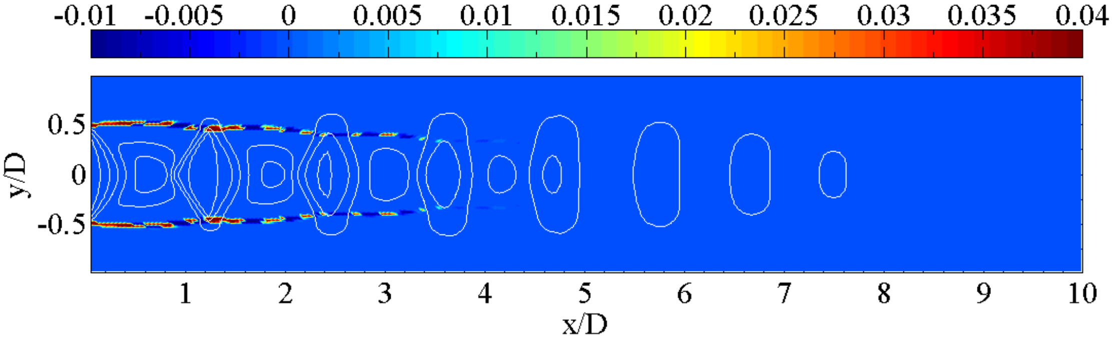

(b) $St = 2.05$, $f = 22000$ Hz

Figure 4.30: Visualization of source terms at $M_j = 1.35$, $\Phi = 70°$ for different frequencies. Pressure iso-lines are shown in white

4.5 Conclusion

In this chapter, the statistical model has been applied to static jets. Two operating conditions have been tested, for various angles. PSDs have been compared to measurements and showed favorable agreement. The visualization of source terms lead to the conclusion that M_j influences not only the aerodynamics of the jet, but also the intrinsic characteristics of the acoustic sources.

The model now needs to be extended, to be able to include flight conditions. This is the purpose of the next chapter.

Chapter 5

Inclusion of refraction effects

5.1 Introduction

So far, the sound produced by BBSAN sources has been propagated using the free-space Green's function. This means that any convection or refraction effect on acoustics has been ignored for the propagation process. Good results can only be expected for single stream jets in static conditions.

5.1.1 Dual stream configurations

Industrial configurations are usually dual stream and contain two mixing layers, and thus two types of BBSAN sources as noticed by Tam [89, 90]. In Figures 5.1 and 5.2, such a configuration is presented. The primary stream is subsonic whereas the secondary stream is supersonic and shocked. There are BBSAN sources in the mixing layer separating the primary and secondary flows, called PS sources. The mixing layer between the secondary stream and the external stream also contains BBSAN sources, called SE sources. The white paths indicate the propagation of an acoustic wave created by both types of sources. On the left-hand side, an SE source is presented. The propagation is slightly modified by the shear layer. On the right-hand side, a PS source radiates through the secondary stream into the ambient medium. Refraction effects are very strong and it is thus necessary to take them into account.

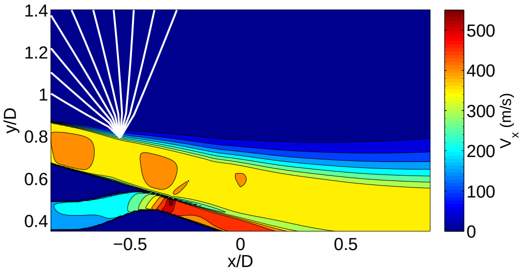

Figure 5.1: Radiation of a SE source

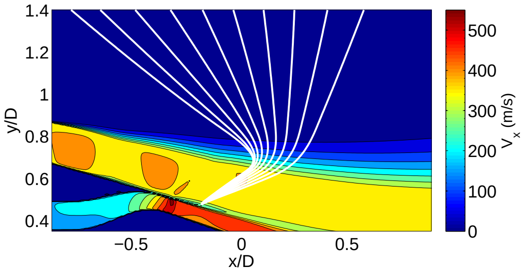

Figure 5.2: Radiation of a PS source

5.1.2 Propagation in a moving medium

The origin of refraction can be easily understood when considering a point source radiating through a jet, as shown in Figure 5.3. There are strong radial velocity gradients in the jet: velocity decreases from the jet centerline to the ambient medium. Consider the wave front AB produced by the source in the mixing layer. Because of the velocity gradients, point B will travel faster than point A. Moving farther downstream, this results in a bent wave front A'B', this phenomenon is called refraction. For a given acoustic source, this means that the initial directivity of the source is modified by the mean flow velocity gradients: refraction induces a quiet region around the jet axis, commonly referred to as a cone of silence or a shadow zone, and was first observed experimentally by Atvars *et al.* [8].

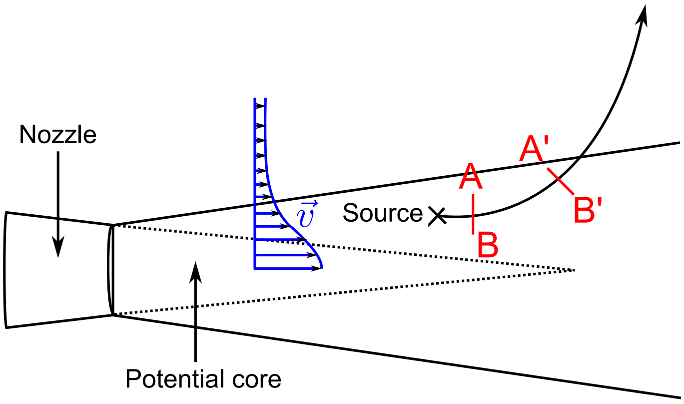

Figure 5.3: Refraction of a ray of sound emitted by a localized source in a jet, from Tam and Auriault[83]

5.1.3 Proposed approach

The acoustic model of this work relies on the resolution of the LEE with a vector Green's function. This function should be tailored to the problem to account for refraction and convection. There are several ways to do so. Miller and Morris [53] used a locally parallel approximation of the mean flow to find the adjoint Green's function of the LEE, as proposed by Tam and Auriault [83].

Here, it is shown that with reasonable approximation, the LEE may be recast into Lilley's equation, that is a scalar wave equation. The corresponding scalar Green's function g_L, including refraction and convection effects, is found thanks to geometric acoustics. g_L is finally related to the vector Green's function of the LEE.

This chapter is organized as follows: first the LEE are recast into Lilley's equation. Second, the computation of a scalar Green's function g_L using ray-tracing is detailed. Third, g_L is related to the vector Green's function of the LEE.

5.2 From the LEE to Lilley's equation

5.2.1 Lilley's equation

For a homogeneous quiescent medium, recasting the LEE into a single wave equation is straightforward, as shown before. In the case of an inhomogeneous moving fluid, some assumptions are necessary to achieve the same result. In what follows, it is assumed that the mean flow is uniformly sheared and parallel to the jet axis, so that

$$\overline{\boldsymbol{v}} = (\overline{v}_1(x_2, x_3), 0, 0) \tag{5.1}$$

As shown by Lilley [45], the LEE can be recast to form a third-order wave equation. The interpretation of all the source terms on the right-hand side of this equation is however tricky [22]. It is possible to linearize this equation about the mean state, so that Lilley's equation reduces to[96, 9]

$$\mathcal{L}p' = \frac{D}{Dt}\left(\frac{D^2}{Dt^2} - \nabla\cdot\overline{c}^2\nabla\right)p' + 2\overline{c}^2\nabla\overline{v_1}\cdot\nabla\frac{\partial}{\partial x_1}p' = \overline{\rho}\,\overline{c}^2\Gamma \tag{5.2}$$

where the source term Γ is defined by

$$\Gamma \equiv -\frac{D}{Dt}\nabla\cdot\boldsymbol{f} + 2\nabla\overline{v}_1\cdot\frac{\partial}{\partial x_1}\boldsymbol{f} \tag{5.3}$$

or similarly in the frequency domain

$$\Gamma(\boldsymbol{y},\omega) = -\left(-i\omega + \overline{v}_1\frac{\partial}{\partial y_1}\right)\frac{\partial f_i}{\partial y_i} + 2\frac{\partial\overline{v}_1}{\partial y_i}\frac{\partial f_i}{\partial y_1} \tag{5.4}$$

In (5.2) the assumption that $\overline{\rho}\,\overline{c}^2 = \gamma\overline{p}$ has been made. Indeed, the uniform shear flow hypothesis implies that the mean static pressure $\overline{p}$ is constant.

5.2.2 Relation between the scalar and vector Green's functions

The scalar Green's function associated with $\mathcal{L}$, namely g_L, is now related to the vector Green's function of the LEE. The function g_L satisfies

$$\mathcal{L}g_L(\boldsymbol{x},\boldsymbol{y},\omega) = \delta(\boldsymbol{x}-\boldsymbol{y}) \tag{5.5}$$

so that the solution to (5.2) is

$$\begin{aligned}
p'(\boldsymbol{x},\omega) &= \overline{\rho}\,\overline{c}^2\int_{\boldsymbol{y}} g_L(\boldsymbol{x},\boldsymbol{y},\omega)\Gamma(\boldsymbol{y},\omega)d\boldsymbol{y} \\
p'(\boldsymbol{x},\omega) &= -\overline{\rho}\,\overline{c}^2\int_{\boldsymbol{y}} g_L(\boldsymbol{x},\boldsymbol{y},\omega)\left[\left(-i\omega + \overline{v}_1\frac{\partial}{\partial y_1}\right)\frac{\partial f_i}{\partial y_i} - 2\frac{\partial\overline{v}_i}{\partial y_i}\frac{\partial f_i}{\partial y_1}\right]d\boldsymbol{y}
\end{aligned} \tag{5.6}$$

Expanding the summation over index i yields,

$$\begin{aligned}
p'(\boldsymbol{x},\omega) = -\overline{\rho}\,\overline{c}^2\int_{\boldsymbol{y}} g_L(\boldsymbol{x},\boldsymbol{y},\omega)\Bigg[&\underbrace{\left(-i\omega + \overline{v}_1\frac{\partial}{\partial y_1}\right)\frac{\partial f_1}{\partial y_1}}_{A} + \underbrace{\left(-i\omega + \overline{v}_1\frac{\partial}{\partial y_1}\right)\frac{\partial f_2}{\partial y_2}}_{B} \\
&+ \underbrace{\left(-i\omega + \overline{v}_1\frac{\partial}{\partial y_1}\right)\frac{\partial f_3}{\partial y_3}}_{C} - 2\underbrace{\frac{\partial\overline{v}_1}{\partial y_1}\frac{\partial f_1}{\partial y_1}}_{=0} - 2\underbrace{\frac{\partial\overline{v}_1}{\partial y_2}\frac{\partial f_2}{\partial y_1}}_{D} - 2\underbrace{\frac{\partial\overline{v}_1}{\partial y_3}\frac{\partial f_3}{\partial y_1}}_{E}\Bigg]d\boldsymbol{y}
\end{aligned} \tag{5.7}$$

The detailed calculation of the terms A, B, C, D, E is given in Appendix B.3. Injecting these expressions into $p'(\boldsymbol{x},\omega)$ gives,

$$\begin{aligned}
p'(\boldsymbol{x},\omega) = \overline{\rho}\,\overline{c}^2 \int_{\boldsymbol{y}} \Bigg\{ &- \left(i\omega \frac{\partial g_L}{\partial y_1} + \overline{v}_1 \frac{\partial^2 g_L}{\partial y_1^2} \right) f_1 \\
&- \left(i\omega \frac{\partial g_L}{\partial y_2} + 3 \frac{\partial \overline{v}_1}{\partial y_2} \frac{\partial g_L}{\partial y_1} + \overline{v}_1 \frac{\partial^2 g_L}{\partial y_1 \partial y_2} \right) f_2 \\
&- \left(i\omega \frac{\partial g_L}{\partial y_3} + 3 \frac{\partial \overline{v}_1}{\partial y_3} \frac{\partial g_L}{\partial y_1} + \overline{v}_1 \frac{\partial^2 g_L}{\partial y_1 \partial y_3} \right) f_3 \Bigg\} d\boldsymbol{y}
\end{aligned} \tag{5.8}$$

Direct identification with the general expression,

$$p'(\boldsymbol{x},\omega) = \overline{\rho}\,\overline{c}^2 \iint \Pi_n(\boldsymbol{x},\boldsymbol{y},\omega) f_n(\boldsymbol{y},\omega) d\boldsymbol{y} \tag{5.9}$$

allows the vector Green's function of the LEE Π_n to be related to the scalar Green's function of Lilley's equation g_L through,

$$\begin{aligned}
\Pi_1(\boldsymbol{x},\boldsymbol{y},\omega) &= - \left(i\omega \frac{\partial g_L}{\partial y_1} + \overline{v}_1 \frac{\partial^2 g_L}{\partial y_1^2} \right) \\
\Pi_2(\boldsymbol{x},\boldsymbol{y},\omega) &= - \left(i\omega \frac{\partial g_L}{\partial y_2} + 3 \frac{\partial \overline{v}_1}{\partial y_2} \frac{\partial g_L}{\partial y_1} + \overline{v}_1 \frac{\partial^2 g_L}{\partial y_1 \partial y_2} \right) \\
\Pi_3(\boldsymbol{x},\boldsymbol{y},\omega) &= - \left(i\omega \frac{\partial g_L}{\partial y_3} + 3 \frac{\partial \overline{v}_1}{\partial y_3} \frac{\partial g_L}{\partial y_1} + \overline{v}_1 \frac{\partial^2 g_L}{\partial y_1 \partial y_3} \right)
\end{aligned} \tag{5.10}$$

The calculation of Π_n hence reduces to the computation of g_L and its derivatives.

5.3 Computation of the scalar Green's function g_L with ray-tracing

In this section, it is shown how to compute g_L using geometric acoustics. Durbin formulated a general theory [27, 28] to construct the high frequency Green's function for a source in an arbitrary subsonic flow. A different approach is used here, so that the formulation is not restricted to the subsonic domain, but some assumptions are made about the flow.

The theory of geometric acoustics is first presented for an inhomogeneous medium at rest and then extended to the case of a moving fluid. g_L is then determined from ray theory. Numerical implementation is described and the work is validated with different test cases.

5.3.1 Geometric acoustics for an inhomogeneous medium at rest

The geometric wave theory provides a solution to the LEE in the high frequency limit. The idea is to extend the plane wave concept for homogeneous media at rest, to the case of inhomogeneous moving fluids. The wave fronts are described locally by their tangent planes. λ being the wave length and L the characteristic size of the medium, the quality of the approximation is in proportion to how small is $\varepsilon = \lambda/L$. This technique is described in the work of Hayes [34] and may be used for various applications, including underwater acoustics, atmospheric propagation and aeroacoustics. Examples of applications in aeroacoustics include the refraction of a point source in a jet by Schubert [74] and the study of shielding, scattering and refraction in a shear flow by Candel *et al.* [20, 21] and Candel [18].

The governing equations are now derived for the simple case of a medium at rest, as presented in Rienstra and Hirschberg[72]. The equations will be extended to a moving fluid afterwards. For an inhomogeneous fluid at rest, the Helmholtz equation is,

$$\nabla\cdot\left(\frac{1}{k^2}\nabla p\right)+p=0 \qquad k=k(\varepsilon\boldsymbol{x})=\frac{\omega}{c_0(\varepsilon\boldsymbol{x})} \tag{5.11}$$

where k is the local wavenumber. The geometrical approximation consists in searching for a solution to (5.11) in the form

$$p(\boldsymbol{x})=Ae^{-i\omega\tau/\varepsilon} \tag{5.12}$$

where the amplitude $A=A(\boldsymbol{X},\varepsilon)$ varies slowly with position and $\tau=\tau(\boldsymbol{X},\varepsilon)$ is the phase function. $\boldsymbol{X}=\varepsilon\boldsymbol{x}$ is the slow position variable. The phase of this wave is $\Theta=\omega\tau/\varepsilon$, so that the wave vector $\boldsymbol{k}$ is the phase gradient: $\boldsymbol{k}=\nabla\Theta=\omega/\varepsilon\overline{\nabla}\tau$. The spatial gradient operator with respect to the slowly varying coordinates is now introduced,

$$\overline{\nabla}\triangleq\left(\frac{\partial}{\partial X},\frac{\partial}{\partial Y},\frac{\partial}{\partial Z}\right) \quad \text{and} \quad \nabla=\varepsilon\overline{\nabla} \tag{5.13}$$

Using these notations, the Helmholtz equation becomes,

$$(k^2-\omega^2|\overline{\nabla}\tau|^2)A-i\varepsilon\omega\frac{k^2}{A}\overline{\nabla}\cdot\left(\frac{A^2\overline{\nabla}\tau}{k^2}\right)+\varepsilon^2k^2\overline{\nabla}\cdot\left(\frac{1}{k^2}\overline{\nabla}A\right)=0 \tag{5.14}$$

Then, an asymptotic expansion of the amplitude and phase is performed,

$$\begin{aligned} A(\boldsymbol{X},\varepsilon)&=A_0(\boldsymbol{X})+\varepsilon A_1(\boldsymbol{X})+O(\varepsilon^2)\\ \tau(\boldsymbol{X},\varepsilon)&=\tau_0(\boldsymbol{X})+O(\varepsilon^2)\end{aligned} \tag{5.15}$$

Collecting identical powers in (5.14) gives the well-known equations

$$|\overline{\nabla}\tau_0|^2=\frac{1}{c_0^2} \tag{5.16}$$

$$\overline{\nabla}\cdot(c_0^2A_0^2\overline{\nabla}\tau_0)=0 \tag{5.17}$$

Equation (5.16) is the *eikonal equation* (from the German word *eikonal*, which means *image* in Greek). This non-linear partial differential equation is not restricted to the present case: it is encountered in fields such as optics or electromagnetism involving wave propagation, when the wave operator is expanded asymptotically. Physically, the *eikonal equation* governs the wave fronts and the ray trajectories, that is the propagation of acoustic energy. Such a hyperbolic differential equation is solved conveniently with the method of characteristics. A characteristic is basically a line along which the information from the domain boundary is transfered to the point of observation.

Applying the method of characteristics to the *eikonal equation* results in the linear differential system,

$$\begin{aligned} \frac{d\boldsymbol{X}}{dt} &= \varepsilon c_0 \frac{\overline{\nabla}\tau_0}{|\overline{\nabla}\tau_0|} = \varepsilon c_0 \frac{\boldsymbol{k}}{|\boldsymbol{k}|} \\ \frac{d}{dt}\overline{\nabla}\tau_0 &= -\varepsilon \frac{\overline{\nabla}c_0}{c_0} \end{aligned} \tag{5.18}$$

Reverting to the original notations,

$$\begin{aligned} \frac{d\boldsymbol{x}}{dt} &= c_0 \frac{\boldsymbol{k}}{|\boldsymbol{k}|} \\ \frac{d\boldsymbol{k}}{dt} &= -k\nabla c_0 \end{aligned} \tag{5.19}$$

The first equation means that the wave front is convected at the local speed c_0, whereas the second equation means that the wave front is refracted (i.e. its direction of propagation changes) by gradients in the speed of sound. In a word, the *eikonal equation* (non-linear, first-order partial differential equation), has been replaced by a set of linear first-order coupled differential equations. These equations are the *ray-tracing equations.*

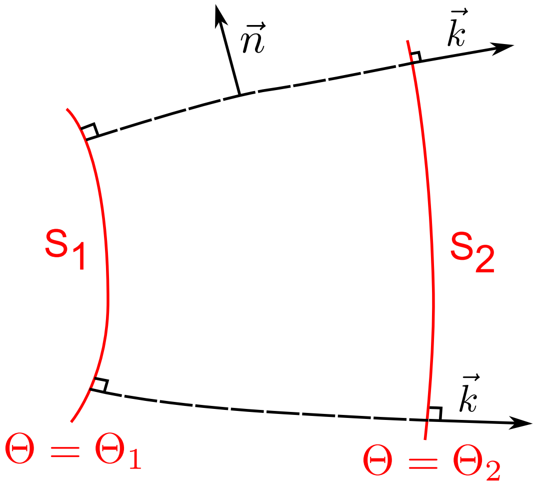

Figure 5.4: A ray tube connecting two equiphase surfaces in a quiescent medium

Once the *eikonal equation* is solved, the amplitude of the acoustic wave may be tracked along the ray paths using the transport equation (5.17) and the ray tube concept. Consider two surfaces S_1 and S_2 of constant phase, respectively $\Theta = \Theta_1$ and $\Theta = \Theta_2$ as illustrated in Figure 5.4. Connect these two surfaces with the corresponding rays (following the ray paths) to create a volume: this volume is called an elementary ray tube. The transport equation can be easily evaluated over the central surface of such a ray tube, using Ostrogradsky's theorem and two properties of the tube: first, on S_1 and S_2, $\overline{\nabla}\tau_0 = \boldsymbol{n}/c_0^2$ where $\boldsymbol{n}$ is the outward normal to the surface. Second, on the sides of the tube, $\overline{\nabla}\tau_0 \cdot \boldsymbol{n} = 0$. Consequently, the integral form of the transport equation states that,

$$\int_{\text{tube}} \overline{\nabla} \cdot (c_0^2 A_0^2 \overline{\nabla}\tau_0) d\boldsymbol{x} = \int_{S_2} c_0 A_0^2 dS - \int_{S_1} c_0 A_0^2 dS = 0 \tag{5.20}$$

Hence, the evolution of the acoustic amplitude along a ray is given by

$$A_0^2(\boldsymbol{X})c_0(\boldsymbol{X})S(\boldsymbol{X}) = \text{cst} \tag{5.21}$$

where $S(\boldsymbol{X})$ is the section of the corresponding ray tube and the constant is the energy injected by the acoustic source into the tube. It follows that when the tube section increases, the wave amplitude decreases and conversely.

5.3.2 Geometrical acoustics for a moving fluid

Since the theory is to be applied to jet flows, it needs to be extended to the case of moving fluids. First, the calculation of the ray paths is described, then geodesic elements are introduced to assess the amplitude of the wave along the ray tube, finally numerical implementation is presented.

Ray paths

So far, the medium has been assumed to be at rest. When the fluid is moving, additional terms need to be included into the previous equations, so that (5.19) becomes,

$$\begin{cases} \dfrac{dx_i}{dt} = c\dfrac{k_i}{k} + \underbrace{v_{0i}}_{(a)} \equiv g_i(\boldsymbol{x}, \boldsymbol{k}) \\ \dfrac{dk_i}{dt} = -k\dfrac{\partial c}{\partial x_i} - \underbrace{k_j \dfrac{\partial v_{0j}}{\partial x_i}}_{(b)} \equiv h_i(\boldsymbol{x}, \boldsymbol{k}) \end{cases} \tag{5.22}$$

The term (a) means that the wave fronts are convected by the local flow velocity. As a result, the ray paths are not perpendicular to the wave fronts anymore. The term (b) conveys the refraction of the waves by the gradients in the flow velocity. The group velocity $v_{g_i} = ck_i/k + v_{0i}$ represents the speed at which the acoustic energy travels,

$$\boldsymbol{v}_g = c\boldsymbol{\nu} + \boldsymbol{v}_0 \quad \boldsymbol{\nu} = \boldsymbol{k}/k \tag{5.23}$$

Figures 5.5-5.6 illustrate the differences between a quiescent and a moving medium, respectively on the left and right-hand side. In a quiescent medium, the rays are perpendicular to the wave fronts and travel at $\boldsymbol{v}_g = c\boldsymbol{\nu}$. In a moving medium, the flow bends the ray trajectory and information travels at $\boldsymbol{v}_g = c\boldsymbol{\nu} + \boldsymbol{v}_0$. Physically, the rays are tangent to the group velocity vector. (5.22) is closed by specifying the source location and the initial shooting angles (θ_0, α_0) so that the ray paths may be found. The coordinate system is described in Figure 5.7.

Acoustic amplitude

Equation (5.21) relates the evolution of the wave amplitude along the rays to the ray tube section for a quiescent medium. For a moving fluid, a similar relation may be established. It is convenient to use the acoustic energy density E $(J.m^{-3})$, related to the rms value of the acoustic pressure fluctuations by,

$$\overline{p'^2} = \frac{\rho c^2 E}{1 + \boldsymbol{M} \cdot \boldsymbol{\nu}} \tag{5.24}$$

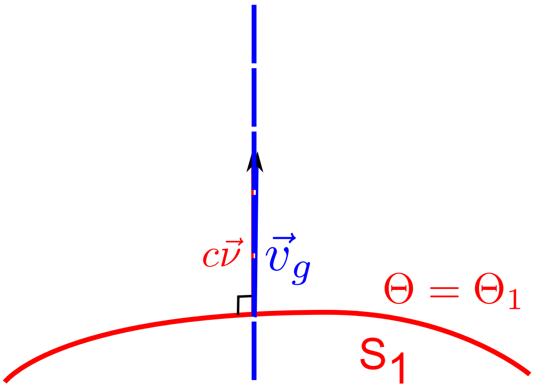

Figure 5.5: Visualization of the ray path for a quiescent medium. The ray is perpendicular to the wave front

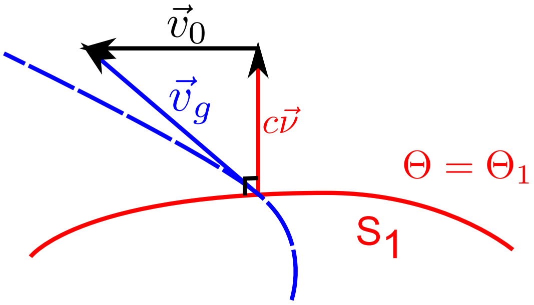

Figure 5.6: Visualization of the ray path for a moving medium. The ray is bent by the flow

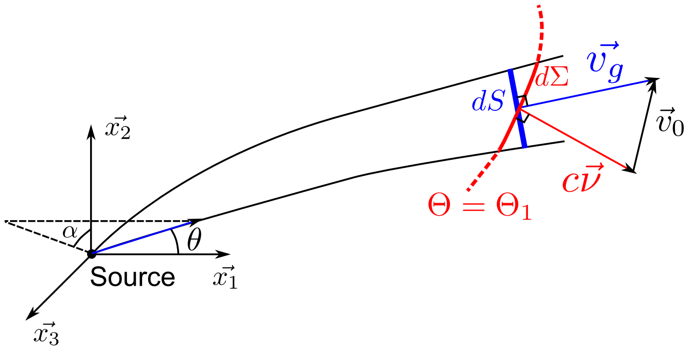

Figure 5.7: Visualization of the cross-section of a ray tube dS, and the intersected wave front section $d\Sigma$

The acoustic energy flowing through a ray tube at the speed $\boldsymbol{v_g}$ is conserved,

$$\int_{\text{tube}} E\boldsymbol{v_g} \cdot \boldsymbol{n} dS = 0 \tag{5.25}$$

In this expression, dS is the cross-section of the ray tube, it is not the surface of the wave front intersected by the ray tube $d\Sigma$. This distinction is illustrated in Figure 5.7. For a given ray tube, the local version of (5.25) is,

$$E v_g dS = K_1 \tag{5.26}$$

where K_1 is the acoustic power injected by the source in the ray tube. Thus, $\overline{p'^2}$ is given as a function of the tube cross-section by

$$\overline{p'^2} = \frac{\rho c^2 K_1}{(1 + \boldsymbol{M} \cdot \boldsymbol{\nu}) v_g dS} \tag{5.27}$$

The group velocity $\boldsymbol{v_g}$ has been determined previously when finding the ray paths. The surface element dS is the only quantity left to evaluate. At least two techniques may be used. The most intuitive one consists in shooting multiple rays from the source to create a tube, and to compute the evolution of dS along the tube. This technique is not very efficient and raises issues, the main one being how many rays to shoot to create a proper ray tube to evaluate dS accurately. Another technique has been used, introduced by Candel [19] in aeroacoustics and summarisd here. First, four geodesic elements are defined:

$$\begin{cases} \boldsymbol{R}^\theta = \left(\dfrac{\partial \boldsymbol{x}}{\partial \theta_0}\right)_{t,\alpha_0} & \boldsymbol{R}^\alpha = \left(\dfrac{\partial \boldsymbol{x}}{\partial \alpha_0}\right)_{t,\theta_0} \\ \boldsymbol{Q}^\theta = \left(\dfrac{\partial \boldsymbol{k}}{\partial \theta_0}\right)_{t,\alpha_0} & \boldsymbol{Q}^\alpha = \left(\dfrac{\partial \boldsymbol{k}}{\partial \alpha_0}\right)_{t,\theta_0} \end{cases} \tag{5.28}$$

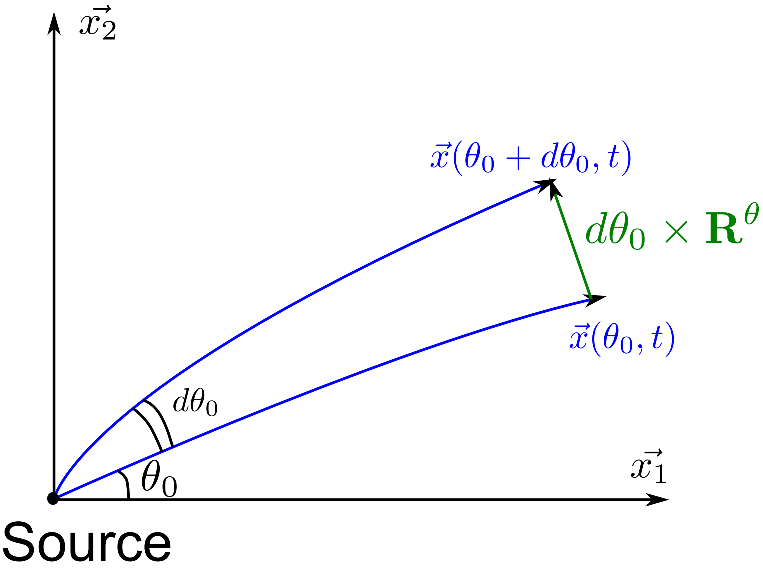

Figure 5.8: Visualization of the geodesic element $\boldsymbol{R}^\theta$

$\boldsymbol{R^\theta}$ quantifies the change in the ray path when slightly shifting the shooting angle θ_0, this is shown in Figure 5.8. A similar meaning holds for $\boldsymbol{R}^\alpha, \boldsymbol{Q}^\theta, \boldsymbol{Q}^\alpha$. By applying the chain rule of differentiation, the evolution of the geodesic elements along the rays is governed by

$$\begin{cases} \dfrac{d\boldsymbol{R}}{dt} = \dfrac{\partial \boldsymbol{g}}{\partial \boldsymbol{x}} \cdot \boldsymbol{R} + \dfrac{\partial \boldsymbol{g}}{\partial \boldsymbol{k}} \cdot \boldsymbol{Q} \\ \dfrac{d\boldsymbol{Q}}{dt} = \dfrac{\partial \boldsymbol{h}}{\partial \boldsymbol{x}} \cdot \boldsymbol{R} + \dfrac{\partial \boldsymbol{h}}{\partial \boldsymbol{k}} \cdot \boldsymbol{Q} \end{cases} \tag{5.29}$$

The explicit expressions of the Jacobian matrices $\partial \boldsymbol{g}/\partial \boldsymbol{x}, \partial \boldsymbol{g}/\partial \boldsymbol{k}, \partial \boldsymbol{f}/\partial \boldsymbol{x}, \partial \boldsymbol{f}/\partial \boldsymbol{k}$ are given in Appendix C.1 and the full expression of (5.29) is detailed in Appendix C.2. The initial conditions for the geodesic elements are given in Appendix C.3. After solving systems (5.22) and (5.29), the cross-section of the tube is recovered by the relation,

$$dS = |(d\theta_0 \boldsymbol{R}^\theta) \times (d\alpha_0 \boldsymbol{R}^\alpha) \cos(\boldsymbol{k}, \boldsymbol{v_g})| \tag{5.30}$$

and $\overline{p'^2}$ is then fully known.

Numerical calculation

Both ray paths and geodesic elements are solved using a 4th-order Runge-Kutta method. This method is easy to implement, fast and robust. The outline of the method is the following: given an initial value problem

$$\frac{dx}{dt} = f(x, t), \quad x(t_0) = x_0 \tag{5.31}$$

the solution is sampled at times $t_n = n\Delta t,\ n \in \mathbb{N}$, the samples are $x_n = x(n\Delta t)$. The Runge-Kutta method is a time-marching method, that relates x_n to x_{n+1} by,

$$x_{n+1} = x_n + \frac{1}{6}(k_1 + 2k_2 + 2k_3 + k_4) \tag{5.32}$$

where

$$\begin{aligned} k_1 &= \Delta t f(x_n, t_n) \\ k_2 &= \Delta t f(x_n + \frac{1}{2}k_1, t_n + \frac{1}{2}\Delta t) \\ k_3 &= \Delta t f(x_n + \frac{1}{2}k_2, t_n + \frac{1}{2}\Delta t) \\ k_4 &= \Delta t f(x_n + k_3, t_n + \Delta t) \end{aligned} \tag{5.33}$$

At each time step, dx/dt is evaluated at four points: the initial point, two mid-step points and the final point. x_{n+1} is then computed from these derivatives.

For practical applications, the ray paths are computed first because they depend neither on the geodesic elements nor on the considered frequency. The geodesic elements are computed afterwards.

5.3.3 Determination of the scalar Green's function from the ray-tracing solution

The ray-tracing method solves the propagation problem for a point source located at $\boldsymbol{y}_s$ by providing the RMS value of the pressure perturbation p' along acoustic rays. It is possible to relate p' to g_L by defining a consistent source term and after expressing p' as a function of $\overline{p'^2}$.

Acoustic pressure along the rays

In the geometrical acoustics approximation, the acoustic pressure is expressed as

$$p'(\boldsymbol{x},\omega) = \tilde{p}(\boldsymbol{x})e^{-i\boldsymbol{k}\cdot(\boldsymbol{x}-\boldsymbol{y_s})} \tag{5.34}$$

where the amplitude $\tilde{p}(\boldsymbol{x})$ is related to the RMS value of p' by

$$\overline{p'^2} = \frac{1}{2}|\tilde{p}|^2 \tag{5.35}$$

The complex amplitude $\tilde{p}$ is,

$$\tilde{p} = \sqrt{2}\sqrt{\overline{p'^2}}e^{i\phi} \tag{5.36}$$

The value $\phi = \pi/2$ is chosen here for comparison with analytical results. Thus, the acoustic pressure along the rays is simply,

$$p'(\boldsymbol{x},\omega) = i\sqrt{2\overline{p'^2}}e^{-i\boldsymbol{k}\cdot(\boldsymbol{x}-\boldsymbol{y_s})} \tag{5.37}$$

Or more explicitly,

$$p'(\boldsymbol{x},\omega) = i\sqrt{\frac{2\rho c^2 K_1}{(1+\boldsymbol{M}\cdot\boldsymbol{\nu})v_g dS}}e^{-i\boldsymbol{k}\cdot(\boldsymbol{x}-\boldsymbol{y_s})} \tag{5.38}$$

From p' to g_L

The acoustic pressure p' is straightforwardly related to g_L when using a point source in Lilley's equation, i.e. $\Gamma(\boldsymbol{y}) = \delta(\boldsymbol{y}-\boldsymbol{y_s})$. Then, the pressure perturbation is

$$\begin{aligned} p'(\boldsymbol{x},\omega) &= \overline{\rho}\,\overline{c}^2\int_{\boldsymbol{y}} g_L(\boldsymbol{x},\boldsymbol{y},\omega)\delta(\boldsymbol{y}-\boldsymbol{y_s})d\boldsymbol{y} \\ p'(\boldsymbol{x},\omega) &= \overline{\rho}\,\overline{c}^2 g_L(\boldsymbol{x},\boldsymbol{y}_s,\omega) \end{aligned} \tag{5.39}$$

so that g_L is given by,

$$g_L(\boldsymbol{x},\boldsymbol{y},\omega) = \frac{1}{\overline{\rho}\,\overline{c}^2}i\sqrt{\frac{2\rho c^2 K_1}{(1+\boldsymbol{M}\cdot\boldsymbol{\nu})v_g dS}}e^{-i\boldsymbol{k}\cdot(\boldsymbol{x}-\boldsymbol{y_s})} \tag{5.40}$$

All the quantities in the previous expression are known except K_1, which will now be determined.

Acoustic power injected in the ray tube

The acoustic power injected in the ray tube K_1 directly depends on the source term in Lilley's equation. The first step is to compute the total acoustic power W_a created by Γ, and then K_1 is expressed as a fraction of W_a.

To estimate W_a, the acoustic field due to $\Gamma(\boldsymbol{y}) = \delta(\boldsymbol{y}-\boldsymbol{y}_s)$ should be known. As will be shown in the next section, rays will be shot from a medium at rest, so that it is reasonable to assume that there is no flow close to the source, hence Helmholtz's equation is verified by p', that is,

$$(\Delta + k^2)p' = \rho_\infty \nabla\cdot\boldsymbol{f} \tag{5.41}$$

From Lilley's equation, $\Gamma = i\omega\nabla\cdot\boldsymbol{f}$ so that in Helmholtz equation $\nabla\cdot\boldsymbol{f} = \frac{1}{i\omega}\delta(\boldsymbol{y}-\boldsymbol{y_s})$ and then,

$$(\Delta + k^2)p' = \frac{\rho_\infty}{i\omega}\delta(\boldsymbol{y}-\boldsymbol{y_s}) \tag{5.42}$$

The Green's function satisfies $(\Delta + k^2)g_0 = \delta(\boldsymbol{x}-\boldsymbol{y})$ and is given by $g_0(\boldsymbol{x},\boldsymbol{y},\omega) = e^{i\boldsymbol{k}\cdot(\boldsymbol{x}-\boldsymbol{y})}/(4\pi||\boldsymbol{x}-\boldsymbol{y}||)$. The pressure field created by Γ without mean flow is,

$$p'(\boldsymbol{x},\omega) = \frac{\rho_\infty}{i\omega}g_0(\boldsymbol{x},\boldsymbol{y},\omega) \tag{5.43}$$

The RMS value is $\overline{p'^2} = \rho_\infty^2/(32\pi^2\omega^2R^2)$ where $R = ||\boldsymbol{x}-\boldsymbol{y}||$. For a plane wave, the norm of the intensity vector is

$$I = \frac{\overline{p'^2}}{\rho_\infty c_\infty} = \frac{\rho_\infty}{32\pi^2\omega^2 c_\infty R^2} \tag{5.44}$$

Then $W_a = 4\pi R^2 I$ so that,

$$W_a = \frac{\rho_\infty}{8\pi\omega^2 c_\infty} \tag{5.45}$$

Finally, the acoustic power injected in a ray tube with solid angle $d\Omega = \sin\theta_0 d\theta_0 d\alpha_0$ is,

$$K_1 = \frac{d\Omega}{4\pi}W_a \tag{5.46}$$

All the quantities required to compute g_L have been determined. In the case of a shocked jet, the acoustic sources are spatially extended. For a given observer location, applying the method as is would require to shoot from each source at the observer. Since it is not possible to determine the proper shooting angle before shooting (the rays are bent by the flow), this means shooting multiple rays for each source, which is very costly and inefficient. Consequently, an adjoint approach is used.

5.3.4 The adjoint approach

The adjoint approach provides an efficient way to compute the scalar Green's function. Basically, it consists in inverting the source and observer locations when computing g_L. This is illustrated in Figure 5.9. The adjoint Green's function associated with g_L is denoted g_L^a. As shown by Tam and Auriault [83], the direct and adjoint Green's functions satisfy,

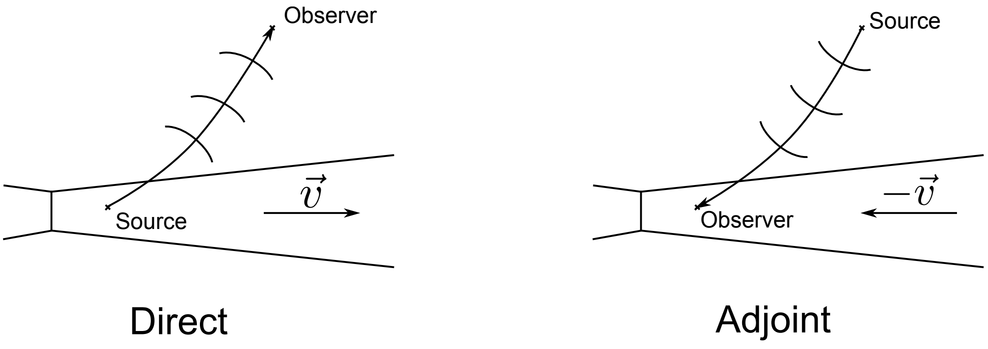

Figure 5.9: Illustration of the direct and adjoint radiation problems

$$g_L(\boldsymbol{x},\boldsymbol{y},\omega) = g_L^a(\boldsymbol{x},\boldsymbol{y},\omega) \tag{5.47}$$

To solve the adjoint problem, one inverts the source and observer locations as well as the flow field, that is $\boldsymbol{v}$ becomes $-\boldsymbol{v}$. The advantage of the adjoint is the following: the rays are shot from a single location at the sources. There is no need to shoot a set of rays for each source. This technique is used here, viz. $g_L(\boldsymbol{x}, \boldsymbol{y}, \omega)$ is replaced by $g_L^a(\boldsymbol{y}, \boldsymbol{x}, \omega)$ in the calculation.

5.3.5 Phase-amplitude decomposition of g_L

Ray paths are independent of frequency. Nevertheless, the wave amplitude along the rays does depend on frequency, and so does g_L, as seen in (5.40). If the ray-tracing program only outputs the result of (5.40), this means that the ray-tracing algorithm has to be run for each frequency, which is very inefficient! This issue is circumvented by writing g_L in terms of amplitude and phase, that is,

$$g_L(\boldsymbol{x}, \boldsymbol{y}, \omega) = A(\boldsymbol{x}, \boldsymbol{y}) e^{-i\boldsymbol{k}\cdot(\boldsymbol{x}-\boldsymbol{y})} \tag{5.48}$$

The ray-tracing algorithm computes $g_L(\boldsymbol{x}, \boldsymbol{y}, \omega_0)$ for an arbitrary fixed frequency ω_0. The amplitude $A(\boldsymbol{x}, \boldsymbol{y})$ is stored, as well as the unitary wave vector $\boldsymbol{\nu} = \boldsymbol{k}/k$. Then, the Green's function at any frequency ω can be recovered easily: the amplitude is known (it does not depend on angular frequency), and the phase factor is computed after determining $\boldsymbol{k}$ with the dispersion relation,

$$k = \frac{\omega}{c + \boldsymbol{v}\cdot\boldsymbol{\nu}} \tag{5.49}$$

5.3.6 Test cases

Several test cases are now shown to illustrate the method. The first case simply consists in shooting in a quiescent uniform medium. In the second case, a uniform mean flow is studied. Finally, g_L is computed on a supersonic jet flow.

Quiescent uniform medium

For this first case, the medium is at rest and uniform. By combining Equations (5.39) and (5.43), g_L is related to the free field Green's function of Helmholtz's equation by,

$$g_L(\boldsymbol{x}, \boldsymbol{y}, \omega) = \frac{1}{i\omega c^2} g_0(\boldsymbol{x}, \boldsymbol{y}, \omega) \quad \text{and} \quad g_0(\boldsymbol{x}, \boldsymbol{y}, \omega) = \frac{e^{ikR}}{4\pi R} \tag{5.50}$$

where $R = ||\boldsymbol{x} - \boldsymbol{y}||$.

This analytical expression is compared to the ray-tracing result. g_L is computed on the domain defined by $0 \leq x/D \leq 5$ and $0 \leq y/D \leq 2.5$, where $D = 0.038$ m. The source is located at $x/D = 0$ and $y/D = 5$. There are $n_i = 250$ nodes along x and $n_j = 150$ nodes along y. 900 rays are shot from 250° to 340° (x-axis reference), the time step is $\Delta t = 5 \times 10^{-6}$ s. The real parts of g_L computed with ray-tracing and analytically are shown in Figures 5.10 and 5.11 respectively, for 5000 Hz. The agreement is excellent. The same conclusions can be drawn at 10000Hz, as seen in Figures 5.12 and 5.13.

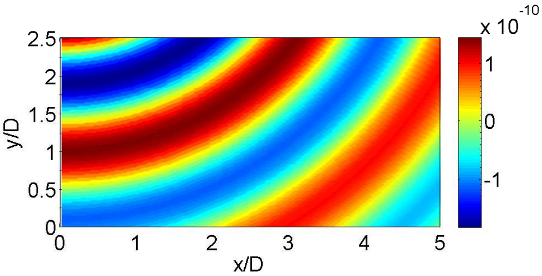

Figure 5.10: Quiescent medium, Re(g_L), 5000 Hz, ray-tracing

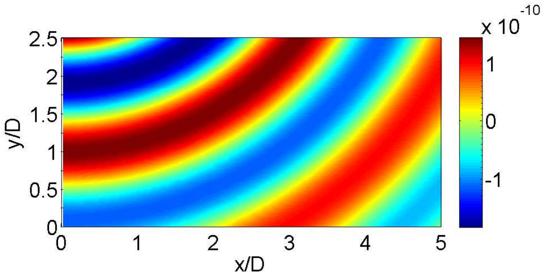

Figure 5.11: Quiescent medium, Re(g_L), 5000 Hz, analytical

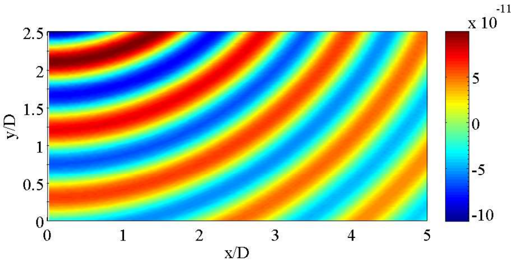

Figure 5.12: Quiescent medium, Re(g_L), 10000 Hz, ray-tracing

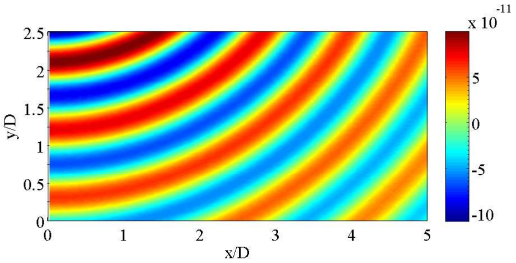

Figure 5.13: Quiescent medium, Re(g_L), 10000 Hz, analytical

Uniform mean flow

In this second test case, a uniform flow parallel to the x-axis is set to $v_1 = -100$ m/s (air flows from right to left). The following relation still holds,

$$g_L(\boldsymbol{x}, \boldsymbol{y}, \omega) = \frac{1}{i\omega c^2} g_u(\boldsymbol{x}, \boldsymbol{y}, \omega) \tag{5.51}$$

where g_u is the Green's function of the advected wave equation for a subsonic uniform flow along the x-axis. According to Howe [35],

$$g_u(\boldsymbol{x}, \boldsymbol{y}, \omega) = \frac{\exp\left(ik\left[\left(\frac{R^2}{1-M^2} + \frac{M^2(x_1-y_1)^2}{(1-M^2)^2}\right)^{1/2} - \frac{M(x_1-y_1)}{1-M^2}\right]\right)}{4\pi\sqrt{1-M^2}\left(R^2 + \frac{M^2(x_1-y_1)^2}{1-M^2}\right)^{1/2}} \tag{5.52}$$

where M is the flow Mach number. This analytical expression is compared to results from ray-tracing.

The real parts of g_L are compared in Figures 5.14 and 5.15 at 5000 Hz. The imaginary parts are compared in Figures 5.16 and 5.17. The overall agreement is excellent. The influence of the mean flow on the acoustic field is self-evident in comparison with the previous case. The mean flow bends the wave fronts and shortens the wavelengths moving in the opposite direction to the flow.

Supersonic jet flow

The method is finally applied to a supersonic jet flow configuration, at $M_j = 1.15$. The adjoint problem is considered, that is the source is not located in the jet, but rather at

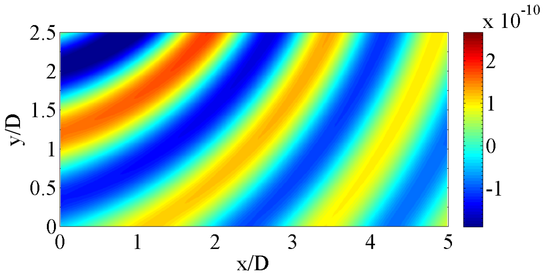

Figure 5.14: Uniform flow, Re(g_L), 5000 Hz, ray-tracing

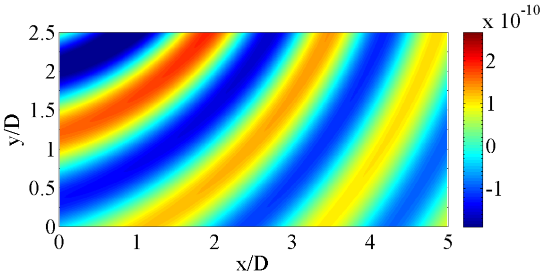

Figure 5.15: Uniform flow, Re(g_L), 5000 Hz, analytical

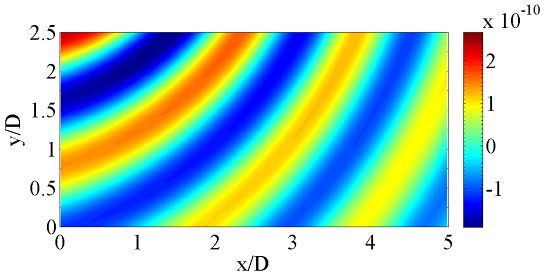

Figure 5.16: Uniform flow, Im(g_L), 5000 Hz, ray-tracing

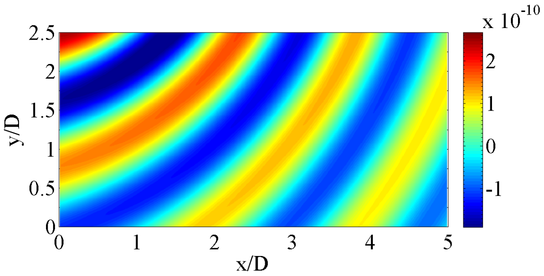

Figure 5.17: Uniform flow, Im(g_L), 5000 Hz, analytical

the observer location ($x/D = 0$, $y/D = 5$). The original flow field is also reversed, as described in Section 5.3.4. The computational domain extends over $0 \leq x/D \leq 5$ and $0 \leq y/D \leq 2.5$, 900 rays are shot from 260° to 350° with respect to the jet axis, the time step is $dt = 5.0 \times 10^{-7}$ s. There are 600 points along the x axis and 300 points along the y axis.

The results are shown in Figures 5.18 and 5.19, for the real and imaginary parts respectively. The incident wave is progressively bent by the jet flow and the wavelengths are clearly shortened, as expected.

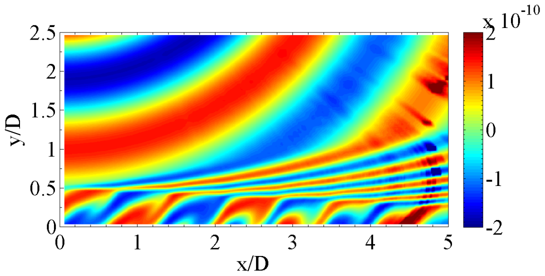

Figure 5.18: Visualization of Re(g_L) at 5000 Hz, computed with ray tracing. Supersonic jet flow, $M_j = 1.15$.

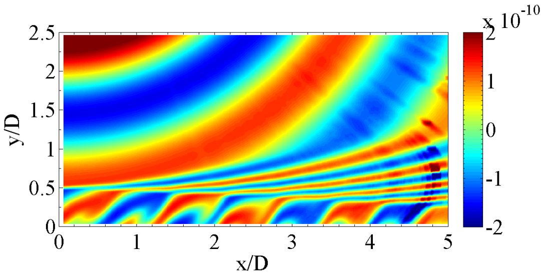

Figure 5.19: Visualization of Im(g_L) at 5000 Hz, computed with ray tracing. Supersonic jet flow, $M_j = 1.15$.

5.4 Computation of the vector Green's function

Once the Green's function of Lilley's equation g_L is known, the vector Green's functions of the LEE Π_n may be computed, by differentiating g_L, as seen in Equation (5.10). The differentiation steps are presented in this section, as well as two test cases.

5.4.1 Calculation of the derivatives of g_L

Thanks to the ray-tracing algorithm, g_L is known along the rays. In order to differentiate g_L, the function is first interpolated onto a regular grid, usually the same as the one for the flow field. The closest neighbor is used for interpolation, this requires a sufficient number of rays as well as a small enough time step, in order to cover the grid regularly. The typical refinement used is shown in Figure 5.20.

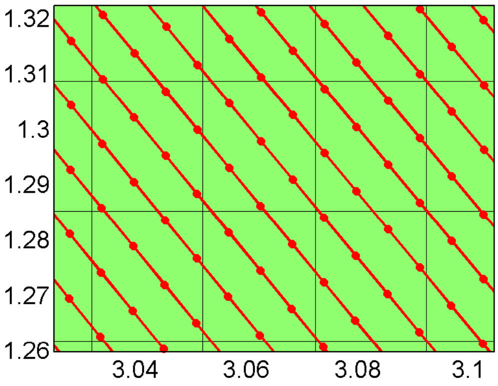

Figure 5.20: Rays over a regular mesh. The dots represent successive time steps.

Differentiation of g_L is then performed on the grid using a fourth order finite difference scheme. The coefficients of the scheme are given in Appendix B.3.1. Along the grid boundaries, derivatives are computed using first order finite differences.

5.4.2 Test cases

The previous test cases are now extended to the calculation of the vector Green's functions. As stated before, this requires the evaluation of the spatial derivatives of g_L (see Equation (5.10)). Hence, the derivatives computed with ray-tracing are compared to the analytical solution, and then Π_1 and Π_2 are shown.

Quiescent medium

The calculation is performed at 5000 Hz. Analytical expressions for the derivatives of g_L have been established and can be found in Appendix B.4. Comparisons are shown for dg_L/dx, dg_L/dy, d^2g_L/dx^2 and $dg_L/dxdy$, see Figures 5.21 to 5.28.

The overall agreement is excellent, this is essential because these calculations are used to compute Π_1 and Π_2, which are readily computed. Comparisons for both real and imaginary parts are presented in Figures 5.29 to 5.36. Again the agreement is excellent.

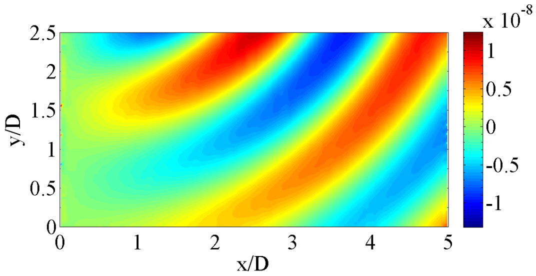

Figure 5.21: Quiescent medium, Re(dg_L/dx), 5000 Hz, ray-tracing

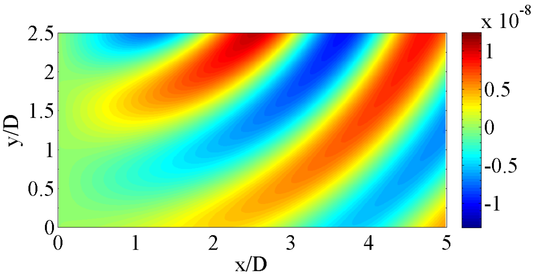

Figure 5.22: Quiescent medium, Re(dg_L/dx), 5000 Hz, analytical

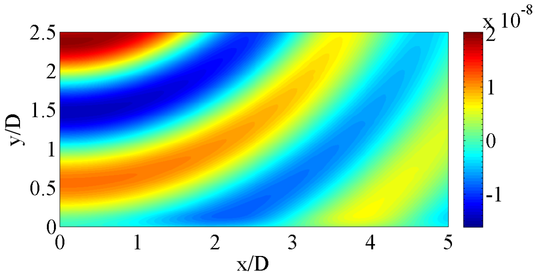

Figure 5.23: Quiescent medium, Re(dg_L/dy), 5000Hz, ray-tracing

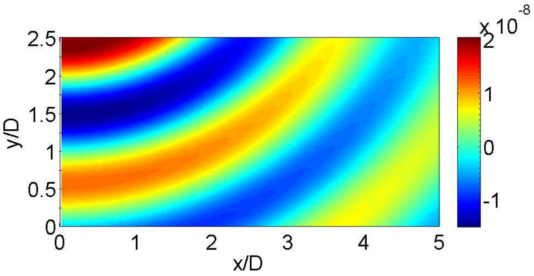

Figure 5.24: Quiescent medium, Re(dg_L/dy), 5000Hz, analytical

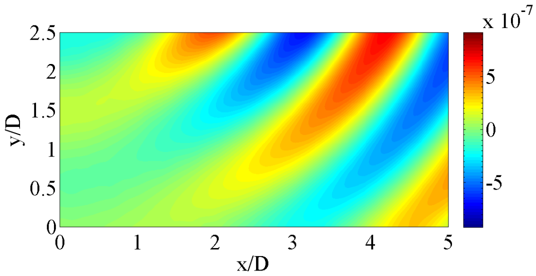

Figure 5.25: Quiescent medium, Re(d^2g_L/dx^2), 5000Hz, ray-tracing

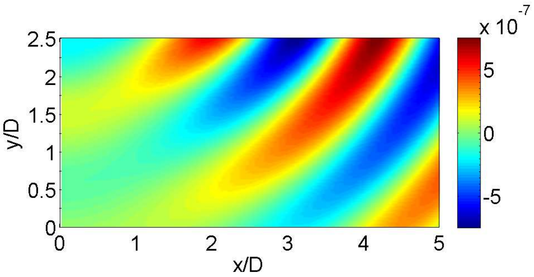

Figure 5.26: Quiescent medium, Re(d^2g_L/dx^2), 5000Hz, analytical

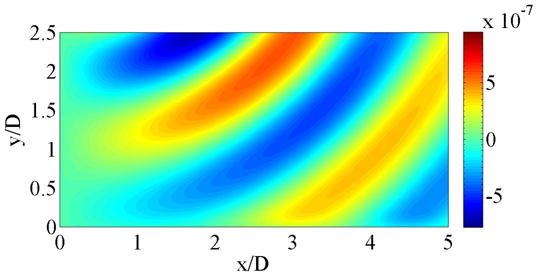

Figure 5.27: Quiescent medium, Re($d^2g_L/dxdy$), 5000Hz, ray-tracing

.

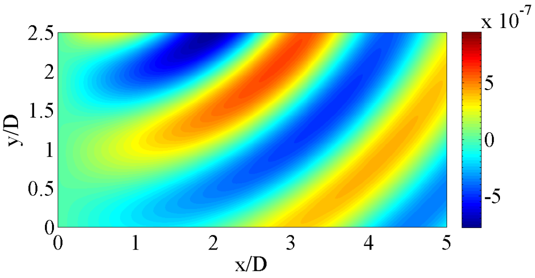

Figure 5.28: Quiescent medium, Re($d^2g_L/dxdy$), 5000Hz, analytical

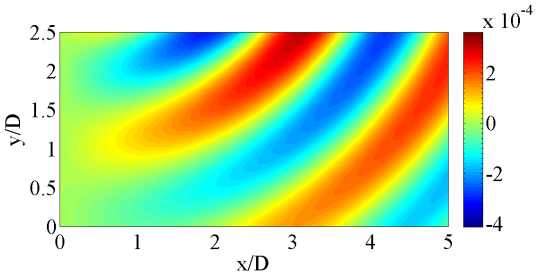

Figure 5.29: Quiescent medium, $\mathrm{Re}(\Pi_1)$, 5000Hz, ray-tracing

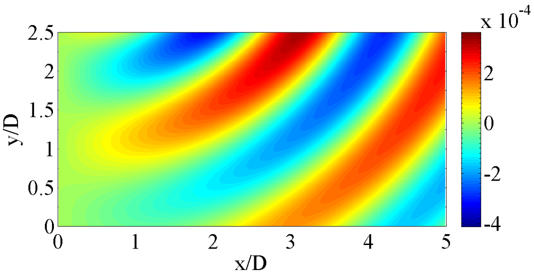

Figure 5.30: Quiescent medium, $\mathrm{Re}(\Pi_1)$, 5000Hz, analytical

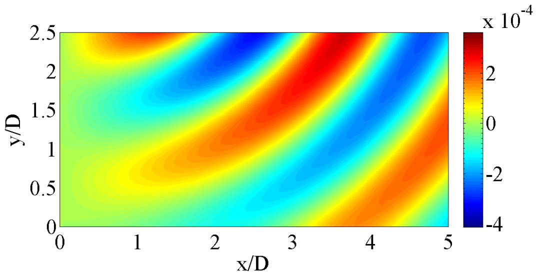

Figure 5.31: Quiescent medium, $\mathrm{Im}(\Pi_1)$, 5000Hz, ray-tracing

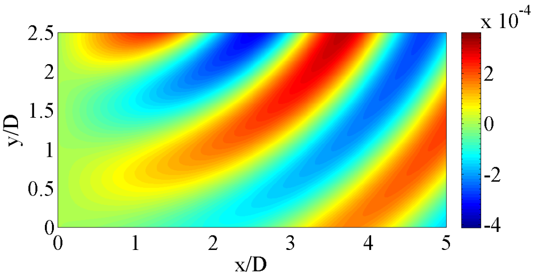

Figure 5.32: Quiescent medium, $\mathrm{Im}(\Pi_1)$, 5000Hz, analytical

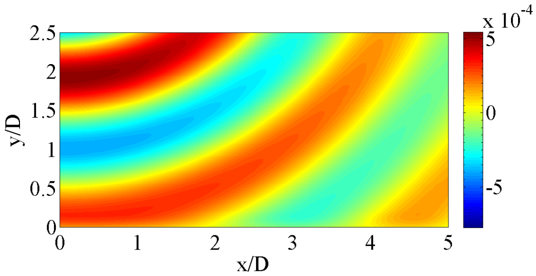

Figure 5.33: Quiescent medium, $\mathrm{Re}(\Pi_2)$, 5000Hz, ray-tracing

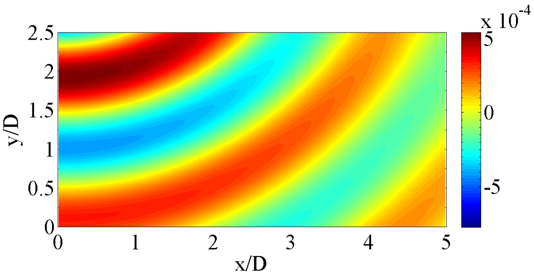

Figure 5.34: Quiescent medium, $\mathrm{Re}(\Pi_2)$, 5000Hz, analytical

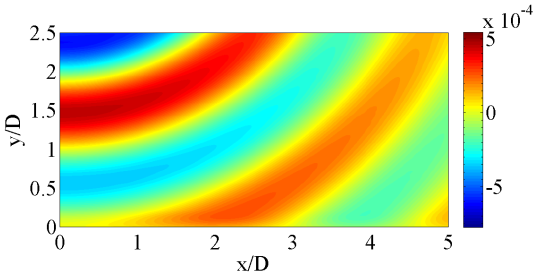

Figure 5.35: Quiescent medium, $\mathrm{Im}(\Pi_2)$, 5000Hz, ray-tracing

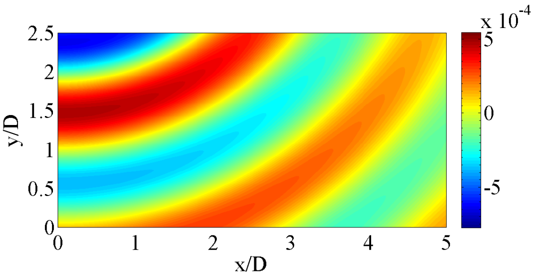

Figure 5.36: Quiescent medium, $\mathrm{Im}(\Pi_2)$, 5000Hz, analytical

Uniform mean flow

Π_1 and Π_2 are now computed for the case of a uniform flow. Computed results for real and imaginary parts are shown in Figures 5.37 to 5.40. The comparison is not performed with analytical results, but since the calculation of g_L on a uniform flow, as well as the differentiation algorithm on the grid have been validated, Π_1 and Π_2 are expected to be computed correctly. Again, the effect of the flow on Π_1 and Π_2 is clearly visible on the visualizations.

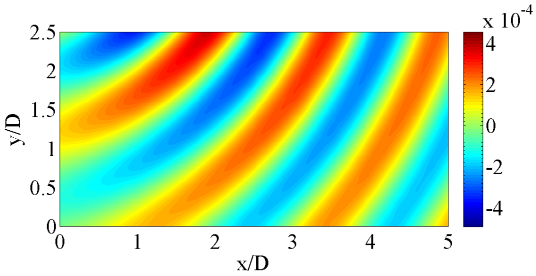

Figure 5.37: Uniform flow, $\text{Re}(\Pi_1)$ 5000Hz, ray-tracing

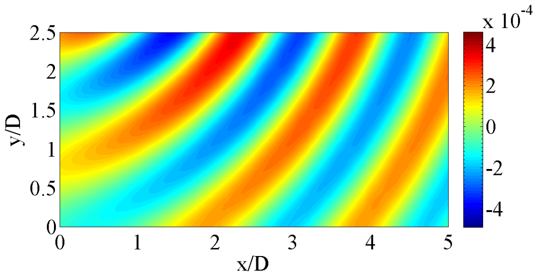

Figure 5.38: Uniform flow, $\text{Im}(\Pi_1)$ 5000Hz, ray-tracing

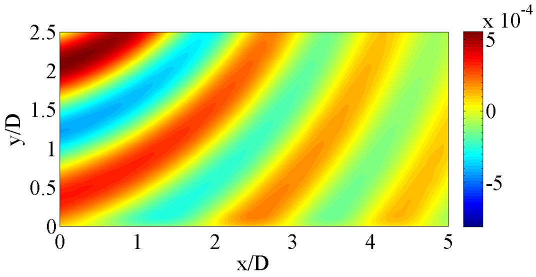

Figure 5.39: Uniform flow, $\text{Re}(\Pi_2)$ 5000Hz, ray-tracing

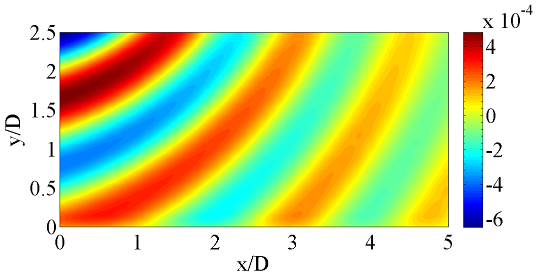

Figure 5.40: Uniform flow, $\text{Im}(\Pi_2)$ 5000Hz, ray-tracing

Supersonic jet flow

The real parts of Π_1 and Π_2 for the supersonic jet flow at $M_j = 1.15$ are shown in Figures 5.41 and 5.42. Refraction by the shear layer of the jet is again clearly visible, and those results are encouraging for acoustic predictions.

5.5 Final formulation

The vector Green's functions associated with the LEE have been calculated using ray-tracing. For PSD calculations, the adjoint Green's functions Π_n^a are used. For clarity it is recalled that the first argument of the Green's function is the observer location, whereas the second argument is the source location. The adjoint and direct Green's functions are related by,

$$\Pi_n(\underbrace{\boldsymbol{x}}_{\text{observer}}, \underbrace{\boldsymbol{y}}_{\text{source}}, \omega) = \Pi_n^a(\underbrace{\boldsymbol{y}}_{\text{observer}}, \underbrace{\boldsymbol{x}}_{\text{source}}, \omega) \tag{5.53}$$

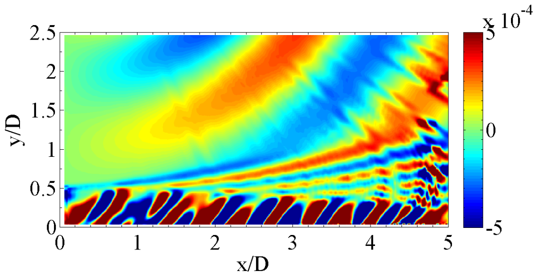

Figure 5.41: Visualization of Re(Π_1) at 5000 Hz, computed with ray tracing. Supersonic jet flow, $M_j = 1.15$.

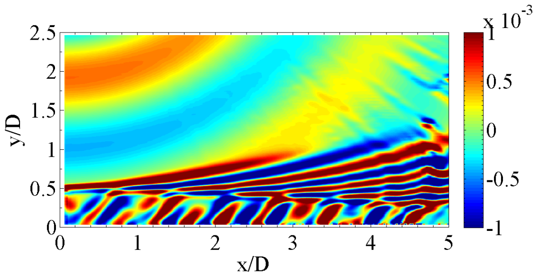

Figure 5.42: Visualization of Re(Π_2) at 5000 Hz, computed with ray tracing. Supersonic jet flow, $M_j = 1.15$.

In terms of the adjoint Green's function, S_{pp} is given by,

$$S_{pp}(\boldsymbol{x},\omega) = (\rho_\infty c_\infty^2)^2 \int \dots \int \Pi_n^a(\boldsymbol{y_1},\boldsymbol{x},-\omega)\Pi_m^{a*}(\boldsymbol{y_1}+\boldsymbol{\eta},\boldsymbol{x},-\omega)R_{nm}(\boldsymbol{y_1},\boldsymbol{\eta},\tau)e^{-i\omega\tau}d\boldsymbol{y_1}d\boldsymbol{\eta}d\tau \tag{5.54}$$

The general form of the cross-correlation function is,

$$R_{mn}(\boldsymbol{y_1},\boldsymbol{\eta},\tau) = a_{mn}\,K\,\frac{p_s(\boldsymbol{y_1})p_s(\boldsymbol{y_1}+\boldsymbol{\eta})}{\rho_\infty^2 c_\infty^2 l^2}\exp\left[-\frac{|\xi|}{u_c\tau_s} - \frac{(\xi-u_c\tau)^2}{l^2} - \frac{\gamma^2+\zeta^2}{l_\perp^2}\right] \tag{5.55}$$

where the coefficient a_{mn} reflects the relative amplitude of the different terms of the cross-correlation. For isotropic turbulence, there is no global contribution of the cross terms ($m \neq n$), so that $a_{mn} = 0$ for $m \neq n$ here. It is also assumed that the auto-correlation terms have the same amplitude, so that $a_{11} = a_{22} = 0.5$. Then,

$$\begin{aligned} S_{pp}(\boldsymbol{x},\omega) = c_\infty^2 \int \dots \int \Pi_n^a(\boldsymbol{y_1},\boldsymbol{x},-\omega)\Pi_m^{a*}(\boldsymbol{y_1}+\boldsymbol{\eta},\boldsymbol{x},-\omega)a_{mn}\,K\,\frac{p_s(\boldsymbol{y_1})p_s(\boldsymbol{y_1}+\boldsymbol{\eta})}{l^2} \\ \exp\left[-\frac{|\xi|}{u_c\tau_s} - \frac{(\xi-u_c\tau)^2}{l^2} - \frac{\gamma^2+\zeta^2}{l_\perp^2}\right]e^{-i\omega\tau}d\boldsymbol{y_1}d\boldsymbol{\eta}d\tau \end{aligned} \tag{5.56}$$

As before, integration over τ is readily performed,

$$\int_\tau \exp\left[-\frac{(\xi-u_c\tau)^2}{l^2}\right]\exp(-i\omega\tau)d\tau = \exp\left(-i\omega\frac{\xi}{u_c}\right)\sqrt{\pi}\frac{l}{u_c}\exp\left(-\frac{\omega^2}{4}\frac{l^2}{u_c}^2\right) \tag{5.57}$$

So that the final expression for S_{pp} is,

$$\begin{aligned} S_{pp}(\boldsymbol{x},\omega) = c_\infty^2\sqrt{\pi} \int \dots \int \Pi_n^a(\boldsymbol{y_1},\boldsymbol{x},-\omega)\Pi_m^{a*}(\boldsymbol{y_1}+\boldsymbol{\eta},\boldsymbol{x},-\omega)a_{mn}\,K\,\frac{p_s(\boldsymbol{y_1})p_s(\boldsymbol{y_1}+\boldsymbol{\eta})}{l u_c} \\ \exp\left(-i\omega\frac{\xi}{u_c}\right)\exp\left(-\frac{\omega^2}{4}\frac{l^2}{u_c^2}\right)\exp\left[-\frac{|\xi|}{u_c\tau_s} - \frac{\gamma^2+\zeta^2}{l_\perp^2}\right]d\boldsymbol{y_1}d\boldsymbol{\eta} \end{aligned} \tag{5.58}$$

In Appendix D, it is shown that when neglecting the mean flow effects, this expression reduces to the formulation without refraction effects, see Equation (3.49).

5.6 Conclusion

The acoustic model has been formally extended to account for refraction effects. This is achieved by numerically computed the Green's functions of the problem. The scalar Green's function, related to Lilley's equation is computed with ray-tracing. Then, it is related to the vector Green's functions of the LEE used in the model. The calculation have been successfully validated on simple test cases. The model may now be applied to real configurations.

Chapter 6

BBSAN of jets in flight

This chapter addresses the case of shocked jets in flight conditions, simulated with a secondary nozzle, co-axial to the main nozzle. As indicated in Section 1.3, flight is expected to modify the aerodynamics and acoustics of the jet.

6.1 Case description

The experimental setup is shown in Figure 6.1: the main nozzle in gray corresponds to the secondary stream of a civil engine, whereas the surrounding nozzle in blue accounts for the external flow encountered in flight. The diameter of the secondary nozzle is $D_s = 200$ mm. Air may be driven up to $M_{\text{ext}} = 0.39$ in the secondary nozzle. This is of course less than in real flight conditions, but this is due to facility limitations. The chosen operating conditions are $M_j = 1.15$, $M_j = 1.35$ and $M_{\text{ext}} = 0.22$, $M_{\text{ext}} = 0.39$. In order to assess the numerical prediction capabilities, RANS simulations and acoustic simulations have

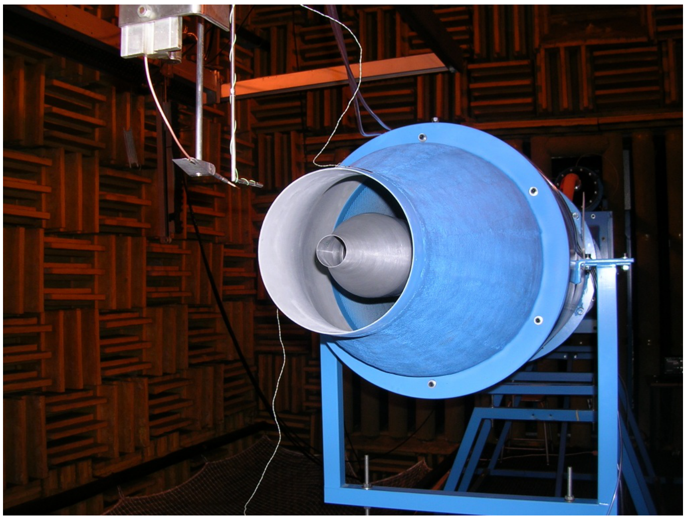

Figure 6.1: Photo of the experimental setup used at ECL by B. André [3]. The diameter of the primary nozzle is $D = 0.038$ m, the diameter of the external nozzle is $D_{\text{ext}} = 0.02$ m

been performed. The first part of this chapter focuses on the aerodynamic results, while acoustic results are detailed in the second part.

6.2 Aerodynamics of supersonic jets in flight

The aerodynamics are studied in a similar way to the studies in Chapter 4 for jets in static conditions.

6.2.1 Schlieren visualization

An average view of 500 Schlieren images is shown in Figure 6.2 for $M_j = 1.15$ and $M_{\text{ext}} = 0.22$. The calculation is in the upper part and the measurement in the lower part. The agreement is good, as far as shock location is concerned. It should be noted that in the measurements, the flow right after $x/D = 0$ is hidden: this is because the camera is located on the side of the jet, outside of the secondary flow, so that the secondary nozzle hides a small portion of the initial primary flow. This is clearly seen in Figure 6.2 (a): the tip of the expansion fan does not reach $y/D = 0/5$ at $x/D = 0.0$. Experimental images have been shifted consequently to account for this phenomenon.

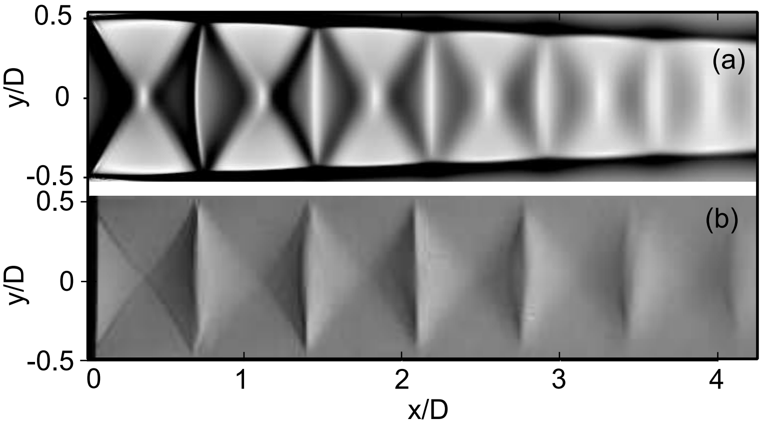

Figure 6.2: Average view of Schlieren images of a $M_j = 1.15$ jet, $M_{\text{ext}} = 0.22$. (a): calculation, (b): measurement

The effect of flight on Schlieren visualizations is seen in Figures 6.3 and 6.4 for $M_j = 1.15$ and $M_j = 1.35$ respectively: visualization for three external Mach numbers are compared for both M_j. Independently of M_j, it is observed that the first two cells seems unaffected by the external flow. This agrees with Morris [54]: the external boundary layer on the primary nozzle make the first cells insensitive to the freestream. The third and subsequent cells lengthen with M_{ext} though.

6.2.2 Static pressure

Case $M_j = 1.15$

The computed and measured profiles of static pressure on the jet axis are compared in Figures 6.5 and 6.6 for $M_{\text{ext}} = 0.22$ and $M_{\text{ext}} = 0.39$ respectively. As already observed in

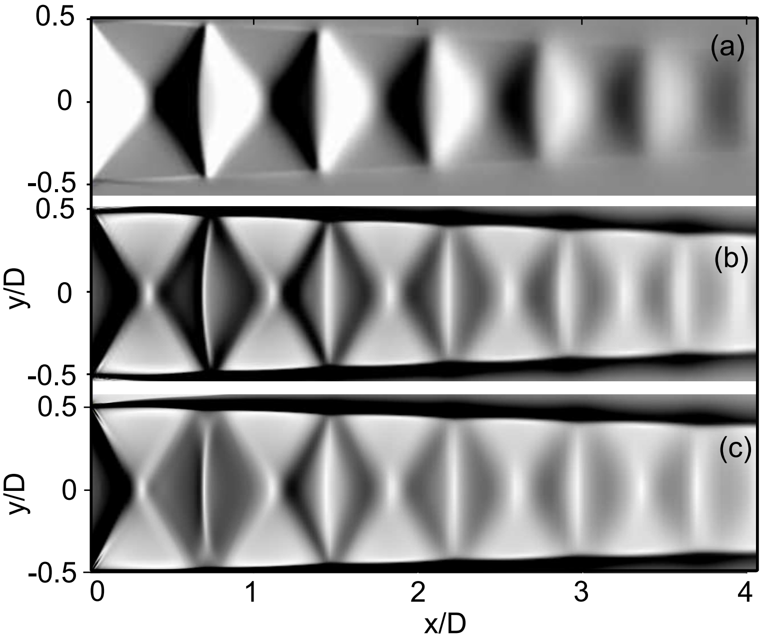

Figure 6.3: Average view of Schlieren images of a $M_j = 1.15$ jet. Calculations for different M_{ext}: (a) $M_{\text{ext}} = 0.0$, (b): $M_{\text{ext}} = 0.22$, (c): $M_{\text{ext}} = 0.39$

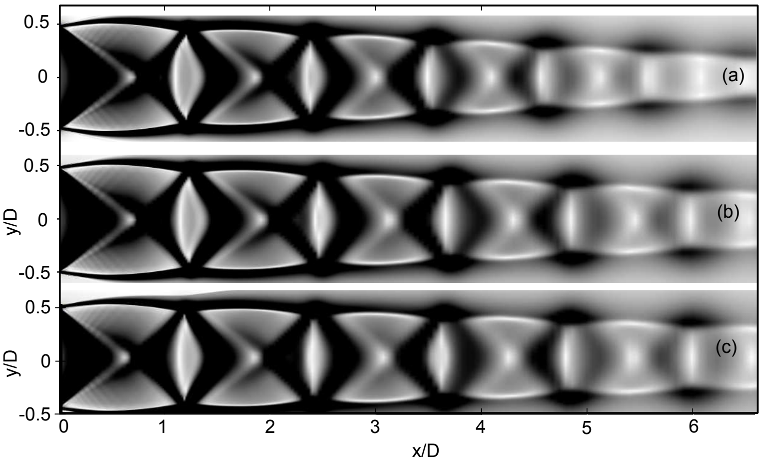

Figure 6.4: Average view of Schlieren images of a $M_j = 1.35$ jet. Calculations for different M_{ext}: (a) $M_{\text{ext}} = 0.0$, (b): $M_{\text{ext}} = 0.22$, (c): $M_{\text{ext}} = 0.39$

the Schlieren visualizations, the shocks are located correctly for both M_{ext}. The amplitude decay is nonetheless faster in the calculations than measurements. This could lead to an underestimation of the noise sources located downstream when computing BBSAN.

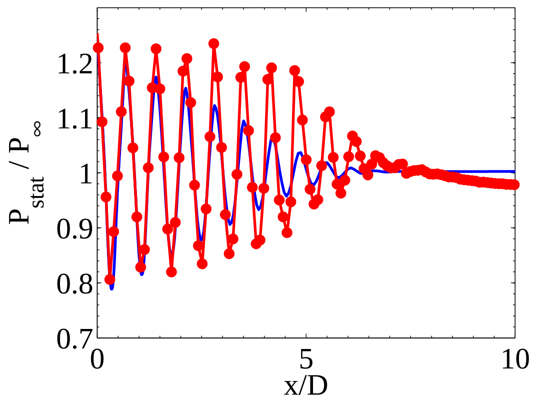

Figure 6.5: Static pressure on the jet axis, $M_j = 1.15$, $M_{\text{ext}} = 0.22$. —— calculation, —●— measurement

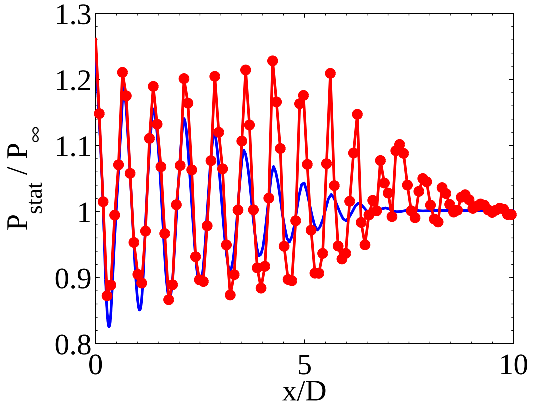

Figure 6.6: Static pressure on the jet axis, $M_j = 1.15$, $M_{\text{ext}} = 0.39$. —— calculation, —●— measurement

Norum & Brown [59] observed that increasing M_{ext} lead to a longer quasi-periodic structure. The difference in their measurements at $M_j = 1.8$, between $M_{\text{ext}} = 0$ and $M_{\text{ext}} = 0.9$ is obvious, this is because the development of the jet is slowed by the freestream.

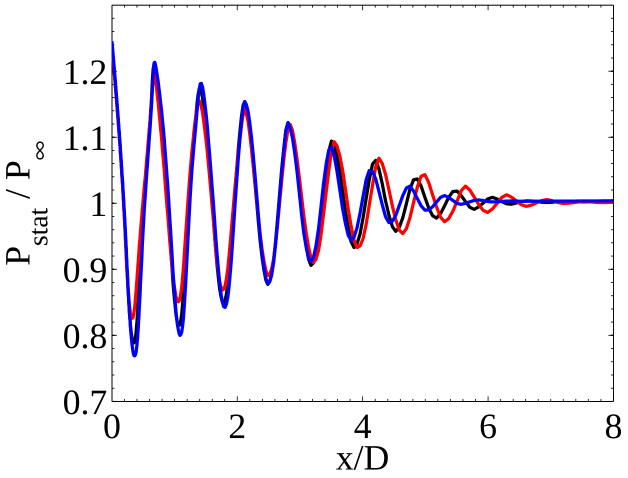

Figure 6.7: Calculated pressure profiles on the jet axis of a $M_j = 1.15$ jet. —●— $M_{\text{ext}} = 0.0$, —●— $M_{\text{ext}} = 0.22$, —●— $M_{\text{ext}} = 0.39$

The effect of M_{ext} in the calculations is easily seen in Figure 6.7, where the calculated pressure profiles on the jet axis for three M_{ext} are shown. The shock-structure as a whole is a bit longer for $M_{\text{ext}} = 0.39$ than for static conditions. Though the first shock-cells are not sensitive to M_{ext}, a gradual stretch is also visible from the fifth cell till the end of the structure.

Case $M_j = 1.35$

The agreement between calculations and measurements is better in this case than in the previous one: the predicted amplitudes of the first cells are close to measurements and decay accordingly, see Figures 6.8 and 6.9.

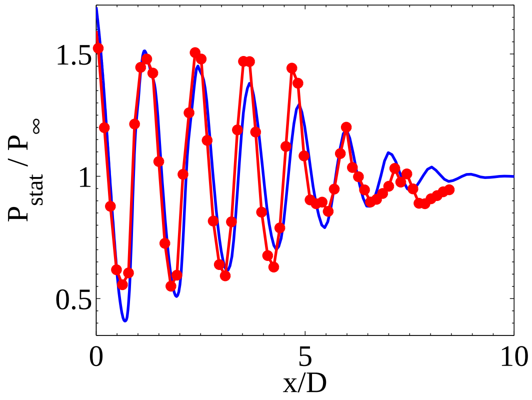

Figure 6.8: Static pressure on the jet axis, $M_j = 1.35$, $M_{\text{ext}} = 0.22$. —— calculation, —●— measurement

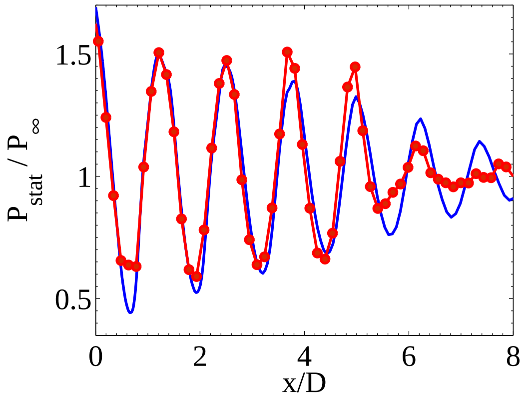

Figure 6.9: Static pressure on the jet axis, $M_j = 1.35$, $M_{\text{ext}} = 0.39$. —— calculation, —●— measurement

The effect of the external stream is visible from the third cell downstream in the calculation, see Figure 6.10: the calculated pressure profiles on the jet axis show a gradual stretching of the shock structure with M_{ext} as well as a slower amplitude decay.

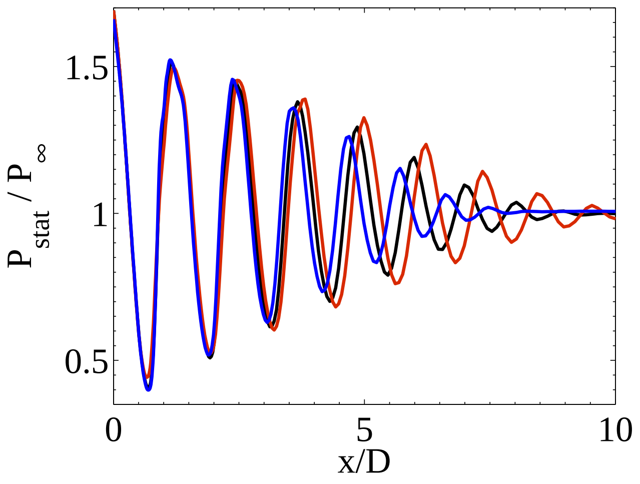

Figure 6.10: Calculated pressure profiles on the jet axis of a $M_j = 1.35$ jet. —●— $M_{\text{ext}} = 0.0$, —●— $M_{\text{ext}} = 0.22$, —●— $M_{\text{ext}} = 0.39$

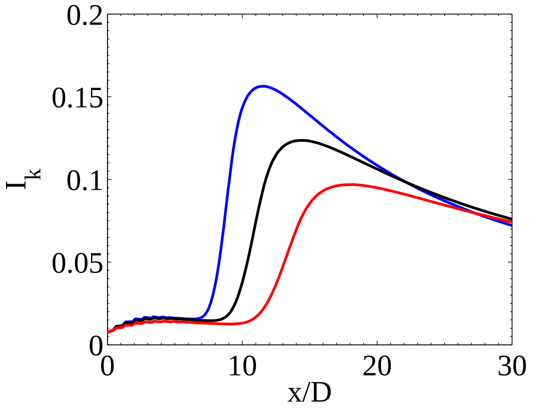

Figure 6.11: Calculated turbulence intensity profiles on the jet axis of a $M_j = 1.15$ jet. —●— $M_{\text{ext}} = 0.0$, —●— $M_{\text{ext}} = 0.22$, —●— $M_{\text{ext}} = 0.39$

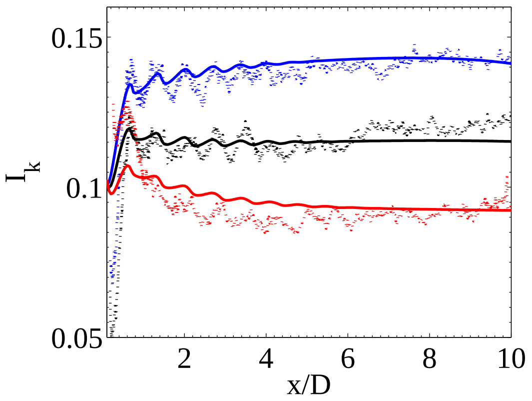

Figure 6.12: Axial turbulence rate, $y/D = 0.5$, $M_j = 1.15$. Calculations: —— $M_{\text{ext}} = 0.0$, —— $M_{\text{ext}} = 0.22$, —— $M_{\text{ext}} = 0.39$. Measurements: ··· $M_{\text{ext}} = 0.0$, ··· $M_{\text{ext}} = 0.22$, ··· $M_{\text{ext}} = 0.39$

6.2.3 Turbulence

The influence of M_{ext} on the jet development is well demonstrated by studying axial profiles of I_k for different M_{ext}. In Figures 6.11 and 6.12, I_k at $M_j = 1.15$ is shown for $y/D = 0$ and $y/D = 0.5$ respectively. The peak value of I_k on the jet axis is a decreasing function of M_{ext}. Without the freestream, I_k peaks at more than 15% whereas it peaks at less than 10% at $M_{\text{ext}} = 0.39$. Turbulence intensity on the jet axis is thus diminished by the freestream. It is also worth noting that the peak location moves downstream as M_{ext} increases. This means that the turbulent development of the jet is slowed by the freestream. Along the lip line, calculated values of I_k are compared to measurements. The agreement is good. Fluctuations reflect the influence of the shock-cell structure in the mixing layer. I_k decreases with M_{ext} similarly to what is found on the jet axis.

Similar plots for I_k are shown for $M_j = 1.35$ in Figures 6.13 and 6.14 respectively. The same conclusions may be drawn.

Hence, the freestream reduces shear in the shear layer, resulting in a slower turbulent development of the jet. In turn, this lengthens the shock-cell structure, as observed on the pressure profiles.

6.2.4 Length and strength of the shock-cells

The influence of M_{ext} on the shock-cell length is now examined, for $M_j = 1.15$ and $M_j = 1.35$, in Figures 6.15 and 6.16 respectively. The first cells are not significantly affected by the freestream as observed before. The global trend for both M_j is the higher M_{ext}, the longer the shock-cells. This is consistent with what was seen before. From an acoustic perspective, the increase in shock-cell length is expected to decrease the peak frequency of BBSAN

In Figures 6.17 and 6.18, the influence of M_{ext} on the shock strength at $M_j = 1.15$ and $M_j = 1.35$ is shown. The conclusions are the same for both M_j: the first cells are weakened by flight, whereas the shock strength is increased for the last cells. The overall

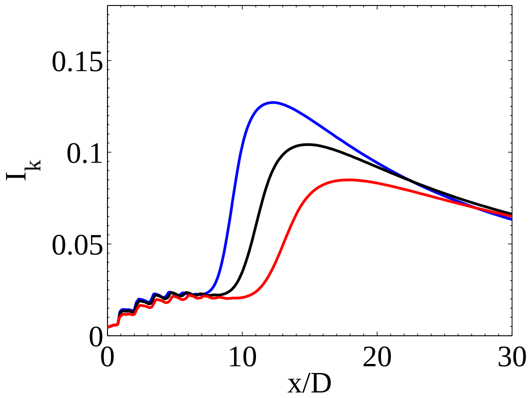

Figure 6.13: Calculated turbulence intensity profiles on the jet axis of a $M_j = 1.15$ jet. —●— $M_{\text{ext}} = 0.0$, —●— $M_{\text{ext}} = 0.22$, —●— $M_{\text{ext}} = 0.39$

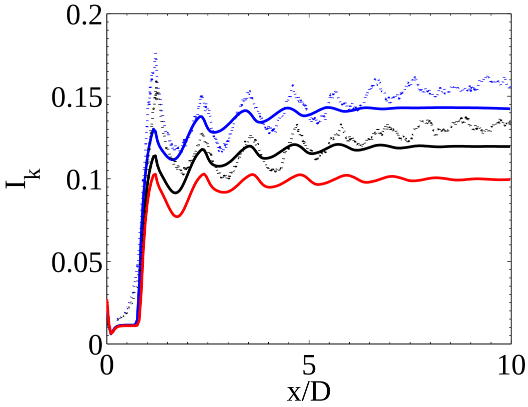

Figure 6.14: Axial turbulence rate, $y/D = 0.5$, $M_j = 1.15$. Calculations: —— $M_{\text{ext}} = 0.0$, —— $M_{\text{ext}} = 0.22$, —— $M_{\text{ext}} = 0.39$. Measurements: ··· $M_{\text{ext}} = 0.0$, ··· $M_{\text{ext}} = 0.22$

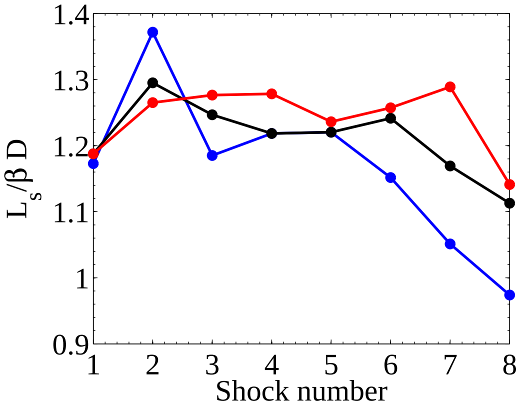

Figure 6.15: Shock-cell length versus shock-number at $M_j = 1.15$: —●— $M_{\text{ext}} = 0.0$, —●— $M_{\text{ext}} = 0.22$, —●— $M_{\text{ext}} = 0.39$

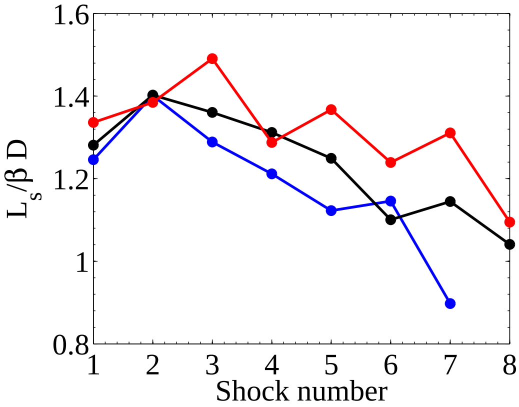

Figure 6.16: Shock-cell length versus shock-number at $M_j = 1.35$: —●— $M_{\text{ext}} = 0.0$, —●— $M_{\text{ext}} = 0.22$, —●— $M_{\text{ext}} = 0.39$

influence of M_{ext} is moderate though.

As observed in the static case, shocks are much stronger at $M_j = 1.35$ than at $M_j = 1.15$.

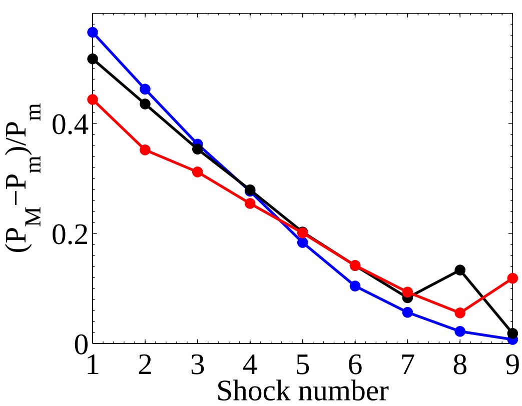

Figure 6.17: Calculated shock-strength at $M_j = 1.15$ for different M_{ext}: —●— $M_{\text{ext}} = 0.0$, —●— $M_{\text{ext}} = 0.22$, —●— $M_{\text{ext}} = 0.39$

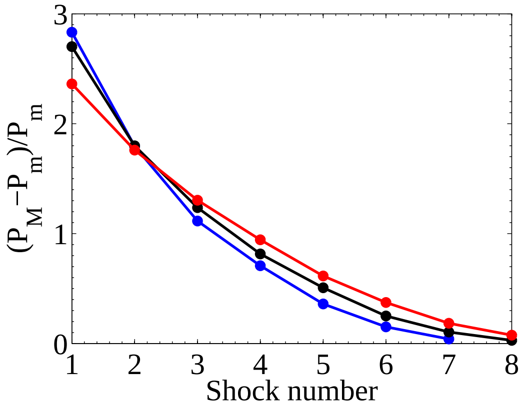

Figure 6.18: Calculated shock-strength at $M_j = 1.35$ for different M_{ext}: —●— $M_{\text{ext}} = 0.0$, —●— $M_{\text{ext}} = 0.22$, —●— $M_{\text{ext}} = 0.39$

6.3 Assessment of the acoustic model

The previous aerodynamic fields are used to compute the sources of BBSAN. Nonetheless ray-tracing calculations, that is propagation effects, are performed on a simplified aerodynamic field defined by $M = 0$ for $y > D_s$ and $M = M_{\text{ext}}$ for $0 \leq y \leq D_s$. Refraction occurring between the secondary stream and ambient medium in the ECL experiment is thus correctly accounted for.

The PSDs using the numerical Green's function at $M_j = 1.35$ for $M_s = 0.22$ and $M_s = 0.39$ are shown in Figures 6.19-6.22. Comparison is made with PSDs using the free-field Green's function, and with experiments.

Numerically computing the Green's function results in a more accurate estimation of the peak frequency, this is clearly seen in Figures 6.21 and 6.23 for $M_s = 022$ and $M_s = 0.39$ respectively. Numerical Green's functions result in a lower peak frequency, closer to experiments for all angles. This is also true for harmonics of f_p, as shown in Figure 6.20. Nevertheless, at lower frequencies, the numerical calculations lead to sharply rising levels, which is not physical, except for $\theta = 90^{\circ}$. This is not understood for now on and requires further investigations.

6.3.1 Results at $M_j = 1.35$ and $M_s = 0.22$

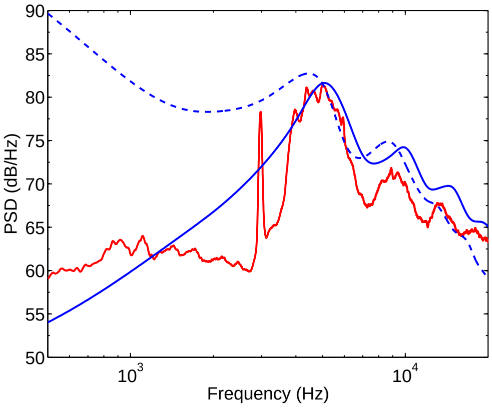

Figure 6.19: PSDs at $M_j = 1.35$ and $M_s = 0.22$, $\theta = 130^{\circ}$. —— measurement, - - - numerical Green's function, —— analytical Green's function

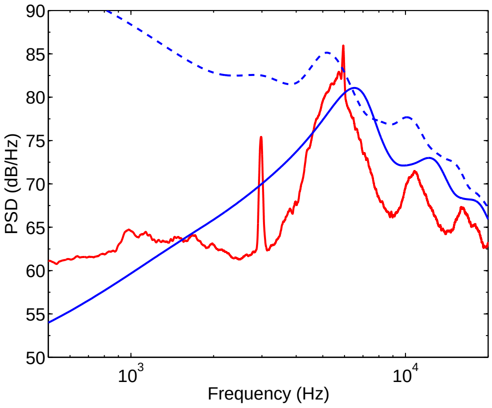

Figure 6.20: PSDs at $M_j = 1.35$ and $M_s = 0.22$, $\theta = 110^{\circ}$. —— measurement, - - - numerical Green's function, —— analytical Green's function

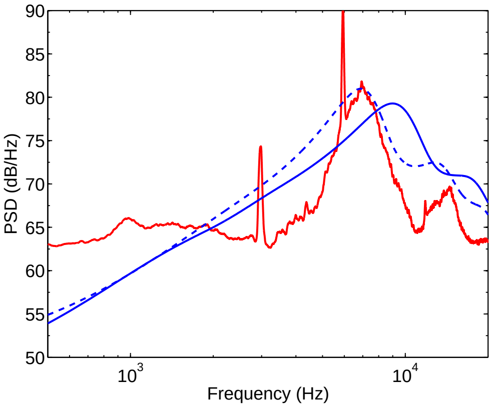

Figure 6.21: PSDs at $M_j = 1.35$ and $M_s = 0.22$, $\theta = 90^{\circ}$. —— measurement, - - - numerical Green's function, —— analytical Green's function

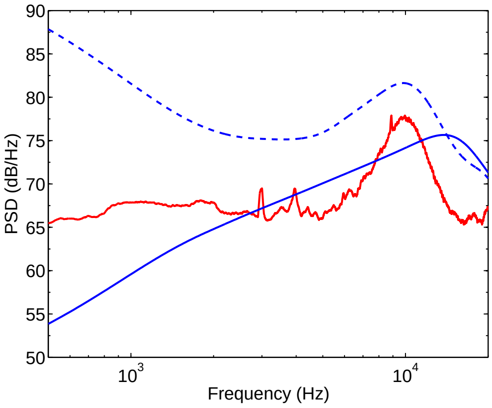

Figure 6.22: PSDs at $M_j = 1.35$ and $M_s = 0.22$, $\theta = 70^{\circ}$. —— measurement, - - - numerical Green's function, —— analytical Green's function

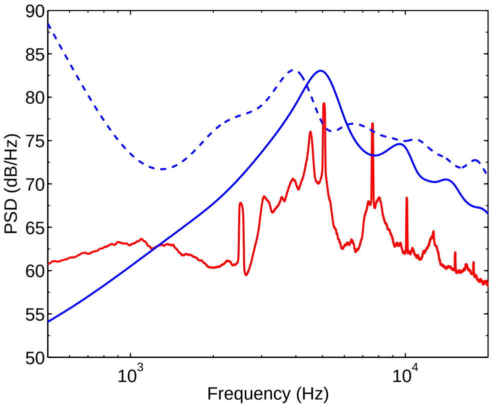

Figure 6.23: PSDs at $M_j = 1.35$ and $M_s = 0.39$, $\theta = 130^{\circ}$. —— measurement, - - - numerical Green's function, —— analytical Green's function

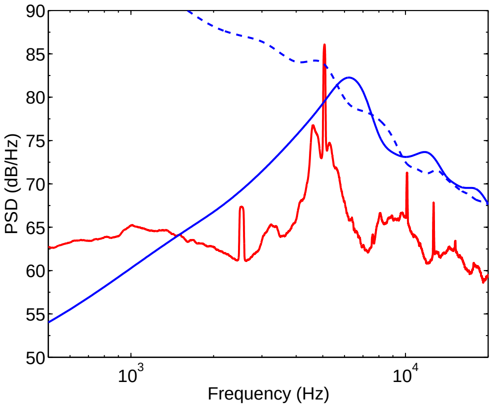

Figure 6.24: PSDs at $M_j = 1.35$ and $M_s = 0.39$, $\theta = 110^{\circ}$. —— measurement, - - - numerical Green's function, —— analytical Green's function

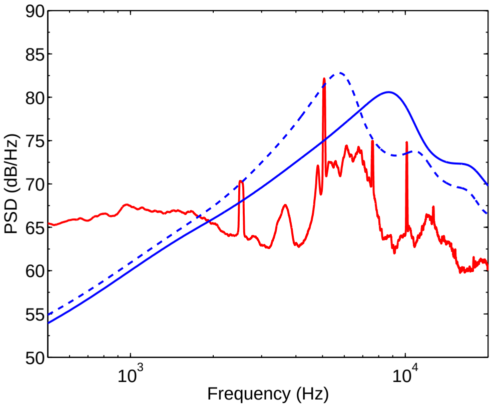

Figure 6.25: PSDs at $M_j = 1.35$ and $M_s = 0.39$, $\theta = 90^{\circ}$. —— measurement, - - - numerical Green's function, —— analytical Green's function

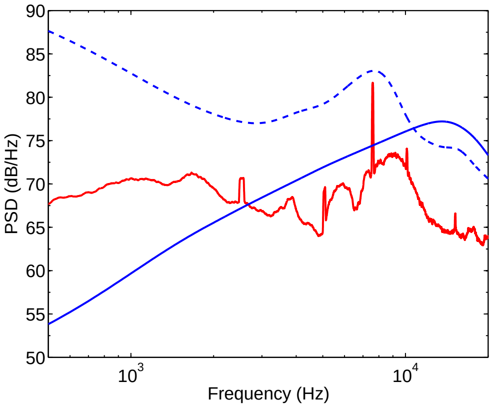

Figure 6.26: PSDs at $M_j = 1.35$ and $M_s = 0.39$, $\theta = 70^{\circ}$. —— measurement, - - - numerical Green's function, —— analytical Green's function

Conclusion

General conclusion

The objective of this research has been to develop a prediction method for BBSAN, using a calculation of the mean turbulent flow as an input for the model. This approach overcomes the shortcomings of simplified analytical models.

In the first chapter, the aero-acoustic features of supersonic shocked jets have been presented, along with the state of the art. Interaction between shock-cells and turbulence has been presented as the key mechanism generating BBSAN. Historical predictions methods of BBSAN have been described, as well as recent developments. The influence of flight on BBSAN has also been described. Flight modifies both the aerodynamics and acoustics of shocked jets.

The RANS equations, used to compute the mean turbulent flow have been presented in Chapter 2. Since the calculations are performed on shocked flows, the use of limiters is necessary to prevent the computation from diverging. The chosen limiters have been presented, as well as the $k-\omega-$SST turbulence model, that is used to account for turbulence in the calculations.

In the third chapter, a model for BBSAN has been derived analytically, starting from the work by Morris & Miller [56], to finally achieve a different formulation. The model relies on the LEE and a decomposition of the flow field among four contributions (mean flow, shock perturbations, turbulence perturbations, shock-turbulence interaction). A source term accounting for BBSAN has been identified by recasting this decomposition into the LEE. The LEE have then been arranged as a wave equation problem, solved with the free field Green's function. Correlation function and PSD of the acoustic signal have then been computed. At this stage, Morris & Miller use a spatial Fourier transform in their formulation, well-suited for academic cases and regular meshes. For the present model to be more general and easier to apply to complex configurations, a solution was obtained not to use the Fourier transform. Using a slightly different correlation function for the turbulent velocity fluctuations gave the desired result, so that the final expression for the PSD does not require the calculation of a Fourier transform.

In chapter four, the previous derivations have been applied to the case of static jets. First, it has been shown how to practically use a CFD solver to calculate the mean turbulent shocked flow. A robust methodology consisting of three main steps has been set up and presented. The methodology has been applied to jets at $M_j = 1.15$ and $M_j = 1.35$. The calculations have been compared favorably to measurements by André [3] at ECL. Comparisons include Schlieren visualizations, static pressure profiles, 2D velocity field with PIV and turbulence intensity. It has been shown that the calculations correctly predicted the shock locations, which is essential because it determines the peak frequency of BBSAN. The examination of pressure profiles demonstrated that the amplitude of the shocks agreed fairly well with measurements, which in turns determines the source strength and noise levels. The influence of the jet Mach number on the length and strength of the shock-cells has also been discussed. Acoustic results have then been presented. First, a grid convergence test has been successfully performed. Optimal size parameters for the acoustic computation grid have been isolated. Then, the developed model has been tested on a static jet at $M_j = 1.15$ and $M_j = 1.35$. For the various observation angles considered, the peak frequency and spectral width of BBSAN agree reasonably well with measurements. BBSAN source terms in the jet have been examined: they are located where shocks and turbulence interact. Their relative strength and spatial distribution vary with M_j and frequency. High frequency sources are mainly found close to the nozzle lip, where turbulence is essentially fine scale. At the peak frequency, sources extend all along the jet sonic boundary. Increasing M_j stretches the shock structure and increases the spatial extent of sources.

The fifth chapter studies refraction effects. The practical situations leading to refraction of acoustic waves have been described. Then, it has been shown that under a uniformly sheared and parallel flow assumption, the LEE may be recast into Lilley's equation to describe the propagation of acoustic perturbations in the flow. The Green's function technique is used to solve both Lilley's equation and the LEE. It has been shown how to compute g_L, the Green's function related to Lilley's equation, with ray tracing. The method has been applied successfully to simple test cases. The vector Green's functions associated with the LEE have then been derived from g_L and validations have been performed on test cases. A final formulation for the BBSAN model, including refraction effects has then been proposed.

The sixth and last chapter deals with flight effect on aerodynamics and acoustics. Flight has been simulated using an external stream surrounding the main jet, and flight Mach numbers M_f ranged up to $M_f = 0.39$. Measurements by André [3] have been used for comparison. Aerodynamic results have been presented first. Starting from Schlieren visualization, the objective was to observe and explain the influence of flight on the development of the shocked jet. The external stream has been found to delay the turbulent development of the jet, resulting in a stretched shock-cell pattern. The study of turbulent quantities confirmed that the reduced velocity difference across the jet shear layer lead to a slower development of turbulence. On average, the shock-cell length increases with M_f and the external stream reduces the decrease in shock-strength downstream. The acoustic model, including refraction effects, has been assessed on a supersonic jet at $M_j = 1.35$ surrounded by a subsonic jet at two Mach numbers $M_s = 0.22$ and $M_s = 0.39$. Numerically computing the Green's function results in a more accurate estimation of the peak frequency of BBSAN, as well as its harmonics. Nevertheless, at lower frequencies acoustic levels rise sharply which is not normal and should be investigated further.

Outlooks

Numerous evolutions may be contemplated, depending on the perspective under consideration. From a modeling perspective, the inclusion of temperature effects may also be considered, as proposed by Miller in [51]. A well-identified difficulty is that classical two-equation turbulence models are known to incorrectly account for temperature fluctuations. Georgiadis *et al.* [32] compared classical models such as the $k-\omega-\mathrm{SST}$ model to improved two-equation models for heated jet flow predictions. He concluded that some modifications could provide better predictions of mean axial velocities, but that those models do not improve upon standard models as far as the prediction of the turbulent kinetic energy is concerned. Since this quantity plays a major role in noise prediction, further research may be necessary before reaching such an application.

From an industrial point of view, an application of the model to more complex geometries is desirable. This may include 3D geometries with noise reduction technologies such as chevrons. In the wider frame of global jet noise prediction, the BBSAN model may be coupled to a mixing noise model such as the one by Tam & Auriault [84] for complete predictions. Another topic of interest concerns installation effects. That is, how the acoustic field produced by the jet plume is modified when the engine is mounted under the wing. A complete review of these effects is given by Fink [30]. More recently, Mengle [47] observed experimentally that parameters such as the nozzle-to-wing gully height and the flap angle modified the radiated sound field. A numerical characterization of these effects would be of real interest: it could provide key information on how to integrate the engine under the wing for better acoustic performance.

Successful comparisons with flight measurements is another essential perspective, for SNECMA and aircraft manufacturers such as Airbus. This would require the computation of the mean turbulent flow issuing from a typical commercial engine such as a CFM56-7B. Then, the complete acoustic model, including refraction effects, could be run and results compared to in flight measurements.

Bibliography

[1] R.K. Amiet. Refraction of sound by a shear layer. *Journal of Sound and Vibration*, 58:467–482, 1978. 33

[2] J.D. Anderson. *Modern compressible flow with historical perspective.* 2004. 20, 21

[3] B. André. *Étude expérimentale de l'effet du vol sur le bruit de choc de jets supersoniques sous-détendus.* PhD thesis, Ecole Centrale de Lyon, 2012. 15, 24, 26, 33, 65, 68, 71, 72, 73, 74, 75, 76, 79, 80, 111, 123, 124

[4] B. André, T. Castelain, and C. Bailly. Experimental exploration of an underexpanded supersonic jet. In *28th International Symposium on Shock Waves*, number 1, Manchester, 2011. 27, 61

[5] B. André, T. Castelain, and C. Bailly. Experimental exploration of an underexpanded supersonic jet. In *28th International Symposium on Shock Waves*, Manchester, 2011. 61

[6] B. André, T. Castelain, and C. Bailly. Experimental study of flight effects on screech in underexpanded jets. In *17th AIAA/CEAS Aeroacoustics Conference*, Portland, Oregon, USA, 2011. 61

[7] B. André, T. Castelain, and C. Bailly. Shock-tracking procedure for studying screech-induced oscillations. *AIAA Journal*, 49(7):1563–1566, 2011. 66, 67

[8] J. Atvars, L. K. Schubert, and H.S. Ribner. Refraction of sound from a point source placed in an air jet. *Journal of Acoustic Society of America*, 47(1A):168–170, 1970. 90

[9] C. Bailly, C. Bogey, and S. Candel. Modelling of sound generation by turbulent reacting flows. *International Journal of Aeroacoustics*, 9(4):461–490, 2010. 91

[10] C. Bailly and S. Candel. Prediction of supersonic jet noise from a statistical acoustic model and a compressible turbulence closure. *Journal of Sound and Vibration*, 194(2):219–242, July 1996. 31

[11] C. Bailly, S. Candel, and P. Lafon. Subsonic and supersonic jet noise predictions from statistical source models. *AIAA Journal*, 35(11):1688–1696, November 1997. 15

[12] C. Bailly and G. Comte-Bellot. *Turbulence.* CNRS Editions, 2002. 23, 40, 63

[13] W. Béchara, P. Lafon, C. Bailly, and S. Candel. Application of a k-epsilon turbulence model to the prediction of noise. 97(6):3518–3531, 1995. 15

[14] J. Boussinesq. *Essai sur la théorie des eaux courantes. Mémoires présentées par divers savants à l'Académie des Sciences. Paris.* 1877. 41

[15] G. L. Brown and A. Roshko. On density effects and large structure in turbulent mixing layers. *Journal of Fluid MechanicsB*, 64(4):775–816, 1974. 23, 24, 25

[16] E.J. Bultemeier, U.W. Ganz, J. Premo, and E. Nesbitt. Effect of uniform chevrons on cruise shockcell noise. *AIAA Aeroacoustics Conference*, 2006. 14

[17] S. Candel. Champ aérodynamique d'un jet chaud subsonique et structure cohérente. Technical report, 1974. 22, 63

[18] S. Candel. Application of geometrical techniques to aeroacoustic problems. In *13rd AIAA Aero-acoustics conference*, number 76, pages 1–13, Palo Alto, California, 1976. 93

[19] S. Candel. Numerical solution of conservation equations arising in linear wave theory: application to aeroacoustics. *Journal of Fluid Mechanics*, 83:466–493, 1977. 97

[20] S. Candel, A. Guedel, and A. Julienne. Radiation, refraction and scattering of acoustic waves in a free shear flow. In *13rd AIAA Aero-acoustics conference*, number 76, pages 1–17, Palo Alto, California, 1976. 93

[21] S. Candel, A. Julienne, and M. Julliand. Shielding and scattering by a jet flow. In *3rd AIAA Aero-acoustics conference*, number 76, pages 1–15, Palo Alto, 1976. 93

[22] T. Colonius, S.K. Lele, and P. Moin. Sound generation in a mixing layer. *Journal of Fluid Mechanics*, 330:375–409, 1997. 91

[23] S.C. Crow and F.H. Champagne. Orderly structure in jet turbulence. *Journal of Fluid Mechanics*, 48(03):547–591, 1971. 23, 25

[24] L. Davies, M.J. Fisher, and M.J. Barratt. The characteristics of the turbulence in the mixing region of a round jet. *Journal of Fluid Mechanics*, 15(3):337–367, 1962. 71

[25] P. Drevet, J.P. Duponchel, and J.R. Jacques. The effect of flight on jet noise as observed on the bertin Aérotrain. *Journal of Sound and Vibration*, 54(76):173–201, 1977. 32

[26] D.G. Duffy. *Green's functions with applications.* 1st edition, 2001. 51, 52

[27] P.A. Durbin. High frequency Green function for aerodynamic noise in moving media, Part 1: General theory. *Journal of Sound and Vibration*, 91:519–525, 1983. 92

[28] P.A. Durbin. High frequency Green function for aerodynamic noise in moving media, Part 2: Noise from a spreading jet. *Journal of Sound and Vibration*, 91:527–538, 1983. 92

[29] R. Emden. Über die Ausströmungserscheinungen permanenter Gase. *Annalen der Physik*, 69:426–453, 1899. 24

[30] M.R. Fink. Propulsive lift noise. In *Aeroacoustics of flight vehickes: theory and practive. Volume 1: noise sources*, pages 449–481. 1994. 125

[31] V. Fleury. *Superdirectivité, bruit d'appariement et autres contributions au bruit de jet subsonique*. PhD thesis, Ecole Centrale de Lyon, 2006. 71, 72

[32] N.J. Georgiadis and W.A. Yoder, D.A., Engblom. Evaluation of modified two equation turbulence models for jet flow predictions. In *44th AIAA Aerospace Sciences Meeting and Exhibit*, number January, pages 1–16, 2006. 42, 125

[33] M. Harper-Bourne and M.J. Fisher. The noise from shock waves in supersonic jets. In *AGARD Noise Mech. 13 p (SEE N74-22640 14-02); International Organization*, 1973. 29, 78, 80

[34] W.D. Hayes. Kinematic wave theory. *Proceedings of the Royal Society of London. Series A. Mathematical and physical sciences*, 320(1541):209–226, 1970. 93

[35] M.S. Howe. *Acoustics of fluid-structure interactions*. 1998. 102

[36] J. Huber, A.A. Sylla, V. Fleury, J. Bulté, K. Britchford, E. Laurendeau, and D.F. Long. Understanding and reduction of cruise jet noise at model full scale. *AIAA Aeroacoustics Conference*, (May), 2009. 36

[37] W.P. Jones and B.E. Launder. The prediction of laminarization with a two-equation model of turbulence. *International Journal of Heat and Mass Transfer*, 15:301–314, 1972. 42, 43, 135

[38] A. Khavaran, E.A. Krejsa, and C.M. Kim. Computation of supersonic jet mixing noise for an axisymmetric CD nozzle using k-e turbulence model. *AIAA Journal*, 1992. 31

[39] M.T. Landahl and M.T. Mollo-Christense. *Turbulence and random processes in fluid mechanics*. 1992. 40

[40] J.C. Lau. *PhD Thesis*. PhD thesis, University of Southampton, 1971. 22

[41] J.C. Lau, P.J. Morris, and M.J. Fisher. Measurements in subsonic and supersonic free jets using a laser velocimeter. *Journal of Fluid Mechanics*, 93(1):1–27, 1979. 22, 71, 72, 73, 74, 76

[42] M. Lazareff and L. Cambier. elsA's Theoretical manual. Technical report, Onera, 2004. 44, 47

[43] S.K. Lele. Phased array models of shock-cell noise sources. In *AIAA Aeroacoustics Conference*, number May, pages 23–25, 2005. 50

[44] M.J. Lighthill. On sound generated aerodynamically-I. General theory. In *Proceedings of the Royal Society of London A*, pages 564–587, 1952. 26

[45] G.M. Lilley. Fourth Monthly Progress Report on contract F-33615-71-C-1663. Appendix: generation of sound in a mixing region. Technical report, Lockheed Aircraft Company, Marietta, Ga., 1971. 91

[46] G.M. Lilley. Jet noise classical theory and experiments. In *Aeroacoustics of flight vehicles: Thoery and Practice*, chapter 4, pages 211–289. 1995. 22

[47] V.G. Mengle. The effect of nozzle-to-wing gulley height on jet flow attachment to the wing and jet-flap interaction noise. In *17th AIAA/CEAS Aeroacoustics Conference*, number June, Portland, Oregon, USA, 2011. 125

[48] F.R. Menter. Improved two-equation k-omega turbulence models for aerodynamic flows. Technical report, 1992. 43, 135

[49] F.R. Menter. Influence of freestream values on k-omega turbulence model predictions. *AIAA Journal*, 30(6), 1992. 42

[50] S.A.E Miller. *The prediction of broadband shock-associated noise using Reynolds-averaged Navier-Stokes solutions.* PhD thesis, 2009. 31, 56

[51] S.A.E Miller. The scaling of broadband shock-associated noise with increasing temperature. In *18th AIAA/CEAS Aeroacoustics Conference*, Colorado Springs, CO, USA, 2012. 31, 124

[52] S.A.E Miller and P.J. Morris. The prediction of broadband shock-associated noise from dualstream and rectangular jets using RANS CFD. In *16th AIAA/CEAS Aeroacoustics Conference*, 2010. 31, 49, 56

[53] S.A.E Miller and P.J. Morris. The prediction of broadband shock-associated noise including propagation effects. In *17th AIAA/CEAS Aeroacoustics Conference*, number June, pages 05 – 08, 2011. 31, 56, 90

[54] P.J. Morris. A note on the effect of forward flight on shock spacing in circular jets. *Journal of Sound and Vibration*, 121:175–177, 1988. 34, 112

[55] P.J. Morris and F. Farassat. On the acoustic analogy and alternative theories for jet noise prediction. *AIAA Journal*, 4(40):671–680, 2002. 15, 31

[56] P.J. Morris and S.A.E Miller. The prediction of broadband shock-associated noise using RANS CFD. In *15th AIAA Aeroacoustics Conference*, 2009. 15, 49, 56, 57, 123

[57] P.J. Morris and S.A.E Miller. Prediction of broadband shock-associated noise using Reynolds-Averaged Navier-Stokes computational fluid dynamics. *AIAA Journal*, 48(12), 2010. 49, 56, 57

[58] P.J. Morris and K.B.M.Q. Zaman. Velocity measurements in jets with application to noise source modeling. *Journal of Sound and Vibration*, October 2009. 71

[59] T.D. Norum and M.C. Brown. Simulated high speed flight effects on supersonic jet noise. In *15th AIAA Aeroacoustics Conference*, pages 1–10, Long Beach, California, 1993. 34, 35, 114

[60] T.D. Norum and J.M. Seiner. Measurements of mean static pressure and far-field acoustics of shock-containing supersonic jets. *NASA Technical Memorandum - 84521*, 1982. 30, 68

[61] T.D. Norum and J.G. Shearin. Shock structure and noise of supersonic jets in simulated flight to Mach 0.4. Technical Report February, NASA, 1988. 34, 35

[62] D.C. Pack. A note on Prandtl's formula for the wave-length of a supersonic gas jet. *The Quarterly Journal of Mechanics and Applied Mathematics*, 3(2):173–181, 1950. 25

[63] O.M. Phillips. On the generation of sound by supersonic turbulent shear layers. *Journal of Fluid Mechanics*, 9(1):1–28, 1960. 49

[64] S.Z. Pinckney. A short static-pressure probe design for supersonic flow. Technical report, 1975. 68

[65] A. Powell. On the mechanism of choked jet noise. *Proceedings of the Physical Society*, 66(12):1039–1056, 1953. 27

[66] L. Prandtl. No Title. *Phys. Zeits.*, 5:599, 1904. 24

[67] G. Raman. Advances in understanding supersonic jet screech: review and perspective. Technical report, NASA. 27

[68] G. Raman. Cessation of screech in underexpanded jets. *Journal of Fluid Mechanics1*, 336:69–90, 1997. 27

[69] G. Raman. Supersonic jet screech: half-century from Powell to the present. *Journal of Sound and Vibration*, 225(3):543–571, 1999. 28

[70] L. Rayleigh. On the stability, or instability, of certain fluid motions. In *Proceedings of the London Mathematical Society*, 1879. 24

[71] H.S. Ribner. Reflection, transmission, and amplification of sound by a moving medium. *Journal of Acoustic Society of America*, 29(4):435–441, 1957. 33

[72] S.W. Rienstra and A. Hirschberg. *An introduction to acoustics*. Number April. 2011. 27, 93

[73] P.L. Roe. Approximate Riemann solvers, parameter vectors and difference schemes. *Journal of Computational Physics*, 43(2):357–372, 1981. 45

[74] L. K. Schubert. Numerical study of sound refraction by a jet flow. II. Wave acoustics. *Journal of Acoustic Society of America*, 51(September):447–463, 1971. 93

[75] J.M. Seiner and T.D. Norum. Aerodynamic aspects of shock containing jet plumes. In *AIAA 6th Aeroacoustics Conference*, 1980. 31, 78

[76] H. Shen, J. Luedke, R. Avancha, and A. Gupta. An investigation of shock-cell noise from model engine nozzles. In *14th AIAA/CEAS Aeroacoustics Conference, Vancouver BC , AIAA Paper 2008-2839, May*, 2008. 31

[77] P.R. Spalart. Strategies for turbulence modelling and simulations. *International Journal of Heat and Fluid Flow*, 21:252–263, 2000. 40

[78] C.K.W. Tam. On the noise of a nearly ideally expanded supersonic jet. *Journal of Fluid Mechanics*, 51:69–95, 1972. 25, 31

[79] C.K.W. Tam. Stochastic model theory of broadband shock associated noise from supersonic jets. *Journal of Sound and Vibration*, 116:265–302, 1987. 31, 50

[80] C.K.W. Tam. Broadband shock-associated noise of moderatelty imperfectly expanded supersonic jets. *Journal of Sound and Vibration*, 140:55–71, 1990. 31

[81] C.K.W. Tam. Broadband shock-associated noise from supersonic jets in flight. *Journal of Sound and Vibration*, 151:131–147, 1991. 34, 35

[82] C.K.W. Tam. Supersonic jet noise. *Annual Review of Fluid Mechanics*, 27, 1995. 27

[83] C.K.W. Tam and L. Auriault. Mean flow refraction effects on sound radiated from localized sources in a jet. *Journal of Fluid Mechanics*, 370:149–174, 1998. 34, 90, 100

[84] C.K.W. Tam and L. Auriault. Jet mixing noise from fine-scale turbulence. *AIAA Journal*, 37(2):145–153, 1999. 56, 125

[85] C.K.W. Tam and K.C. Chen. A statistical model of turbulence in two-dimensional mixing layers. *Journal of Fluid Mechanics*, 92, 1979. 26

[86] C.K.W. Tam and P. Chen. Turbulence mixing noise from supersonic jets. *AIAA Journal*, 32(9):174–180, 1994. 27

[87] C.K.W. Tam, M. Golebiowski, and J.M. Seiner. On the two components of turbulent mixing noise from supersonic jets. In *2nd AIAA/CEAS Aeroacoustics Conference*, 1996. 25, 27

[88] C.K.W. Tam, J.A. Jackson, and J.M. Seiner. A multiple-scales model of the shock-cell structure of imperfectly expanded supersonic jets. *Journal of Fluid Mechanics*, 153:123–149, 1985. 25

[89] C.K.W. Tam and N.N. Pastouchenko. Broadband shock-cell noise from dual stream jets. *AIAA Aeroacoustics Conference*, July 2008. 89

[90] C.K.W. Tam, N.N. Pastouchenko, and K. Viswanathan. Broadband shock-cell noise from dual stream jets. *Journal of Sound and Vibration*, 324(3-5):861–891, July 2009. 36, 89

[91] C.K.W. Tam and H.K. Tanna. Shock associated noise of supersonic jets from convergent-divergent nozzles. *Journal of Sound and Vibration*, 81:337–358, 1982. 26, 31

[92] C.K.W. Tam, K. Viswanathan, K.K. Ahuja, and J. Panda. The sources of jet noise: experimental evidence. *Journal of Fluid Mechanics*, 615:253, November 2008. 25, 27, 28

[93] G.D. Van Albada, B. Van Leer, and W.W. Roberts. A comparative study of computational methods in cosmic gas dynamics. *Astron. Astrophysics*, 108:76–84, 1982. 47

[94] D. Wilcox. Reassessment of the scale-determining equation for advanced turbulence models. *AIAA Paper*, 26(11):1299–1310, 1988. 42, 135

[95] D.C. Wilcox. *Turbulence modeling for CFD*. DCW Industries, 3rd edition, 2010. 42

[96] D.W. Wundrow and A. Khavaran. On the applicability of high-frequency approximations to Lilley's equation. *Journal of Sound and Vibration*, 272:793–830, 2004. 91

Appendix A

Turbulence models

A.1 Constants for turbulence models

The $k-\omega-$BSL model is a mix between two turbulence models, namely $k-\omega$ and $k-\varepsilon$. The constants of the $k-\omega-$BSL model are obtained by mixing the constants of those two models, using a blending function. Let ϕ_1 be a constant for the original $k-\omega$ model, and ϕ_2 a constant for the the $k-\varepsilon$ model. The corresponding constant for the BSL model ϕ is obtained by

$$\phi = F_1\phi_1 + (1-F_1)\phi_2 \tag{A.1}$$

where F_1 is a blending function, its expression may be found in [48].

For practical applications, the constants associated with the original $k-\omega$ model are given by [94]

$$\begin{array}{ccc} \sigma_{k1} = 0.5, & \sigma_{\omega 1}, = 0.5 & \beta_1 = 0.0750 \\ \beta^* = 0.09, & \kappa = 0.41, & \gamma_1 = \beta_1/\beta^* - \sigma_{\omega 1}\kappa^2/\sqrt{\beta^*} \end{array} \tag{A.2}$$

The constants used in the $k-\varepsilon$ model are from Jones-Launder [37]

$$\begin{array}{ccc} \sigma_{k2} = 1.0, & \sigma_{\omega 2} = 0.856, & \beta_2 = 0.0828 \\ \beta^* = 0.09, & \kappa = 0.41, & \gamma_2 = \beta_2/\beta^* - \sigma_{\omega 2}\kappa^2/\sqrt{\beta^*} \end{array} \tag{A.3}$$

A blending function F_2 is also used in the $k-\omega-$SST model. It connects the expression of ν_t in the boundary layer to the expression for a free shear flow

$$F_2 = \tanh(arg^2), \quad arg = \max\left(2\frac{\sqrt{k}}{0.09\omega y}, \frac{400\nu}{y^2\omega}\right), \quad \nu_t = \frac{a_1 k}{\max(a_1\omega, \Omega F_2)} \tag{A.4}$$

The constants to be used for the $k-\omega$ model in the boundary layer are

$$\begin{array}{ccc} \sigma_{k1} = 0.85, & \sigma_{\omega 1} = 0.65, & \beta_1 = 0.0750 \\ \beta^* = 0.09, & \kappa = 0.41, & \gamma_1 = \beta_1/\beta^* - \sigma_{\omega 1}\kappa^2/\sqrt{\beta^*} \end{array} \tag{A.5}$$

A.2 Conservative form of the RANS equations

The conservative form of the RANS equations is

$$\frac{\partial}{\partial t}\int_\Omega \boldsymbol{W} d\Omega + \int_{\partial\Omega} \boldsymbol{F}_c \cdot d\boldsymbol{S} + \int_{\partial\Omega} \boldsymbol{F}_d \cdot d\boldsymbol{S} = 0 \tag{A.6}$$

Ω is the CFD domain and $\partial\Omega$ is boundary. The state vector $\boldsymbol{W}$ is given by

$$\boldsymbol{W} = \begin{pmatrix} \overline{\rho} \\ \overline{\rho}\tilde{v}_1 \\ \overline{\rho}\tilde{v}_2 \\ \overline{\rho}\tilde{v}_3 \\ \overline{\rho}E \end{pmatrix} \tag{A.7}$$

where the total energy is given by $E = \overline{\rho}\left(\tilde{e} + \frac{\tilde{v}_i\tilde{v}_i}{2}\right) + \frac{\overline{\rho v_i'' v_i''}}{2}$. The convective flux matrix $\boldsymbol{F}_c$ expresses as

$$\boldsymbol{F}_c = \begin{pmatrix} \overline{\rho}\tilde{v}_1 & \overline{\rho}\tilde{v}_2 & \overline{\rho}\tilde{v}_3 \\ \overline{\rho}\tilde{v}_1^2 + P & \overline{\rho}\tilde{v}_1\tilde{v}_2 & \overline{\rho}\tilde{v}_1\tilde{v}_3 \\ \overline{\rho}\tilde{v}_1\tilde{v}_2 & \overline{\rho}\tilde{v}_2^2 + P & \overline{\rho}\tilde{v}_2\tilde{v}_3 \\ \overline{\rho}\tilde{v}_1\tilde{v}_3 & \overline{\rho}\tilde{v}_2\tilde{v}_3 & \overline{\rho}\tilde{v}_3^2 + P \end{pmatrix} \tag{A.8}$$

and the diffusive flux is given by

$$\boldsymbol{F}_d = \begin{pmatrix} 0 & 0 & 0 \\ \tau_{11} & \tau_{12} & \tau_{13} \\ \tau_{21} & \tau_{22} & \tau_{23} \\ \tau_{31} & \tau_{32} & \tau_{33} \end{pmatrix} \tag{A.9}$$

Appendix B

Calculation of the vector Green's function

B.1 Calculation of $\Pi_n(\boldsymbol{x},\boldsymbol{y},\omega)$ without mean flow

Without mean flow, $\Pi_n(\boldsymbol{x},\boldsymbol{y},\omega)$ is obtained by deriving the free field scalar Green's function, namely

$$\Pi_n(\boldsymbol{x},\boldsymbol{y},\omega)=\frac{\partial}{\partial y_n}\left(\frac{e^{-i\omega\frac{|\boldsymbol{x}-\boldsymbol{y}|}{c_\infty}}}{4\pi c_\infty^2|\boldsymbol{x}-\boldsymbol{y}|}\right) \tag{B.1}$$

Two functions are introduced,

$$\begin{cases} u(\boldsymbol{y})=e^{-i\omega|\boldsymbol{x}-\boldsymbol{y}|/c_\infty} \\ v(\boldsymbol{y})=4\pi c_\infty^2|\boldsymbol{x}-\boldsymbol{y}| \end{cases} \tag{B.2}$$

Then,

$$\Pi_n(\boldsymbol{x},\boldsymbol{y},\omega)=\frac{\partial}{\partial y_n}\left(\frac{u}{v}\right)=\frac{\frac{\partial u}{\partial y_n}v-\frac{\partial v}{\partial y_n}u}{v^2} \tag{B.3}$$

The derivation of $\partial u/\partial y_n$ gives,

$$\begin{aligned}\frac{\partial u}{\partial y_n}&=\frac{\partial}{\partial y_n}\left(e^{-i\omega|\boldsymbol{x}-\boldsymbol{y}|/c_\infty}\right)\\ &=\frac{\partial}{\partial y_n}\left(-\frac{i\omega}{c_\infty}|\boldsymbol{x}-\boldsymbol{y}|\right)e^{-i\omega|\boldsymbol{x}-\boldsymbol{y}|/c_\infty}\\ \frac{\partial u}{\partial y_n}&=-\frac{i\omega}{c_\infty}\frac{y_n-x_n}{|\boldsymbol{x}-\boldsymbol{y}|}e^{-i\omega|\boldsymbol{x}-\boldsymbol{y}|/c_\infty}\end{aligned} \tag{B.4}$$

For $\partial v/\partial y_n$,

$$\frac{\partial v}{\partial y_n}=\frac{\partial}{\partial y_n}(4\pi c_\infty^2|\boldsymbol{x}-\boldsymbol{y}|)=4\pi c_\infty^2\frac{y_n-x_n}{|\boldsymbol{x}-\boldsymbol{y}|} \tag{B.5}$$

Reverting to B.3 :

$$\begin{aligned}
\Pi_n(\boldsymbol{x},\boldsymbol{y},\omega) &= \frac{-\frac{i\omega}{c_\infty}\frac{y_n-x_n}{|\boldsymbol{x}-\boldsymbol{y}|}e^{-i\omega|\boldsymbol{x}-\boldsymbol{y}|/c_\infty}\times 4\pi c_\infty^2|\boldsymbol{x}-\boldsymbol{y}| - e^{-i\omega|\boldsymbol{x}-\boldsymbol{y}|/c_\infty}\times 4\pi c_\infty^2\frac{y_n-x_n}{|\boldsymbol{x}-\boldsymbol{y}|}}{16\pi^2c_\infty^4|\boldsymbol{x}-\boldsymbol{y}|^2} \\
&= -\frac{\frac{i\omega}{c_\infty}\frac{y_n-x_n}{|\boldsymbol{x}-\boldsymbol{y}|}e^{-i\omega|\boldsymbol{x}-\boldsymbol{y}|/c_\infty}\times|\boldsymbol{x}-\boldsymbol{y}| + e^{-i\omega|\boldsymbol{x}-\boldsymbol{y}|/c_\infty}\times\frac{y_n-x_n}{|\boldsymbol{x}-\boldsymbol{y}|}}{4\pi c_\infty^2|\boldsymbol{x}-\boldsymbol{y}|^2} \qquad \text{(B.6)} \\
\Pi_n(\boldsymbol{x},\boldsymbol{y},\omega) &= -\frac{e^{-i\omega|\boldsymbol{x}-\boldsymbol{y}|/c_\infty}}{4\pi c_\infty^2}\times(y_n-x_n)\times\frac{\frac{1}{|\boldsymbol{x}-\boldsymbol{y}|}+\frac{i\omega}{c_\infty}}{|\boldsymbol{x}-\boldsymbol{y}|^2}
\end{aligned}$$

This expression is simplified using the far field hypothesis, detailed in the main chapter corresponding to this appendix. An asymptotic expansion of $|\boldsymbol{x}-\boldsymbol{y}|^2$ at the lowest order gives,

$$\begin{aligned}
|\boldsymbol{x}-\boldsymbol{y}|^{-2} &= (x_1^2+x_2^2+x_3^2+y_1^2+y_2^2+y_3^2-2(x_1y_1+x_2y_2+x_3y_3))^{-1} \\
&= |\boldsymbol{x}|^{-2}\left(1+\frac{|\boldsymbol{y}|^2}{|\boldsymbol{x}|^2}-2\frac{\boldsymbol{x}.\boldsymbol{y}}{|\boldsymbol{x}|^2}\right)^{-1} \qquad \text{(B.7)} \\
|\boldsymbol{x}-\boldsymbol{y}|^{-2} &= |\boldsymbol{x}|^{-2}+o(1)
\end{aligned}$$

Similarly, for $(y_n-x_n)(1/|\boldsymbol{x}-\boldsymbol{y}|+i\omega/c_\infty)$,

$$\begin{aligned}
(y_n-x_n)(1/|\boldsymbol{x}-\boldsymbol{y}|+i\omega/c_\infty) &= x_n\left(\frac{y_n}{x_n}-1\right)\left(\frac{i\omega}{c_\infty}+|\boldsymbol{x}-\boldsymbol{y}|^{-1}\right) \\
&= -x_n\left[\frac{i\omega}{c_\infty}+\left\{|\boldsymbol{x}|^2\left(1+\frac{|\boldsymbol{y}|^2}{|\boldsymbol{x}|^2}-2\frac{\boldsymbol{x}.\boldsymbol{y}}{|\boldsymbol{x}|^2}\right)\right\}^{-1/2}\right]+o(1) \\
&= -x_n\left[\frac{i\omega}{c_\infty}+|\boldsymbol{x}|^{-1}\left(1+\frac{|\boldsymbol{y}|^2}{|\boldsymbol{x}|^2}-2\frac{\boldsymbol{x}.\boldsymbol{y}}{|\boldsymbol{x}|^2}\right)^{-1/2}\right]+o(1) \\
(y_n-x_n)(1/|\boldsymbol{x}-\boldsymbol{y}|+i\omega/c_\infty) &= -x_n\left[\frac{i\omega}{c_\infty}+|\boldsymbol{x}|^{-1}\right]+o(1)
\end{aligned} \qquad \text{(B.8)}$$

$\Pi_n(\boldsymbol{x},\boldsymbol{y},\omega)$ is now given by,

$$\begin{aligned}
\Pi_n(\boldsymbol{x},\boldsymbol{y},\omega) &= -\frac{e^{-i\omega|\boldsymbol{x}-\boldsymbol{y}|/c_\infty}}{4\pi c_\infty^2}\times(|\boldsymbol{x}|^{-2}+o(1))\times\left(-x_n\left[\frac{i\omega}{c_\infty}+|\boldsymbol{x}|^{-1}\right]+o(1)\right) \\
&= \frac{e^{-i\omega|\boldsymbol{x}-\boldsymbol{y}|/c_\infty}}{4\pi c_\infty^2}|\boldsymbol{x}|^{-2}\times x_n\left[\frac{i\omega}{c_\infty}+|\boldsymbol{x}|^{-1}\right]+o(1) \qquad \text{(B.9)} \\
\Pi_n(\boldsymbol{x},\boldsymbol{y},\omega) &= \frac{e^{-i\omega|\boldsymbol{x}-\boldsymbol{y}|/c_\infty}}{4\pi c_\infty^2}\frac{i\omega}{c_\infty}\frac{x_n}{|\boldsymbol{x}|^2}+o(1)
\end{aligned}$$

Finally,

$$\Pi_n(\boldsymbol{x},\boldsymbol{y},\omega) \approx \frac{e^{-i\omega|\boldsymbol{x}-\boldsymbol{y}|/c_\infty}}{4\pi c_\infty^2}\frac{i\omega}{c_\infty}\frac{x_n}{|\boldsymbol{x}|^2} \tag{B.10}$$

B.2 Calculation of $\Pi_m(\boldsymbol{x}, \boldsymbol{y}+\boldsymbol{\eta}, \omega)$

According to the previous part, $\Pi_m(\boldsymbol{x},\boldsymbol{y}+\boldsymbol{\eta},\omega)$ is given by,

$$\Pi_m(\boldsymbol{x},\boldsymbol{y}+\boldsymbol{\eta},\omega) = \frac{e^{-i\omega|\boldsymbol{x}-(\boldsymbol{y}+\boldsymbol{\eta})|/c_\infty}}{4\pi c_\infty^2}\frac{i\omega}{c_\infty}\frac{x_m}{|\boldsymbol{x}|^2} \tag{B.11}$$

$|\boldsymbol{x} - (\boldsymbol{y} + \boldsymbol{\eta})|$ is asymptotically expanded at the lowest order in $|\boldsymbol{y}|/|\boldsymbol{x}|$,

$$\begin{aligned} |\boldsymbol{x} - (\boldsymbol{y} + \boldsymbol{\eta})|^2 &= |\boldsymbol{x} - \boldsymbol{y}|^2 + |\boldsymbol{\eta}|^2 - 2(\boldsymbol{x} - \boldsymbol{y}).\boldsymbol{\eta} \\ &= |\boldsymbol{x} - \boldsymbol{y}|^2 \left(1 + \frac{|\boldsymbol{\eta}|^2}{|\boldsymbol{x} - \boldsymbol{y}|^2} - 2\frac{(\boldsymbol{x} - \boldsymbol{y}).\boldsymbol{\eta}}{|\boldsymbol{x} - \boldsymbol{y}|^2}\right) \end{aligned} \tag{B.12}$$

Since $\boldsymbol{\eta} = \boldsymbol{y_2} - \boldsymbol{y_1}$, $|\boldsymbol{\eta}^2|/|\boldsymbol{x} - \boldsymbol{y}|^2 = o(1)$:

$$|\boldsymbol{x} - (\boldsymbol{y} + \boldsymbol{\eta})|^2 = |\boldsymbol{x} - \boldsymbol{y}|^2 \left(1 - 2\frac{\boldsymbol{x}.\boldsymbol{\eta}}{|\boldsymbol{x} - \boldsymbol{y}|^2}\right) + o(1) \tag{B.13}$$

It follows that,

$$|\boldsymbol{x} - (\boldsymbol{y} + \boldsymbol{\eta})| = |\boldsymbol{x} - \boldsymbol{y}| \left(1 - \frac{\boldsymbol{x}.\boldsymbol{\eta}}{|\boldsymbol{x} - \boldsymbol{y}|^2}\right) + o(1) \tag{B.14}$$

$$\Pi_m(\boldsymbol{x}, \boldsymbol{y} + \boldsymbol{\eta}, \omega) = \frac{e^{-i\frac{\omega}{c_\infty}|\boldsymbol{x} - \boldsymbol{y}|} \times e^{i\frac{\omega}{c_\infty}\frac{\boldsymbol{x}.\boldsymbol{\eta}}{|\boldsymbol{x} - \boldsymbol{y}|}}}{4\pi c_\infty^2} \frac{i\omega}{c_\infty} \frac{x_m}{|\boldsymbol{x}|^2} \tag{B.15}$$

Finally,

$$\begin{aligned} \Pi_m(\boldsymbol{x}, \boldsymbol{y} + \boldsymbol{\eta}, \omega) &= \Pi_m(\boldsymbol{x}, \boldsymbol{y}, \omega) e^{i\frac{\omega}{c_\infty}\frac{\boldsymbol{x}.\boldsymbol{\eta}}{|\boldsymbol{x} - \boldsymbol{y}|}} \\ \Pi_m^*(\boldsymbol{x}, \boldsymbol{y} + \boldsymbol{\eta}, -\omega) &= \Pi_m^*(\boldsymbol{x}, \boldsymbol{y}, -\omega) e^{i\frac{\omega}{c_\infty}\frac{\boldsymbol{x}.\boldsymbol{\eta}}{|\boldsymbol{x} - \boldsymbol{y}|}} \end{aligned} \tag{B.16}$$

B.3 Derivation of Π_n with mean flow

This appendix details the calculation of Π_n when mean flow effects are considered. The acoustic pressure is a solution to Lilley's equation, so that,

$$\begin{aligned} p'(\boldsymbol{x}, \omega) &= \overline{\rho}\,\overline{c}^2 \int_{\boldsymbol{y}} g_L(\boldsymbol{x}, \boldsymbol{y}, \omega) \Gamma(\boldsymbol{y}, \omega) d\boldsymbol{y} \\ p'(\boldsymbol{x}, \omega) &= -\overline{\rho}\,\overline{c}^2 \int_{\boldsymbol{y}} g_L(\boldsymbol{x}, \boldsymbol{y}, \omega) \left[\left(-i\omega + \overline{v}_1 \frac{\partial}{\partial y_1}\right) \frac{\partial f_i}{\partial y_i} - 2\frac{\partial \overline{v}_i}{\partial y_i}\frac{\partial f_i}{\partial y_1}\right] d\boldsymbol{y} \end{aligned} \tag{B.17}$$

Expanding the summation over i,

$$\begin{aligned} p'(\boldsymbol{x}, \omega) = -\overline{\rho}\,\overline{c}^2 \int_{\boldsymbol{y}} g_L(\boldsymbol{x}, \boldsymbol{y}, \omega) &\Bigg[\underbrace{\left(-i\omega + \overline{v}_1 \frac{\partial}{\partial y_1}\right) \frac{\partial f_1}{\partial y_1}}_{A} + \underbrace{\left(-i\omega + \overline{v}_1 \frac{\partial}{\partial y_1}\right) \frac{\partial f_2}{\partial y_2}}_{B} \\ &+ \underbrace{\left(-i\omega + \overline{v}_1 \frac{\partial}{\partial y_1}\right) \frac{\partial f_3}{\partial y_3}}_{C} - 2\underbrace{\frac{\partial \overline{v}_1}{\partial y_1}\frac{\partial f_1}{\partial y_1}}_{=0} - 2\underbrace{\frac{\partial \overline{v}_1}{\partial y_2}\frac{\partial f_2}{\partial y_1}}_{D} - 2\underbrace{\frac{\partial \overline{v}_1}{\partial y_3}\frac{\partial f_3}{\partial y_1}}_{E} \Bigg] d\boldsymbol{y} \end{aligned} \tag{B.18}$$

Using integration by parts for terms A to E, the spatial differentiation operator may be applied to the Green's function instead of the source term. For instance, for term A this leads to,

$$\begin{aligned}
A &= \int_{\boldsymbol{y}} g_L(\boldsymbol{x},\boldsymbol{y},\omega)\left(-i\omega+\overline{v}_1\frac{\partial}{\partial y_1}\right)\frac{\partial f_1}{\partial y_1}d\boldsymbol{y} \\
&= \int_{y_2,y_3}\left[\int_{y_1} g_L(\boldsymbol{x},\boldsymbol{y},\omega)\left(-i\omega+\overline{v}_1\frac{\partial}{\partial y_1}\right)\frac{\partial f_1}{\partial y_1}dy_1\right]dy_2\,dy_3 \\
A &= \int_{y_2,y_3}\left\{\left[g_L(\boldsymbol{x},\boldsymbol{y},\omega)(-i\omega)f_1+g_L(\boldsymbol{x},\boldsymbol{y},\omega)\overline{v}_1\frac{\partial f_1}{\partial y_1}\right]_{y_1\to-\infty}^{y_1\to+\infty}\right. \\
&\quad \left.-\int_{y_1}\left[(-i\omega)f_1\frac{\partial g_L}{\partial y_1}+\overline{v}_1\frac{\partial f_1}{\partial y_1}\frac{\partial g_L}{\partial y_1}\right]dy_1\right\}dy_2\,dy_3
\end{aligned} \tag{B.19}$$

The first term between square brackets is null because there are no source at infinity. Then,

$$\begin{aligned}
A &= \int_{\boldsymbol{y}} i\omega\frac{\partial g_L}{\partial y_1}f_1 d\boldsymbol{y}-\int_{\boldsymbol{y}}\overline{v}_1\frac{\partial f_1}{\partial y_1}\frac{\partial g_L}{\partial y_1}d\boldsymbol{y} \\
A &= \int_{\boldsymbol{y}} i\omega\frac{\partial g_L}{\partial y_1}f_1 d\boldsymbol{y}-\int_{y_2,y_3}\left\{\left[\overline{v}_1 f_1\frac{\partial g_L}{\partial y_1}\right]_{y_1\to-\infty}^{y_1\to+\infty}-\int_{y_1}\frac{\partial}{\partial y_1}\left(\overline{v}_1\frac{\partial g_L}{\partial y_1}\right)f_1 dy_1\right\}
\end{aligned} \tag{B.20}$$

Again, the term between square brackets is null. Since $\overline{v}_1$ is not a function of y_1, A reduces to,

$$A = \int_{\boldsymbol{y}}\left(i\omega\frac{\partial g_L}{\partial y_1}+\overline{v}_1\frac{\partial^2 g_L}{\partial y_1^2}\right)f_1 dy_1 \tag{B.21}$$

Following similar steps, B is calculated,

$$\begin{aligned}
B &= \int_{\boldsymbol{y}} g_L(\boldsymbol{x},\boldsymbol{y},\omega)\left(-i\omega+\overline{v}_1\frac{\partial}{\partial y_1}\right)\frac{\partial f_2}{\partial y_2}d\boldsymbol{y} \\
&= \int_{\boldsymbol{y}}\left(-i\omega\frac{\partial f_2}{\partial y_2}g_L(\boldsymbol{x},\boldsymbol{y},\omega)+\overline{v}_1\frac{\partial^2 f_2}{\partial y_1\partial y_2}g_L(\boldsymbol{x},\boldsymbol{y},\omega)\right)d\boldsymbol{y} \\
&= \int_{y_1,y_3}\left\{-\left[i\omega f_2 g_L(\boldsymbol{x},\boldsymbol{y},\omega)\right]_{y_2\to-\infty}^{y_2\to+\infty}+\int_{y_2}\left(i\omega f_2\frac{\partial g_L}{\partial y_2}\right)dy_2\right\}dy_1 dy_3 \\
&+ \int_{y_1,y_3}\left[\overline{v}_1\frac{\partial f_2}{\partial y_2}g_L(\boldsymbol{x},\boldsymbol{y},\omega)\right]_{y_2\to-\infty}^{y_2\to+\infty}dy_1\,dy_3-\int_{\boldsymbol{y}}\overline{v}_1\frac{\partial f_2}{\partial y_2}\frac{\partial g_L}{\partial y_1}d\boldsymbol{y} \\
&= \int_{\boldsymbol{y}} i\omega\frac{\partial g_L}{\partial y_2}f_2 d\boldsymbol{y}-\int_{y_1,y_3}\left[f_2\overline{v}_1\frac{\partial g_L}{\partial y_1}\right]_{y_2\to-\infty}^{y_2\to+\infty}dy_1\,dy_3+\int_{\boldsymbol{y}}\overline{v}_1\frac{\partial^2 g_L}{\partial y_2\partial y_1}f_2 d\boldsymbol{y} \\
B &= \int_{\boldsymbol{y}}\left(i\omega\frac{\partial g_L}{\partial y_2}+\overline{v}_1\frac{\partial^2 g_L}{\partial y_1\partial y_2}\right)f_2 d\boldsymbol{y}
\end{aligned} \tag{B.22}$$

The same steps applied to C give,

$$\begin{aligned}
C &= \int_{\boldsymbol{y}} g_L(\boldsymbol{x},\boldsymbol{y},\omega)\left(-i\omega+\overline{v}_1\frac{\partial}{\partial y_1}\right)\frac{\partial f_3}{\partial y_3}d\boldsymbol{y} \\
&= \int_{\boldsymbol{y}} i\omega\frac{\partial g_L}{\partial y_3}f_3 d\boldsymbol{y}-\int_{\boldsymbol{y}}\overline{v}_1\frac{\partial f_3}{\partial y_3}\frac{\partial g_L}{\partial y_1}d\boldsymbol{y} \\
C &= \int_{\boldsymbol{y}}\left(i\omega\frac{\partial g_L}{\partial y_3}+\overline{v}_1\frac{\partial^2 g_L}{\partial y_3\partial y_1}\right)f_3 d\boldsymbol{y}
\end{aligned} \tag{B.23}$$

D is faster to evaluate,

$$\begin{aligned} D &= \int_{\boldsymbol{y}} \frac{\partial \overline{v}_1}{\partial y_2}\frac{\partial f_2}{\partial y_1} g_L(\boldsymbol{x},\boldsymbol{y},\omega) d\boldsymbol{y} \\ &= -\int_{\boldsymbol{y}} \frac{\partial}{\partial y_1}\left(\frac{\partial \overline{v}_1}{\partial y_2} g_L\right) f_2 d\boldsymbol{y} \\ D &= -\int_{\boldsymbol{y}} \frac{\partial g_L}{\partial y_1}\frac{\partial \overline{v}_1}{\partial y_2} f_2 d\boldsymbol{y} \end{aligned} \tag{B.24}$$

E is similar to D,

$$\begin{aligned} E &= \int_{\boldsymbol{y}} \frac{\partial \overline{v}_1}{\partial y_3}\frac{\partial f_3}{\partial y_1} g_L(\boldsymbol{x},\boldsymbol{y},\omega) d\boldsymbol{y} \\ &= -\int_{\boldsymbol{y}} \frac{\partial}{\partial y_1}\left(\frac{\partial \overline{v}_1}{\partial y_3} g_L\right) f_3 d\boldsymbol{y} \\ E &= -\int_{\boldsymbol{y}} \frac{\partial g_L}{\partial y_1}\frac{\partial \overline{v}_1}{\partial y_3} f_3 d\boldsymbol{y} \end{aligned} \tag{B.25}$$

Injecting the new expressions of terms A to E into $p'(\boldsymbol{x},\omega)$ gives,

$$\begin{aligned} p'(\boldsymbol{x},\omega) = \overline{\rho}\,\overline{c}^2 \int_{\boldsymbol{y}} \Bigg\{ &-\left(i\omega\frac{\partial g_L}{\partial y_1} + \overline{v}_1 \frac{\partial^2 g_L}{\partial y_1^2}\right) f_1 \\ &-\left(i\omega\frac{\partial g_L}{\partial y_2} + 3\frac{\partial \overline{v}_1}{\partial y_2}\frac{\partial g_L}{\partial y_1} + \overline{v}_1 \frac{\partial^2 g_L}{\partial y_1 \partial y_2}\right) f_2 \\ &-\left(i\omega\frac{\partial g_L}{\partial y_3} + 3\frac{\partial \overline{v}_1}{\partial y_3}\frac{\partial g_L}{\partial y_1} + \overline{v}_1 \frac{\partial^2 g_L}{\partial y_1 \partial y_3}\right) f_3 \Bigg\} d\boldsymbol{y} \end{aligned} \tag{B.26}$$

Direct identification between this expression and the formal solution,

$$p'(\boldsymbol{x},\omega) = -\overline{\rho}\,\overline{c}^2 \iint \Pi_n(\boldsymbol{x},\boldsymbol{y},\omega) f_n(\boldsymbol{y},\omega) d\boldsymbol{y} \tag{B.27}$$

leads to the expression of Π_n,

$$\begin{aligned} \Pi_1(\boldsymbol{x},\boldsymbol{y},\omega) &= -\left(i\omega\frac{\partial g_L}{\partial y_1} + \overline{v}_1 \frac{\partial^2 g_L}{\partial y_1^2}\right) \\ \Pi_2(\boldsymbol{x},\boldsymbol{y},\omega) &= -\left(i\omega\frac{\partial g_L}{\partial y_2} + 3\frac{\partial \overline{v}_1}{\partial y_2}\frac{\partial g_L}{\partial y_1} + \overline{v}_1 \frac{\partial^2 g_L}{\partial y_1 \partial y_2}\right) \\ \Pi_3(\boldsymbol{x},\boldsymbol{y},\omega) &= -\left(i\omega\frac{\partial g_L}{\partial y_3} + 3\frac{\partial \overline{v}_1}{\partial y_3}\frac{\partial g_L}{\partial y_1} + \overline{v}_1 \frac{\partial^2 g_L}{\partial y_1 \partial y_3}\right) \end{aligned} \tag{B.28}$$

B.3.1 Differentiation of g_L using finite differences

The derivatives of g_L on the mesh are computed using finite differences at fourth order. The scheme is recalled for the first order derivatives,

$$\left(\frac{\partial g_L}{\partial y_1}\right)_{i,j,k} = \frac{1}{\Delta y_1}\left(\frac{-1}{12} g_{L_{i+2,j,k}} + \frac{2}{3} g_{L_{i+1,j,k}} - \frac{2}{3} g_{L_{i-1,j,k}} + \frac{1}{12} g_{L_{i-2,j,k}}\right) + \mathcal{O}(\Delta y_1^4) \tag{B.29}$$

$$\left(\frac{\partial g_L}{\partial y_2}\right)_{i,j,k} = \frac{1}{\Delta y_2}\left(\frac{-1}{12} g_{L_{i,j+2,k}} + \frac{2}{3} g_{L_{i,j+1,k}} - \frac{2}{3} g_{L_{i,j-1,k}} + \frac{1}{12} g_{L_{i,j-2,k}}\right) + \mathcal{O}(\Delta y_2^4) \tag{B.30}$$

$$\tag{B.31}$$

Higher order derivatives are computed accordingly.

B.4 Free field test case

In order to validate the computation of the scalar Green's function, a simple test case is considered: the free field radiation. In this case, the scalar Green's function is

$$g_L(\boldsymbol{x}, \boldsymbol{y}, \omega) = \frac{1}{i\omega c_\infty^2} \frac{e^{ikR}}{4\pi R} \tag{B.32}$$

where $k = \omega / c_\infty$ and $R = |\boldsymbol{x} - \boldsymbol{y}|$. Then the analytical derivatives of g_∞ are given by,

$$\begin{aligned} \frac{\partial g_0}{\partial y_i}(\boldsymbol{x}, \boldsymbol{y}, \omega) &= \frac{(y_i - x_i) e^{ikR} (kR + i)}{4\pi c_\infty^2 \omega R^3} \\ \frac{\partial^2 g_0}{\partial y_i^2}(\boldsymbol{x}, \boldsymbol{y}, \omega) &= \left[\frac{1}{2R^2} \left(k + \frac{ik^2 (x_1 - y_1)^2}{R} - \frac{k (x_1 - y_1)^2}{R^2} \right) \right. \\ &\qquad \left. - \frac{k (x_1 - y_1)^2}{R^4} - i \frac{\frac{3(x_1 - y_1)^2}{R^5} - \frac{1}{R^3}}{2} \right] \frac{e^{ikR}}{2\pi c_\infty^2 \omega} \\ \frac{\partial^2 g_0}{\partial y_i \partial y_j}(\boldsymbol{x}, \boldsymbol{y}, \omega) &= i (y_i - x_i)(y_j - x_j) \frac{k^2 R^2 + 3ikR - 3}{4\pi c_\infty^2 R^5 \omega} e^{ikR} \end{aligned} \tag{B.33}$$

Appendix C

Geometrical acoustics

C.1 Jacobian matrices for the geodesic elements

The geodesic elements satisfy the following system,

$$\left\{ \begin{aligned} \frac{d\boldsymbol{R}}{dt} &= \frac{\partial \boldsymbol{f}}{\partial \boldsymbol{x}}.\boldsymbol{R} + \frac{\partial \boldsymbol{f}}{\partial \boldsymbol{k}}.\boldsymbol{Q} \\ \frac{d\boldsymbol{Q}}{dt} &= \frac{\partial \boldsymbol{g}}{\partial \boldsymbol{x}}.\boldsymbol{R} + \frac{\partial \boldsymbol{g}}{\partial \boldsymbol{k}}.\boldsymbol{Q} \end{aligned} \right. \tag{C.1}$$

The corresponding Jacobian matrices in expanded and condensed form are given by,

$$\frac{\partial \boldsymbol{f}}{\partial \boldsymbol{x}} = \begin{pmatrix} \frac{\partial u_{0x}}{\partial x} + \frac{\partial c}{\partial x}\nu_x & \frac{\partial u_{0x}}{\partial y} + \frac{\partial c}{\partial y}\nu_x & \frac{\partial u_{0x}}{\partial z} + \frac{\partial c}{\partial z}\nu_x \\ \frac{\partial u_{0y}}{\partial x} + \frac{\partial c}{\partial x}\nu_y & \frac{\partial u_{0y}}{\partial y} + \frac{\partial c}{\partial y}\nu_y & \frac{\partial u_{0y}}{\partial z} + \frac{\partial c}{\partial z}\nu_y \\ \frac{\partial u_{0z}}{\partial x} + \frac{\partial c}{\partial x}\nu_z & \frac{\partial u_{0z}}{\partial y} + \frac{\partial c}{\partial y}\nu_z & \frac{\partial u_{0z}}{\partial z} + \frac{\partial c}{\partial z}\nu_z \end{pmatrix} = \frac{\partial u_{0i}}{\partial x_j} + \frac{\partial c}{\partial x_j}\nu_{x_i} \tag{C.2}$$

$$\frac{\partial \boldsymbol{f}}{\partial \boldsymbol{k}} = \frac{c}{k} \begin{pmatrix} 1-\nu_x^2 & -\nu_x\nu_y & -\nu_x\nu_z \\ -\nu_x\nu_y & 1-\nu_y^2 & -\nu_y\nu_z \\ -\nu_x\nu_z & -\nu_y\nu_z & 1-\nu_z^2 \end{pmatrix} = \frac{c}{k}(\delta_{ij} - \nu_{x_i}\nu_{x_j}) \tag{C.3}$$

$$\frac{\partial \boldsymbol{g}}{\partial \boldsymbol{x}} = -k \begin{pmatrix} \frac{\partial^2 c}{\partial x^2} + \nu_j \frac{\partial^2 u_{0j}}{\partial x^2} & \frac{\partial^2 c}{\partial x \partial y} + \nu_j \frac{\partial^2 u_{0j}}{\partial x \partial y} & \frac{\partial^2 c}{\partial x \partial z} + \nu_j \frac{\partial^2 u_{0j}}{\partial x \partial z} \\ \frac{\partial^2 c}{\partial x \partial y} + \nu_j \frac{\partial^2 u_{0j}}{\partial x \partial y} & \frac{\partial^2 c}{\partial y^2} + \nu_j \frac{\partial^2 u_{0j}}{\partial y^2} & \frac{\partial^2 c}{\partial y \partial z} + \nu_j \frac{\partial^2 u_{0j}}{\partial y \partial z} \\ \frac{\partial^2 c}{\partial x \partial z} + \nu_j \frac{\partial^2 u_{0j}}{\partial x \partial z} & \frac{\partial^2 c}{\partial y \partial z} + \nu_j \frac{\partial^2 u_{0j}}{\partial y \partial z} & \frac{\partial^2 c}{\partial z^2} + \nu_j \frac{\partial^2 u_{0j}}{\partial z^2} \end{pmatrix} = -k \left(\frac{\partial^2 c}{\partial x_i \partial x_j} + \nu_l \frac{\partial^2 u_{0l}}{\partial x_i \partial x_j} \right) \tag{C.4}$$

$$\frac{\partial \boldsymbol{g}}{\partial \boldsymbol{k}} = - \begin{pmatrix} \frac{\partial c}{\partial x}\nu_x + \frac{\partial u_{0x}}{\partial x} & \frac{\partial c}{\partial x}\nu_y + \frac{\partial u_{0y}}{\partial x} & \frac{\partial c}{\partial x}\nu_z + \frac{\partial u_{0z}}{\partial x} \\ \frac{\partial c}{\partial y}\nu_x + \frac{\partial u_{0x}}{\partial y} & \frac{\partial c}{\partial y}\nu_y + \frac{\partial u_{0y}}{\partial y} & \frac{\partial c}{\partial y}\nu_z + \frac{\partial u_{0z}}{\partial y} \\ \frac{\partial c}{\partial z}\nu_x + \frac{\partial u_{0x}}{\partial z} & \frac{\partial c}{\partial z}\nu_y + \frac{\partial u_{0y}}{\partial z} & \frac{\partial c}{\partial z}\nu_z + \frac{\partial u_{0z}}{\partial z} \end{pmatrix} = - \left(\frac{\partial c}{\partial x_i}\nu_{x_j} + \frac{\partial u_{0x_j}}{\partial x_i} \right) \tag{C.5}$$

C.2 Detailed equations for the geodesic elements

$$\left\{ \begin{aligned} \frac{d\boldsymbol{R}}{dt} &= \left(\frac{\partial u_{0i}}{\partial x_j} + \frac{\partial c}{\partial x_j}\nu_{x_i} \right) \times R_j + \frac{c}{k}(\delta_{ij} - \nu_{x_i}\nu_{x_j}) \times Q_j \\ \frac{d\boldsymbol{Q}}{dt} &= -k \left(\frac{\partial^2 c}{\partial x_i \partial x_j} + \nu_l \frac{\partial^2 u_{0l}}{\partial x_i \partial x_j} \right) \times R_j - \left(\frac{\partial c}{\partial x_i}\nu_{x_j} + \frac{\partial u_{0x_j}}{\partial x_i} \right) \times Q_j \end{aligned} \right. \tag{C.6}$$

C.3 Initial conditions

$$\boldsymbol{R}^{\boldsymbol{\theta}}(0) = \boldsymbol{R}^{\boldsymbol{\alpha}}(0) = 0 \tag{C.7}$$

$$\boldsymbol{Q}^{\theta}(0) = \frac{\partial k\boldsymbol{\nu}}{\partial \theta_0}(0) = \frac{\partial k(0)}{\partial \theta_0}\boldsymbol{\nu}_0 + k(0)\frac{\partial \boldsymbol{\nu}_0}{\partial \theta_0} \qquad \boldsymbol{Q}^{\theta}(0) = \left[\frac{-k_0}{(1+\boldsymbol{M}.\boldsymbol{\nu})^2}\boldsymbol{M}.\frac{\partial \boldsymbol{\nu}}{\partial \theta}\right]\boldsymbol{\nu} + k\frac{\partial \boldsymbol{\nu}}{\partial \theta} \tag{C.8}$$

$$\boldsymbol{Q}^{\alpha}(0) = \frac{\partial k\boldsymbol{\nu}}{\partial \alpha_0}(0) = \frac{\partial k(0)}{\partial \alpha_0}\boldsymbol{\nu_0} + k(0)\frac{\partial \boldsymbol{\nu_0}}{\partial \alpha_0} \quad \text{soit} \quad \boldsymbol{Q}^{\alpha}(0) = \left[\frac{-k_0}{(1+\boldsymbol{M}.\boldsymbol{\nu})^2}\boldsymbol{M}.\frac{\partial \boldsymbol{\nu}}{\partial \alpha}\right]\boldsymbol{\nu} + k\frac{\partial \nu}{\partial \alpha} \tag{C.9}$$

Appendix D

Derivation of S_{pp}

It is now shown that the formula of S_{pp} including refraction effects, namely

$$S_{pp}(\boldsymbol{x},\omega) = c_\infty^2\sqrt{\pi}\int ... \int \Pi_n^a(\boldsymbol{y_1},\boldsymbol{x},-\omega)\Pi_m^{a*}(\boldsymbol{y_1}+\boldsymbol{\eta},\boldsymbol{x},-\omega)a_{mn}\, K\,\frac{p_s(\boldsymbol{y_1})p_s(\boldsymbol{y_1}+\boldsymbol{\eta})}{lu_c} \\ \exp\left(-i\omega\frac{\xi}{u_c}\right)\exp\left(-\frac{\omega^2}{4}\frac{l^2}{u_c^2}\right)\exp\left[-\frac{|\xi|}{u_c\tau_s}-\frac{\gamma^2+\zeta^2}{l_\perp^2}\right]d\boldsymbol{y_1}d\boldsymbol{\eta} \tag{D.1}$$

reduces to Equation (3.49) when neglecting refraction. When refraction is neglected, the analytical vector Green's function is known, it is given by (3.24). First, $a_{nm} = 0$ for $m \neq n$. Then, the use of (3.36) gives,

$$\Pi_n^a(\boldsymbol{x},\boldsymbol{y_1},-\omega)\Pi_n^{a*}(\boldsymbol{x},\boldsymbol{y_1}+\boldsymbol{\eta},-\omega) = |\Pi_n^a(\boldsymbol{x},\boldsymbol{y_1},-\omega)|^2 e^{i\frac{\omega}{c_\infty}\frac{\boldsymbol{x}\cdot\boldsymbol{\eta}}{|\boldsymbol{x}-\boldsymbol{y}|}} \tag{D.2}$$

This expression gives,

$$S_{pp}(\boldsymbol{x},\omega) = \frac{\omega^2}{16\pi\sqrt{\pi}c_\infty^4 R^2}\int ... \int \frac{K}{lu_c}\exp\left(-\frac{\omega^2}{4}\frac{l^2}{u_c^2}\right)p_s(\boldsymbol{y})p_s(\boldsymbol{y}+\boldsymbol{\eta})\times ... \\ \exp\left(-i\frac{\omega\xi}{u_c}\right)\exp\left[-\frac{|\xi|}{u_c\tau_s}-\frac{\gamma^2+\zeta^2}{l_\perp^2}\right]\exp\left(i\frac{\omega}{c_\infty}\frac{x_1\xi+x_2\gamma+x_3\zeta}{R}\right)d\boldsymbol{\eta}d\boldsymbol{y} \tag{D.3}$$

which was expected.

ÉCOLE CENTRALE LYON

Direction de la recherche

Liste des personnes Habilitées à Diriger des Recherches en poste à l'Ecole Centrale de Lyon

Nom-Prénom	*Corps grade*	Laboratoire ou à défaut département ECL	Etablissement
BEROUAL Abderrahmane	*professeur*	AMPERE	ECL
BURET François	*professeur*	AMPERE	ECL
JAFFREZIC-RENAULT Nicole	*directeur de recherche*	AMPERE	CNRS/ECL
KRÄHENBÜHL Laurent	*directeur de recherche*	AMPERE	CNRS/ECL
NICOLAS Alain	*professeur*	AMPERE	ECL
NICOLAS Laurent	*directeur de recherche*	AMPERE	CNRS/ECL
SCORLETTI Gérard	*professeur*	AMPERE	ECL
SIMONET Pascal	*directeur de recherche*	AMPERE	CNRS/ECL
VOLLAIRE Christian	*professeur*	AMPERE	ECL

Nbre Ampère 9

HELLOUIN Yves	*maître de conférences*	DER EEA	ECL

Nbre DER EEA 1

GUIRALDENQ Pierre	*professeur émérite*	DER STMS	ECL
VINCENT Léo	*professeur*	DER STMS	ECL

Nbre DER STMS 2

LOHEAC Jean-Pierre	*maître de conférences*	ICJ	ECL
MAITRE Jean-François	*professeur émérite*	ICJ	ECL
MARION Martine	*professeur*	ICJ	ECL
MIRONESCU Elisabeth	*professeur*	ICJ	ECL
MOUSSAOUI Mohand	*professeur*	ICJ	ECL
MUSY François	*maître de conférences*	ICJ	ECL
ZINE Abdel-Malek	*maître de conférences*	ICJ	ECL

Nbre ICJ 7

CALLARD Anne-Ségolène	*professeur*	INL	ECL
CLOAREC Jean-Pierre	*maître de conférences*	INL	ECL
GAFFIOT Frédéric	*professeur*	INL	ECL
GAGNAIRE Alain	*maître de conférences*	INL	ECL
GARRIGUES Michel	*directeur de recherche*	INL	CNRS/ECL
GENDRY Michel	*directeur de recherche*	INL	CNRS/ECL
GRENET Geneviève	*directeur de recherche*	INL	CNRS/ECL
HOLLINGER Guy	*directeur de recherche*	INL	CNRS/ECL
KRAWCZYK Stanislas	*directeur de recherche*	INL	CNRS/ECL
LETARTRE Xavier	*chargé de recherche*	INL	CNRS/ECL
O'CONNOR Ian	*professeur*	INL	ECL
PHANER-GOUTORBE Magali	*professeur*	INL	ECL
ROBACH Yves	*professeur*	INL	ECL

SAINT-GIRONS Guillaume	*chargé de recherche*	INL	CNRS/ECL
SEASSAL Christian	*directeur de recherche*	INL	CNRS/ECL
SOUTEYRAND Eliane	*directeur de recherche*	INL	CNRS/ECL
TARDY Jacques	*directeur de recherche*	INL	CNRS/ECL
VIKTOROVITCH Pierre	*directeur de recherche*	INL	CNRS/ECL

Nbre INL 18

CHEN Liming	*professeur*	LIRIS	ECL
DAVID Bertrand	*professeur*	LIRIS	ECL

Nbre LIRIS 2

BAILLY Christophe	*professeur*	LMFA	ECL
BERTOGLIO Jean-Pierre	*directeur de recherche*	LMFA	CNRS/ECL
BLANC-BENON Philippe	*directeur de recherche*	LMFA	CNRS/ECL
BOGEY Christophe	*chargé de recherche*	LMFA	CNRS/ECL
CAMBON Claude	*directeur de recherche*	LMFA	CNRS/ECL
CARRIERE Philippe	*directeur de recherche*	LMFA	CNRS/ECL
CHAMPOUSSIN J-Claude	*professeur émérite*	LMFA	ECL
COMTE-BELLOT genevièvre	*professeur émérite*	LMFA	ECL
FERRAND Pascal	*directeur de recherche*	LMFA	CNRS/ECL
GALLAND Marie-Annick	*professeur*	LMFA	ECL
GODEFERD Fabien	*directeur de recherche*	LMFA	CNRS/ECL
GOROKHOVSKI Mikhail	*professeur*	LMFA	ECL
HENRY Daniel	*directeur de recherche*	LMFA	CNRS/ECL
JEANDEL Denis	*professeur*	LMFA	ECL
JUVE Daniel	*professeur*	LMFA	ECL
LE RIBAULT Catherine	*chargée de recherche*	LMFA	CNRS/ECL
LEBOEUF Francis	*professeur*	LMFA	ECL
PERKINS Richard	*professeur*	LMFA	ECL
ROGER Michel	*professeur*	LMFA	ECL
SCOTT Julian	*professeur*	LMFA	ECL
SHAO Liang	*directeur de recherche*	LMFA	CNRS/ECL
SIMOENS Serge	*chargé de recherche*	LMFA	CNRS/ECL
TREBINJAC Isabelle	*maître de conférences*	LMFA	ECL

Nbre LMFA 23

BENAYOUN Stéphane	*professeur*	LTDS	ECL
CAMBOU Bernard	*professeur*	LTDS	ECL
COQUILLET Bernard	*maître de conférences*	LTDS	ECL
DANESCU Alexandre	*maître de conférences*	LTDS	ECL
FOUVRY Siegfrid	*chargé de recherche*	LTDS	CNRS/ECL
GEORGES Jean-Marie	*professeur émérite*	LTDS	ECL
GUERRET Chrystelle	*chargé de recherche*	LTDS	CNRS/ECL
HERTZ Dominique	*past*	LTDS	ECL
ICHCHOU Mohamed	*professeur*	LTDS	ECL
JEZEQUEL Louis	*professeur*	LTDS	ECL
JUVE Denyse	*ingénieur de recherche*	LTDS	ECL
KAPSA Philippe	*directeur de recherche*	LTDS	CNRS/ECL
LE BOT Alain	*directeur de recherche*	LTDS	CNRS/ECL
LOUBET Jean-Luc	*directeur de recherche*	LTDS	CNRS/ECL
MARTIN Jean-Michel	*professeur*	LTDS	ECL
MATHIA Thomas	*directeur de recherche*	LTDS	CNRS/ECL
MAZUYER Denis	*professeur*	LTDS	ECL
PERRET-LIAUDET Joël	*maître de conférences*	LTDS	ECL

SALVIA Michelle	*maître de conférences*	LTDS	ECL
SIDOROFF François	*professeur*	LTDS	ECL
SINOU Jean-Jacques	*professeur*	LTDS	ECL
STREMSDOERFER Guy	*professeur*	LTDS	ECL
THOUVEREZ Fabrice	*professeur*	LTDS	ECL
TREHEUX Daniel	*professeur*	LTDS	ECL
VINCENS Eric	*maître de conférences*	LTDS	ECL
		Nbre LTDS 25	
	Total HdR ECL	91	

dernière page de la thèse

AUTORISATION DE SOUTENANCE

Vu les dispositions de l'arrêté du 7 août 2006,

Vu la demande du Directeur de Thèse

Monsieur C. BAILLY

et les rapports de

Monsieur Ph. LAFON
Docteur HDR - LaMSID - UMR EDF/CNRS/CEA 8193 - 1 avenue du Général De Gaulle - BP 408
92141 CLAMART cedex

Et de

Monsieur Ph. MORRIS
Professor - Boeing/A.D. Welliver Professor - Penn State University
Department of Aerospace Engineering - 233C Hammond Building - University Park - PA 16802
Etats-Unis

Monsieur HENRY Cyprien

est autorisé à soutenir une thèse pour l'obtention du grade de **DOCTEUR**

Ecole doctorale MECANIQUE, ENERGETIQUE, GENIE CIVIL ET ACOUSTIQUE

Fait à Ecully, le 4 décembre 2012

P/Le directeur de l'E.C.L.
La directrice des Etudes

M-A. GALLAND

ECOLE CENTRALE DE LYON
36, avenue Guy de Collongue
69134 ECULLY Cedex

Le 13 décembre 2012

PROCES VERBAL
DE SOUTENANCE DE THESE

pour l'obtention du grade de **DOCTEUR**

de

Monsieur HENRY Cyprien

Rapporteurs :

Ph. LAFON	Docteur HDR - LaMSID - UMR EDF/CNRS/CEA 8193 - 1 avenue du Général De Gaulle - BP 408 92141 CLAMART cedex
Ph. MORRIS	Professor - Boeing/A.D. Welliver Professor - Penn State University Department of Aerospace Engineering - 233C Hammond Building - University Park - PA 16802 - Etats-Unis

ECOLE CENTRALE DE LYON

PROCES-VERBAL DE SOUTENANCE DE THESE

Présentée le **13 décembre 2012**

par Monsieur **HENRY Cyprien**

né(e) le 6 avril 1986 à Paris 17ème (75)

N° d'inscription : 11352 N° d'ordre : **2012-60**

en vue de l'obtention du grade de **DOCTEUR**

Ecole doctorale : **MECANIQUE, ENERGETIQUE, GENIE CIVIL ET ACOUSTIQUE**

devant le Jury composé de (1)

Ph. LAFON	Docteur HDR - LaMSID - UMR EDF/CNRS/CEA 8193 - 1 avenue du Général De Gaulle - BP 408 92141 CLAMART cedex
Ph. MORRIS	Professeur - Boeing/A.D. Welliver Professor - Penn State University Department of Aerospace Engineering - 233C Hammond Building - University Park - PA 16802 Etats-Unis
G. BODARD	Docteur - SNECMA - Rond-Point René Ravaud - Réau - 77550 MOISSY-CRAMAYEL
S. DECK	Docteur HDR - ONERA - 29 avenue division Leclerc - 92320 CHATILLON
D. JUVE	Professeur - Laboratoire de Mécanique des Fluides et Acoustique - Ecole Centrale de Lyon
M. PORTA	Docteur - AIRBUS - 316 route de Bayonne - 31060 TOULOUSE cedex 03
C. BAILLY	Professeur - LMFA - Ecole centrale de Lyon

dont le Président nommé en séance : M. Daniel JUVÉ

sur le sujet de thèse suivant :
Prediction of Broadband Shock-Associated Noise in Static and Flight Conditions.

Thèse préparée dans le Laboratoire de Mécanique des Fluides et Acoustique de l'E.C.L.

dirigé par M. M. LANCE

sous la conduite de M. C. BAILLY

---

(1) Le jury doit comprendre au moins trois membres, indiquer les noms et titres des membres du jury.

(2) " La soutenance est publique sauf dérogation accordée par le Président ou le Directeur de l'Etablissement ... L'admission ou l'ajournement est prononcé après délibération du jury. Le président signe le rapport de soutenance qui est contresigné par l'ensemble des membres du jury. " (Arrêté du 7 août 2006).

(3) L'admission peut donner lieu à l'attribution de l'une des mentions suivantes : Honorable, Très Honorable, Très Honorable avec Félicitations.

RAPPORT DE SOUTENANCE :

Monsieur Cyprien Henry a présenté ses travaux de façon concise et très claire. Il a bien mis en avant l'originalité de son travail, alliant calculs de mécanique des fluides et modélisations aéroacoustiques dans l'objectif d'une application en configuration réaliste pour la détermination du bruit de chocs large bande d'écoulements supersoniques co-axiaux. La validation systématique de chaque étape du calcul donne une assise solide au code issu de ce processus complexe.

Le jury souligne tout particulièrement un apport original et très significatif de la thèse, s'appuyant sur l'utilisation d'une méthode de rayons en formulation adjointe, ce qui permet la prise en compte des effets de réfraction induits par des écoulements moyens quelconques.

Monsieur Cyprien Henry a répondu avec beaucoup de franchise aux questions souvent difficiles posées par le jury, démontrant une très bonne maîtrise des différents aspects de son travail.

A l'unanimité le jury propose que l'Ecole centrale de Lyon décerne à Monsieur Cyprien Henry le grade de docteur de l'Université de Lyon, spécialité Acoustique, avec la mention Très Honorable.

Décision : [✓ **ADMISSION** (3)] **AJOURNEMENT**

Mention

☐ **HONORABLE**

☒ **TRES HONORABLE**

☐ **TRES HONORABLE AVEC FELICITATIONS** *

** Il est rappelé en préambule la recommandation unanime du Conseil Scientifique de l'Ecole Centrale de Lyon de ne pas procéder à l'attribution des félicitations du Jury. La délibération du Jury se fait donc dans ce contexte.*

Ecully, le

Fait et signé en séance par les membres du Jury

VU

P/Le Directeur de l'Ecole Centrale de Lyon
La Directrice des Etudes,

M-A. GALLAND

Les Examinateurs :

Ph. LAFON

Ph. MORRIS

G. BODARD

S. DECK

D. JUVE

M. PORTA

Ch. BAILLY

ECOLE CENTRALE DE LYON
36, avenue Guy de Collongue
69134 ECULLY Cedex

ANNEXE DU PROCES-VERBAL DE SOUTENANCE

Avis du Jury sur la reproduction de la Thèse soutenue

Titre de la thèse :
Prediction of Broadband Shock-Associated Noise in Static and Flight Conditions.

Nom et prénom de l'auteur : Monsieur **HENRY Cyprien**

Membres du Jury :
Ph. LAFON - Ph. MORRIS - G. BODARD - S. DECK - D. JUVE - M. PORTA - C. BAILLY

Président du Jury : Daniel JUVÉ

Date de la soutenance : **13 décembre 2012**

Reproduction de la thèse soutenue :

[✓ Thèse pouvant être reproduite en l'état]

Thèse ne pouvant pas être reproduite

Thèse pouvant être reproduite après corrections suggérées au cours de la soutenance

Signature du Président du Jury :

Juvé

En conséquence de quoi, le Directeur de l'E.C.L. autorise la reproduction de la thèse.

P/Le Directeur de l'E.C.L.
La Directrice des Etudes,

M-A. GALLAND

Abstract

This work aims at developing a statistical prediction method for BroadBand Shock-Associated Noise (BBSAN), following recent work from NASA and Boeing. The approach is similar to studies performed for mixing noise models.

First, a methodology has been developed to compute the mean turbulent flow field using the Reynolds Averaged Navier-Stokes (RANS) equations. These equations are solved with elsA, a solver developed by ONERA. Most calculations have been performed on academic configurations. An extensive test campaign has been conducted on these configurations at Ecole Centrale de Lyon (ECL), so that calculations have been thoroughly compared to measurements. Mainly, two operating conditions have been tested. The first one is a jet at $M_j = 1.15$. This condition is typical of a civil engine in cruise. The second operating condition is a jet at $M_j = 1.35$, which rather concerns military engines.

An acoustic model has been developed. It uses the RANS calculation as an input to compute Power Spectrum Densities (PSDs). The intermediate version of the model does not account for refraction effects: acoustic sources are propagated to the far-field using a free field Green's function. As will be seen, this gives good results on simple configurations.

The model has been extended to account for refraction effects. This is achieved by computing a Green's function tailored to the problem. A ray tracing method coupled to an adjoint approach has been used to evaluate the Green's function. The computation of the Green's function has been validated for simple cases. The Green's function calculation has been coupled to the acoustic model. PSDs including refraction effects on dual-stream jets are presented.